6. SITE 1271[1]

Shipboard Scientific Party[2]

OPERATIONS SUMMARY

Transit to Site 1271

Site 1271 is on the southern end of the inside corner high south of the 15°20′N Fracture Zone ~19 nmi northwest of Site 1270. We again chose to use a six-collar bottom-hole assembly (BHA) in order to ensure the preservation of sufficient BHA components for future drilling during this leg.
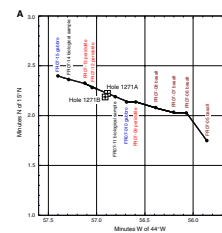
Hole 1271A

Our camera survey for Hole 1271A (Fig. F1) began at Global Positioning System coordinates between samples of gabbro and peridotite collected during *Faranaut* Dive 7 (Fig. F2). Our target was a smooth, sedimented slope above an outcrop of gabbro. After a 1.75-hr survey, we confirmed that our location was on a shallow, eastward-dipping slope of smooth sediment and that our depth (estimated from drill string length) was consistent with our desired drilling location.

Hole 1271A was initiated at 0545 hr on 3 June 2003 through 2.5 m of sediment. The first core required 4.75 hr to advance to 12.9 meters below seafloor (mbsf). Cores 2R and 3R (Table T1), however, were cored in a total of 50 min. After recovering Core 5R, hole conditions began to deteriorate and the driller noted the hole had begun to fill between connections. After only advancing 2.0 m on Core 6R we decided to abandon any further attempt to core deeper. The bit was pulled clear of the seafloor at 0244 hr, ending Hole 1271A. The average rate of penetration for the hole was 4.5 m/hr.

F1. Bathymetry of Site 1271 area, p. 41.
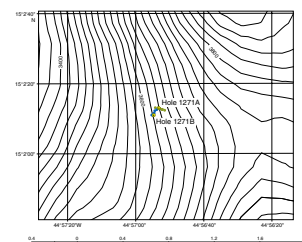
F2. Survey track and bathymetric section, p. 42.

T1. Coring summary, p. 119.

Hole 1271B

Since the shallow sedimented slope where we located Hole 1271A seemed to be our most promising drilling target (based on *Faranaut* Dive 7 videotapes), we decided to move southwest along the same depth contour to position Hole 1271B. Hole 1271B was spudded ~90 m from Hole 1271A.

At 0730 hr on 4 June we began coring Hole 1271B. Cores 1R to 3R were cored without incident, but while drilling Core 4R the driller suspected that a piece of rock had lodged in the bit throat or the bottom of the core barrel. High circulating pressure eventually cleared the obstruction. After cutting Core 4R the driller had difficulty getting the pipe back to the bottom of the hole through several meters of hard fill.

Coring continued through Core 20R (to 103.8 mbsf) with low recovery but little or no indication of poor hole conditions. Having achieved a depth >100 mbsf, we chose to curtail coring operations in order to collect wireline logging data. Coring was completed by 1345 hr on 6 June, and the bit was released in the bottom of Hole 1271B. As the driller attempted to pull the bottom of the pipe to logging depth (nominally 30 mbsf), the hole appeared to collapse around the pipe, shutting off circulation. With some difficulty, the pipe was freed and circulation regained.

After securing the pipe at 30 mbsf, the first logging tool was set up and run into the hole. However, the logging tool would not advance more than 6 m past the end of the pipe, indicating catastrophic hole collapse. Our logging attempt was regretfully abandoned. After the pipe was raised to 2300 meters below sea level (mbsl), we recovered the positioning beacons and began the short transit (~3.7 nmi) to our next site. Operations at Site 1271 ended at 0745 hr on 7 June. The average rate of penetration for the hole was 4.0 m/hr.

IGNEOUS AND MANTLE PETROLOGY

Site 1271 consists of two holes, Holes 1271A and 1271B, that recovered peridotites (dunite and harzburgite), small chromitite pods, and gabbros. In describing and interpreting these rocks we first document the stratigraphic distribution and lithology from Holes 1271A and 1271B then combine these observations to discuss igneous processes inferred from the rocks.
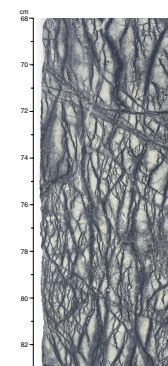
Hole 1271A

This short hole is composed mainly of dunite, with minor amounts of orthopyroxene, so we discuss the features of the hole without subdivision (Fig. F3). The proportion of orthopyroxene pseudomorphs observed in hand sample and in thin section (Figs. F4, F5) varies from 0% to 11%, so most of these peridotites are dunites. An exception is a small piece of altered harzburgite in Section 209-1271A-2R-1. Because of the extreme alteration (Fig. F4), little information can be extracted about the grain size or other textural aspects of the dunite, especially in the uppermost cores (Cores 209-1271A-1R and 2R; 2.56 mbsf). Locally, the dunite is less altered and the original texture and primary mineralogy are still recognizable (Figs. F5, F6). This dunite contains up to 6% orthopyroxene and up to 5% spinel.
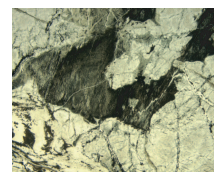
F3. Lithostratigraphic summary, Hole 1271A, p. 44.
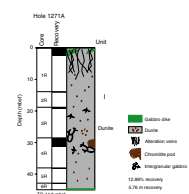
F4. Altered dunite cut by alteration veins, p. 45.

F5. Orthopyroxene pseudomorph in dunite, p. 46.

F6. Plagioclase and orthopyroxene pseudomorph in dunite, p. 47.

Throughout Hole 1271A the dunite is cut by gabbroic intrusions of various sizes in intervals 209-1271A-1R-1 (Piece 7, 23–32 cm) and (Piece 9, 37–51 cm) (Fig. F49A) and 2R-1, 24–51 cm. A large pyroxene crystal (as large as 7 cm) replaced by amphibole is contained in interval 209-1271A-1R-1, 46–50 cm (Fig. F49A). Dunite xenoliths and/or olivine as xenocrysts are included in this gabbroic material (Figs. F7, F8). Gabbroic material is also found along grain boundaries and triple junctions. This material is altered to secondary minerals but is interpreted to have been predominantly plagioclase (Fig. F9). These features can be found throughout the core but are best preserved in Core 209-1271A-4R between 28.5 and 31.23 mbsf. At the bottom of the hole in Core 209-1271A-6R pieces of microgabbro were recovered but they lack lithologic context.

In Core 209-1271A-4R there is a significant amount of chromian spinel, locally as much as 45% of the rock. Examples include euhedral spinels, as large as 3 mm, that occur as small aggregates ~1 cm in diameter or as thin bands (e.g., interval 209-1271A-4R-2 [Piece 3, 61–63 cm]). A chromitite pod ~3 cm in diameter with irregular but sharp contacts in interval 209-1271A-4R-2 (Piece 2, 38–48 cm) represents the maximum enrichment in spinel (Fig. F10). The chromian spinel is associated with chlorite-altered plagioclase(?), olivine, and clinopyroxene. Chromian spinel in dunite and chromitite is reddish brown in thin section. Some small rutile grains are also present in the chromitite pod (Fig. F11). About two-thirds of the grains of chromian spinel in the chromitite are altered to magnetite and/or amorphous (hydr)oxides. The spinels locally include plagioclase and other minerals. Where the spinels are broken and completely altered, the inclusions in them are also altered (Fig. F12).

Hole 1271B

Lithology and Stratigraphy

Hole 1271B consists of 20 cores recovered from 103.8 m of penetration below seafloor. Total recovery was 15.9 m, corresponding to ~15% of the drilled depth. The distribution of rock types defines four lithologic units. From the top of the core down, these are Unit I: dunite/gabbro, Unit II: harzburgite/dunite, Unit III: gabbro/troctolite/dunite, and Unit IV: dunite (Fig. F13).

Unit I

Interval: Sections 209-1271B-1R-1 through 9R-1
Depth: 0–45.7 mbsf
Lithology: dunite/gabbro

Unit I is composed of dunite (63.1%) and gabbro (29.2%) with lesser amounts of harzburgite (6.8%) and breccia (0.9%). Most dunite in Unit I includes gabbroic material (i.e., plagioclase and clinopyroxene/amphibole) interstitial to olivine (see "Lithologic Characterization," p. 5, below). The gabbroic material, now altered to low-temperature minerals, forms rims along grain boundaries of olivine and spinel and millimeter-wide patches at triple junctions (Sections 209-1271B-5R-1 and 6R-1), composing up to 15% of the dunites. Gabbroic material also fills microfractures crosscutting the ultramafic mineral assemblage. The proportion of gabbroic material increases downhole in Unit I. For example, gabbroic material is abundant in the lower part of Section 209-

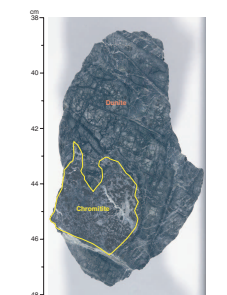**F7.** Olivine grains in amphibolite, p. 48.
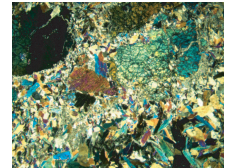
F8. Coarse olivine grain separated in amphibolite, p. 49.
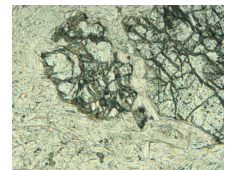
F9. Gabbroic material along olivine grain boundaries, p. 50.

F10. Chromitite pod in dunite, p. 51.

F11. Rutile within chromitite, p. 52.

1271B-8R-1 (bottom of Piece 14) where it forms parallel stringers a few millimeters wide. However, it should be noted that the amount of gabbroic material in the upper half of Unit I (Sections 209-1271B-1R-1 through 3R-1) might have been underestimated because of the significant alteration.

Gabbro is present in most sections of Unit I except Sections 209-1271B-2R-1 and 7R-1. The gabbros in Sections 209-1271B-1R-1 and 3R-1 are highly altered. From Sections 209-1271B-3R-1 (Pieces 17–20) to 8R-1, the bulk of the gabbros contain a large proportion of distinctive brown amphibole. This distinctive brown amphibole gabbro (BAG) occurs throughout Hole 1271B. Overall, the amount of gabbro increases downhole in Unit I from 25.8% in Section 209-1271B-1R-1 to 47.2% in Section 8R-1.

Unit II

Interval: Sections 209-1271B-9R-1 to 11R-1
Depth: 45.70–55.94 mbsf
Lithology: harzburgite/dunite

Unit II is composed of harzburgite (40.7%), dunite (36.0%), and gabbro (23.3%). This unit has more harzburgite than the other units of Hole 1271B. The harzburgite contains as much as 15% orthopyroxene. Coarse- and fine-grained BAGs are intercalated throughout Section 209-1271B-10R-1. A contact between an altered gabbro and dunite occurs in Section 209-1271B-10R-1 (Piece 9), where dunite is cut by an anastomosing network of gabbroic material (Fig. F14A).
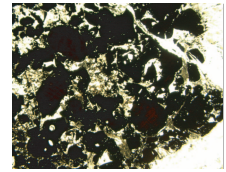
Unit III

Interval: Sections 209-1271B-11R-1 to 18R-1
Depth: 55.94–89.58 mbsf
Lithology: gabbro/troctolite/dunite

Unit III is composed of olivine gabbro and troctolite (41.6%), dunite (39%), and gabbro (17.8%) with a small amount of chromitite (0.8%) and breccia (0.8%). The olivine gabbro and troctolite are interpreted to have originated as a dunite sequence that was pervasively infiltrated by melt that crystallized plagioclase and clinopyroxene along olivine grain boundaries, resulting in hybrid rocks now classified as olivine gabbros and troctolites. At a mesoscale, xenoliths of dunite are enclosed in the gabbroic rocks (Fig. F14B, F14C). Amphibole is relatively abundant in the gabbroic rocks. Parts of Hole 1271B thus contain dunite–gabbro hybrid rocks, with a transition from peridotites with small proportions of gabbroic material along grain boundaries to rocks with 15%–55% gabbroic material. There is a continuous range in size of gabbroic bodies from decimeter- to millimeter-sized intergranular patches. The olivine gabbro/troctolite/dunite hybrid rocks are abundant in the upper and lower parts of Unit III but are scarce in the middle of the unit where massive gabbro predominates. Other than the gabbro in the dunites, the most abundant gabbro type in this unit is BAG. Minor amphibolite horizons are present, but the origin of these rocks is ambiguous. They might have been clinopyroxene megacrysts, clinopyroxenites, or some other lithology that was completely modified.
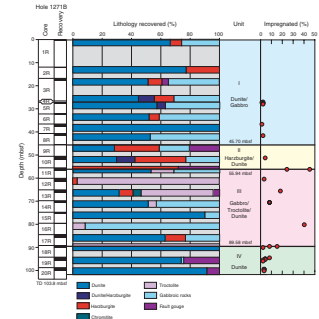
Unit IV

Interval: Sections 209-1271B-18R-1 to 20R-1
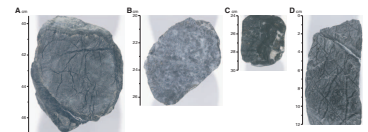Depth: 89.58–100.08 mbsf
Lithology: dunite

F12. Chromitite with opaque altered grains, p. 53.

F13. Lithostratigraphic summary, Hole 1271B, p. 54.

F14. Gabbroic material in peridotites, p. 55.

Unit IV is composed of dunite (99.0%) with a minor amount of altered gabbro (1.0%). The dunite in Unit IV is like that in Unit I in that it contains various proportions of gabbroic material along olivine grain boundaries. These relations are better preserved in Unit IV and allow us to document the distribution of the gabbroic material and recognize the primary features (textures and grain sizes) of the dunites (Fig. F14D). The percentage of gabbroic material varies from piece to piece, from 1% to 15%, and is irregularly distributed within each piece. Sections 209-1271B-19R-1 (Pieces 3–6) and 19R-2 (Piece 1) contain large (2 mm) parallel gabbroic stringers. In the same section, thin intervals of mud made of serpentinized dunite, retaining the original rock texture, alternate with the rock samples through the sequence. These dunites contain the largest proportions of gabbro material, predominantly present as subparallel stringers.

Lithologic Characterization

Dunite

Dunite has protogranular textures. Original grain sizes range from 5 to 15 mm, determined where the grain boundaries are defined by the presence of intergranular gabbroic material. Olivine is the major mineral phase (90%–100%), associated with minor orthopyroxene (<10%) and accessory spinel. Spinel is relatively coarse (1–2 mm) and subhedral to rounded. Spinel is present at triple junctions of olivine grains or is enclosed in olivine. Spinel inclusions in olivine can be found in trains of tiny grains. Some spinel-rich dunites (e.g., 10% in Section 209-1271B-2R-1 [Piece 3] and 5% in Section 3R-1 [Piece 16]) have larger spinel grains (as large as 4 mm) concentrated in 1- to 3-mm-thick bands (e.g., Sections 209-1271B-5R-1 [Pieces 9 and 10] and 7R-1 [Pieces 1, 4, 5, and 7–12]). In Section 209-1271B-20R-1 (Piece 11), a 4-mm-thick spinel-rich band is present. Despite locally high proportions of spinel elsewhere in the hole, Unit IV dunite has the most spinel, with an average of 5%. Spinel in dunite from Hole 1271A is reddish black, whereas spinel in dunite from Hole 1271B is reddish brown. This reddish color of spinel in Site 1271 peridotite suggests that it has a higher Fe^{3+}/Fe^{2+} ratio than spinel in typical abyssal peridotite.

Harzburgite

Harzburgite abundance increases toward the bottom of Unit I. The rocks contain olivine (75–88 vol%) and orthopyroxene (10%–25%), with accessory spinel (<1%). No clinopyroxene was found. However, most harzburgite samples are highly altered, making it difficult to estimate modal composition and texture. Where less altered, harzburgite shows a protogranular texture, in which orthopyroxene has smooth, curved boundaries with surrounding olivine. Grain sizes vary from 1 to 7 mm, with some as large as 15 mm (Section 209-1271B-10R-1 [Piece 24]). Spinel occurs as tiny disseminated grains (0.2 mm) or as large as 4-mm grains in close proximity to orthopyroxene. Harzburgite, like dunite, may contain a small amount of intergranular gabbroic material originally present as plagioclase and clinopyroxene but now altered.

Gabbro in Dunite

Almost all dunite in Holes 1271A and 1271B contains some amount of gabbroic material (1%–15%) that reacted with spinel and orthopyroxene, and possibly with olivine. This gabbroic material, probably mostly plagioclase (now altered), is distributed in an intergranular net-

work along olivine and spinel grain boundaries (Fig. F14D). Millimeter-wide patches of plagioclase and clinopyroxene, now largely altered to amphibole, crystallized at olivine triple junctions. Parallel gabbro stringers (<1 mm thick) are replaced by amphibole or low-temperature alteration minerals. Where alteration is limited, spinel near gabbroic material shows a reaction rim characterized by symplectites of spinel and an altered mineral, possibly originally plagioclase (Fig. F15A, F15B). Intergrowths of spinel, olivine, and an alteration phase also occur along the margins of olivine (Fig. F15C–F15F). Similar intergrowths are also observed at olivine triple junctions and enclosed within olivine (Fig. F16A, F16B). The alteration phase in these intergrowths might have replaced pyroxene, plagioclase, or even amphibole. Where the amount of gabbroic material reaches ~20%–30%, disaggregation of the peridotite minerals can be observed. Coarse olivine aggregates are dispersed into isolated grains separated by amphibole ± plagioclase assemblages, so that very few of the olivine grains show grain/grain contact (Fig. F17A–F17C). The peridotite in Unit III has been most extensively modified. The olivine gabbros and troctolites in this unit contain dunite xenoliths and xenocrysts (olivine and spinel) that may have partially reequilibrated with the gabbroic material.
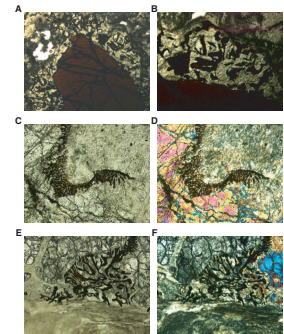
Olivine Gabbros and Troctolites

Oikocrystic olivine gabbro has subhedral olivine grains as large as 12 mm enclosed in a plagioclase matrix (Fig. F18A) and/or coarse poikilitic clinopyroxene (Fig. F18B, F18C). Euhedral laths of plagioclase are in direct contact with olivine, with no reaction relationships, and this assemblage is itself enclosed in clinopyroxene oikocrysts (Fig. F18D). In troctolites, a rim of tiny amphibole crystals is developed around olivine grains in contact with plagioclase. This texture is interpreted as a reaction rim. In other places, olivine grains are more extensively mantled and/or partially replaced by amphiboles and clusters of plagioclase form the remainder of the rock (Fig. F18E, F18F). In the more extensive mantles, the amphibole assemblages may not be reaction rims between plagioclase and olivine but may also include some former igneous pyroxene that crystallized in association with plagioclase. Other samples contain olivine set in a finer-grained matrix of amphibole and 5%–25% plagioclase (Fig. F16C). Euhedral magnetite is a common accessory mineral in all these rocks. It is enclosed in olivine or occurs at its border and in the amphibole/plagioclase assemblages.

In many cases, the origin of the amphibole in gabbros and troctolites is ambiguous. It may have replaced clinopyroxene, orthopyroxene, olivine, or earlier amphibole. There are several generations of amphibole, characterized by various grain sizes and textural relationships with the other minerals. Rarely, some coarser, more equant amphibole crystals seem to be clinopyroxene pseudomorphs. Early amphibole might have been in equilibrium with olivine, as suggested by sharp contact between the two phases and by the presence of discrete, euhedral, fresh amphibole enclosed within olivine (Fig. F16D).

The origin of the olivine in these hybrid rocks is not always clear. Their interpretation as olivine xenocrysts is based on the presence of coarse-grained olivine in dunites that are partly disaggregated into smaller grains separated by amphibole ± plagioclase as described above. Interval 209-1271B-17R-1, 43–48 cm, contains a 1-cm dunitic xenolith (Fig. F19A). Although very altered, a reaction rim is still recognizable between the olivine and the amphibolite matrix (Fig. F19B, F19C) with pseudomorphs of symplectites, much like those observed in symplec-
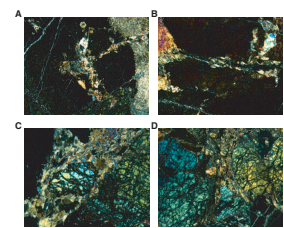
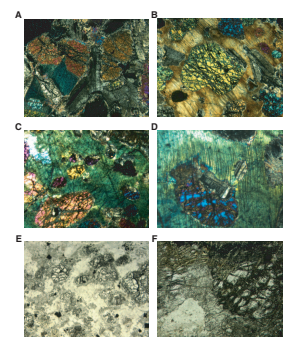**F15.** Reaction rims around olivine and spinel, p. 56.

F16. Mineral inclusions in olivine, p. 57.
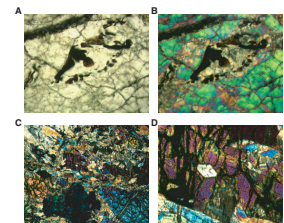
F17. Incipient fragmentation of olivine in dunite, p. 58.

F18. Olivine and plagioclase in gabbro and troctolite, p. 59.

tite-bearing dunites (Fig. F15C, F15D) and troctolites. Many of the olivine grains included in gabbroic material are large with rounded shapes, suggesting that they were originally large olivine crystals in the dunite but were disaggregated and perhaps partially resorbed. However, igneous olivine may also be present in some samples that have plagioclase closely associated with the olivine. The rounded morphology of olivine in these rocks may therefore reflect overgrowths on xenocrysts. The olivine gabbros and troctolites are thus interpreted as hybrid rocks resulting from the inclusion of olivine from dunite into a melt crystallizing a gabbroic phase assemblage. Although the gabbroic portions of these rocks are generally altered to amphiboles, the olivine is mostly fresh and either in equilibrium with amphibole or being replaced by amphibole along grain boundaries. The amount of gabbroic/amphibolitic material in olivine gabbros and troctolites varies from 15% to 80%, producing various textures in these rocks. When gabbroic material composes as much as 80% of the rock, the olivine crystals occur either as isolated single crystals or in small clusters in the gabbroic/amphibolite matrix.
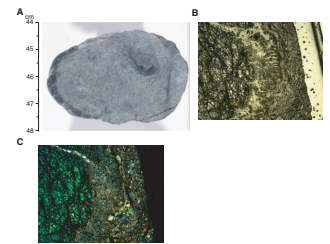
Gabbro

The gabbroic rocks in Hole 1271B include gabbro (sensu stricto), microgabbronorite, and BAG. The gabbro contains only primary plagioclase and clinopyroxene, is coarse grained with ophitic clinopyroxene, and has plagioclase grains >35 mm. A gabbronorite with a magmatic foliation from Section 209-1271B-8R-1 (Piece 9) contains 55% plagioclase, 35% clinopyroxene, 8% orthopyroxene, and 2% oxide.

The BAG contains 35%–55% plagioclase (1–13 mm), 40%–60% brown amphibole (2–20 mm), and accessory minerals, most notably rutile and in some samples ilmenite (the proportion of ilmenite is as high as 20% in a few samples). The amphibole is generally completely fresh, whereas the plagioclase is almost completely altered. The amphibole in the BAG is of uncertain paragenesis. We consider three possibilities for its origin: (1) it is a primary magmatic phase, (2) it is a metamorphic replacement of clinopyroxene, and/or (3) it is a late-stage magmatic reaction product. The presence of euhedral amphibole with sharp grain boundaries supports a magmatic origin (F20A). The euhedral rutile grains included in the amphibole would then require that the rutile is also magmatic, as it is too concentrated to be exsolved from the amphibole (Fig. F20B). Gabbro that has textural characteristics similar to the BAG is found in the same sections as the BAG and is a potential example of the igneous progenitor, subsequently modified by late-magmatic or metamorphic replacement to produce a BAG (Fig. F20C). The presence of latticework extensions of amphibole into plagioclase-rich areas suggests that the amphibole is replacing both clinopyroxene and plagioclase (Fig. F20D). However, close inspection of the gabbro reveals fine tendrils of the ophitic clinopyroxene between plagioclase crystals. If the brown amphibole crystallized from a magma with a similar morphology, then after alteration of the plagioclase the relict amphibole tendrils might be misinterpreted as replacing the plagioclase. Likewise, if the amphibole is metamorphic and replaced igneous clinopyroxene with this habit, it would explain the observed characteristics of the amphibole without requiring that plagioclase be replaced by amphibole.

A small number of amphibole-rich rocks (composed of amphibole [>95%] with minor plagioclase [<5%]) are also present. They are similar to the altered interstitial material in hybridized dunites, olivine gab-

F19. Xenolith of dunite in gabbro replaced by amphibolite, p. 60.

F20. Gabbroic rocks, p. 61.
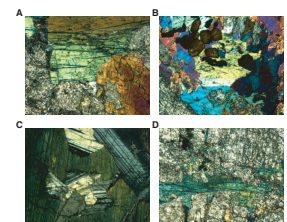
bros, and troctolites. Their origin is ambiguous, but some might have been clinopyroxene megacrysts, gabbros, or igneous rocks rich in primary amphibole.

Chromitite

Chromitites (35%–45% modal spinel) are found in Hole 1271A (Section 209-1271A-4R-2) and at two horizons in Hole 1271B (Sections 209-1271B-13R-1 [Piece 6] and 14R-1 [Piece 7]). The horizon in Section 209-1271B-14R-1 forms a 3-mm-wide band in amphibolite. The spinel is reddish brown, euhedral, and 0.5–2 mm in diameter. The proportion of spinel varies from 35% to 45%, and the grain size ranges from 1 to 5 mm with euhedral to subhedral grains. Spinel crystals are surrounded by a matrix of olivine with a small amount of chlorite (replacing plagioclase or formed by reactions between olivine, pyroxene, and spinel) filling cracks in spinel.

Discussion

Almost all of the peridotite from Site 1271 contains some amount of gabbroic material (typically 1%–15%) crystallized from a liquid that migrated along the grain boundaries and reacted with spinel, orthopyroxene, and olivine. Where the volume of gabbroic material is large (15%–40%), it is associated with the mechanical disaggregation of the peridotite. The best examples of this process are preserved in Hole 1271B, Unit III. When the volume fraction of gabbroic material exceeds ~40%, the rocks have the appearance of gabbroic cumulates and these rocks are named olivine gabbros and troctolites. They have a matrix that was originally (and in some examples still is) composed of plagioclase and clinopyroxene that enclosed dunite xenoliths and xenocrysts (olivine and spinel).

On the basis of the lithologic variation in Hole 1271B we envision the following genesis of these rocks:

1. During the early stages of uplift of the mantle, basaltic liquids migrated principally along grain boundaries by porous flow.
2. With decreasing temperature, plagioclase and clinopyroxene began to crystallize from this liquid, resulting in the incorporation of small amounts of interstitial gabbroic material in dunite and harzburgite (Units I–IV).
3. Locally, the flow was more focused, resulting in channels that produced a hybrid rock composed of a mixture of disaggregated olivine and gabbro (Unit III).
4. With further cooling, the flow switched from porous media to fracture flow, resulting in the crystallization of gabbroic rocks in small patches throughout the peridotite sequence.

A remarkable feature of Site 1271 is the occurrence of chromitite pods (up to 4 cm in diameter) and several chromite layers included in chromian spinel–rich dunite and in amphibolite. This is the first podiform chromitite in abyssal peridotite reported from the Mid-Atlantic Ridge. A small chromitite "minipod" included in a troctolite (with a hybrid origin as described above) was reported from Hess Deep, East Pacific Rise (Leg 147 Site 895; Arai and Matsukage, 1996). Podiform chromitite, usually surrounded by dunite within harzburgite, is common in the mantle section of ophiolites (e.g., Nicolas, 1989), but lherzolite-hosted podiform chromitite is very rare (Irvine, 1977). It is therefore generally believed

that the origin of podiform chromitite requires interaction between liquid and moderately depleted harzburgite (e.g., Zhou et al., 1994; Arai and Yurimoto, 1994; Arai and Abe, 1995), as seen at Site 1271.

Recent experimental study suggests that crystallization of water-rich basaltic liquid can duplicate the nodular textures typical of podiform chromitite (Matveev and Ballhaus, 2002). Surprisingly, given our findings, Matveev and Ballhaus (2002) conclude that podiform chromitites are not expected to occur in oceanic lithosphere forming at mid-ocean ridges because mid-ocean-ridge basalt does not contain sufficient H_2O.

An intriguing feature of Site 1271, and especially Hole 1271B, is the abundance of the amphibole in nearly all the different lithologies. Several generations of amphibole are present, so that in many cases amphibole is clearly replacing former igneous minerals. Textural evidence, such as curved olivine/amphibole grain boundaries and euhedral amphibole inclusions in olivine, indicates that at least some of the amphibole formed in equilibrium with olivine. The chromitite pods found at Site 1271 are all associated with amphibole-rich gabbro and amphibole-bearing dunite. It is also notable that one of the three chromitite bands is enclosed within amphibolite rather than dunite. The association of chromitite and amphibole at Site 1271 is probably not a coincidence and suggests that even in a mid-ocean-ridge environment, abundant H_2O may be involved in chromitite genesis.

The scale of the chromitites (a few centimeters in maximum dimension) and high concentration of chromian spinel in the dunite throughout Site 1271 suggests that these chromitites are similar to podiform chromitites found in many ophiolites. Lithologic variations similar to those in Hole 1271 have been reported from some ophiolites. The association of partially hybridized peridotite with chromitite, gabbroic rocks, and troctolites with various amounts of plagioclase is common in the Mohorovicic (Moho) transition zone of the Oman ophiolite (Nicolas, 1989; Boudier and Nicolas, 1995). However, in the Oman ophiolite amphibole is rare in the Moho transition zone.

METAMORPHIC PETROLOGY

Two holes were cored at Site 1271, which is located at the inside corner high of the Mid-Atlantic Ridge segment south of the 15°20′N Fracture Zone.

The drill core from Hole 1271A consists predominantly of completely serpentinized dunite. Locally, the serpentinites include brucite. Some intervals also experienced low-temperature seafloor weathering. Gabbroic intrusions are a minor component in Hole 1271A.

The drill core from Hole 1271B consists of a complex association of completely altered mafic (gabbros and amphibolites) and ultramafic rocks, dominated by dunite and harzburgite. These are intruded and infiltrated by amphibole-bearing gabbroic lithologies and have experienced variable degrees of syndeformational hydrothermal alteration. Relatively fresh dunite is also present, particularly in proximity to amphibolites.

Hole 1271A

The recovered core consists of highly to completely serpentinized dunite and minor intercalated, highly to completely altered gabbro and microgabbro. Veining is generally well developed throughout the core,

and several generations of veins can be discriminated. Locally, the dunite shows signs of low-temperature oxidative alteration, whereas serpentine-brucite alteration prevails near the bottom of the hole. The degree of downhole alteration is illustrated in Figure F21.

Hydrothermal Alteration

Alteration of Dunite

Hole 1271A is dominated by light gray to black completely serpentinized dunites. Microtextures in the serpentinized dunite range from pseudomorphic mesh texture through transitional texture to non-pseudomorphic ribbon texture. Unaltered orthopyroxene and traces of fresh olivine are restricted to interval 209-1271A-1R-1, 13–19 cm. In Sections 209-1271A-1R-1 and 1R-2, the dunites have a yellowish green to gray groundmass hosting abundant transgranular, black serpentine-magnetite veins, mainly oriented parallel to the long axis of the core (Fig. F22; Table T2).

Within the gray-green to black dunites of Sections 209-1271A-4R-1 and 4R-2, there are intermittently distributed centimeter-scale, occasionally branched veinlike domains and patches that consist mainly of chlorite-talc-amphibole. These are interpreted as the alteration products of intrusions of gabbroic material along olivine grain boundaries (see "Igneous and Mantle Petrology," p. 2).

Chromite is present in Section 209-1271A-4R-1 as a nodular, centimeter-sized chromitite pod (interval 4R-1, 80–83 cm). Within this pod, chlorite, talc, and smectite form the interstitial material between chromite grains and probably represent the alteration products of pyroxene, olivine, and/or plagioclase.

At least some parts of the dark gray, completely altered dunite in Section 209-1271A-4R-2 include a substantial proportion of brucite. This style of alteration is macroscopically indistinguishable from serpentine without brucite and has been recognized during the course of X-ray diffraction analyses and thin section observations (Fig. F23; Table T2). Brucite forms aggregates of fine elongate crystals with anomalous brown interference colors that are surrounded by and intergrown with serpentine, indicating that the brucite formed at the same time as serpentine. This represents the first major occurrence of brucite in altered ultramafic rocks identified during the course of Leg 209.

Some of the dunite experienced variable degrees of low-temperature seafloor weathering with orange to brownish spots containing clays, iron oxyhydroxides, and minor carbonate. This style of alteration is particularly common in Section 209-1271A-3R-1. A fault breccia in interval 209-1271A-1R-1, 7–13 cm, is composed of weathered serpentinized dunite clasts in a carbonate-rich matrix with minor green clay.

Alteration of Gabbro

Intrusions of variably altered gabbroic material in the serpentinized dunite are present in intervals 209-1271A-1R-1, 37–51 cm; 1R-1, 23–32 cm; 2R-1, 4–14 cm; and 6R-1, 6–25 cm. Plagioclase in these gabbros and microgabbros was commonly replaced by sericite, quartz, and secondary sodic plagioclase, and pyroxene experienced slight to moderate amphibole-chlorite alteration.

Interval 209-1271A-1R-1, 37–51 cm, is exceptional and represents an olivine-bearing, pegmatitic gabbro dike. Pyroxene and plagioclase were completely altered to an assemblage of amphibole, chlorite, and sec-
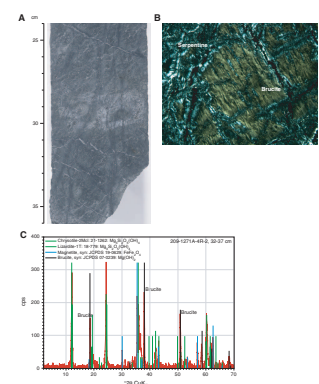
F21. Alteration intensity, Hole 1271A, p. 62.
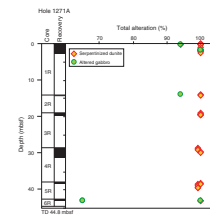
F22. Serpentinized dunite characteristics, p. 63.
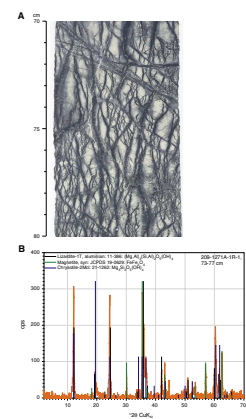
T2. XRD results, p. 120.

F23. Characteristics of completely altered dunite, p. 64.

ondary plagioclase. Olivine is largely unaffected by alteration except for minor talc replacement along its margins.

Metamorphic Veins

Metamorphic veins in Hole 1271A account for 6.8 vol% of the recovered core (Table T3) and consist predominantly of serpentine (79 vol%) (Fig. F24). Other vein minerals are talc (8.6 vol%), amphibole (5.3 vol%), magnetite (2.5 vol%), carbonates (2.1 vol%), and minor zeolites, clays, and iron oxides (other than magnetite).

Several different transgranular vein types were recognized in the serpentinized dunite of Hole 1271A: serpentine-magnetite veins, green picrolite veins, white chrysotile veins, talc-amphibole veins, and carbonate (mainly aragonite)-clay veins. Serpentine-magnetite veins are crosscut by all other vein generations and, therefore, represent the earliest veining event. Other crosscutting relationships indicate that the white chrysotile veins postdate green picrolite and talc-amphibole veins. The carbonate veins represent the last generation of metamorphic veins.

Discussion

In Hole 1271A, dunite was mainly replaced by serpentine; however, noticeable amounts of brucite are present in Section 209-1271A-4R-2. The textural relationships indicate that brucite formed from the olivine breakdown reaction:

$$H_2O + \text{olivine} \rightarrow \text{serpentine} + \text{brucite}.$$

Chemical analyses of two brucite-bearing dunites reveal (Fe + Mg)/Si molar ratios of 1.98 and 2.01, respectively, basically identical to that of olivine (cf. "Geochemistry," p. 27). This result suggests that olivine reacted with water to form serpentine and brucite without significant Si, Mg, and Fe mass transfer.

Chlorite-amphibole assemblages of the subordinate gabbroic intrusions in Hole 1271A represent static greenschist facies alteration, similar to the style of alteration observed in gabbros from Sites 1268 (lower part of Hole 1268A) and 1270 (Hole 1270B). An exceptional pegmatitic olivine gabbro dike contains abundant fresh olivine that has been only marginally replaced by talc, whereas pyroxene and plagioclase were completely replaced by amphibole, chlorite, and secondary plagioclase. Apparently, the olivine stability and reaction kinetics during alteration were strongly dependent on the primary lithology of the rocks.

Veining in Hole 1271A is intense (6.8 vol% of the core), suggesting that fracture-controlled hydrothermal fluid flow was relatively abundant in this area. All veins show transgranular geometries, which may indicate that even the earliest vein generation (serpentine-magnetite) formed at a late stage of serpentinization. The late-stage formation of carbonate veins probably took place during low-temperature seafloor weathering of the succession. This is consistent with the observation of carbonate cement in a fault zone (interval 209-1271A-1R-1, 7–13 cm) that contains weathered serpentinized dunite clasts.

T3. Vein mineralogy, p. 121.

F24. Vein mineralogy, Hole 1271A, p. 65.
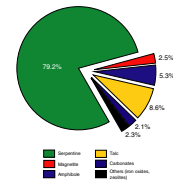
Hole 1271B

Three distinct lithologies, harzburgites/dunites, BAGs, and amphibole-bearing dunites, are present in Hole 1271B. Each lithology is variably altered and shows characteristic features that are described separately. However, the different features within each lithology may in fact be linked by common processes (see "Discussion," p. 14, below).

Hydrothermal Alteration

Alteration of Harzburgite and Dunite

Serpentinized dunite composes a greater proportion of the recovered core than serpentinized harzburgite in Hole 1271B. This differs from the relative proportions recovered at Sites 1268 and 1270, where serpentinized harzburgites were dominant. Serpentinized dunite and harzburgite range from light or dark green (Sections 209-1271B-1R-1 and 2R-1) to gray (Section 19R-1) to black (Sections 7R-1 and 19R-1) and are composed mainly of serpentine and magnetite (Table T2). Brucite forms ~5% of a thin section from Sample 209-1271B-6R-1, 9–12 cm, as brown aggregates in serpentine mesh texture. Noticeable amounts of brucite are also present near the bottom of the hole in Sections 209-1271B-17R-1 to 19R-1. The amount of brucite in these intervals is lower than that in Section 209-1271A-4R-2. Serpentinization textures vary from relict mesh texture to ribbon textures to shear zones in which a distinct foliation is present. Locally, bastite pseudomorphs after orthopyroxene are present (e.g., Section 209-1271B-6R-1). Talc alteration is minor in Hole 1271B and is present only in three short intervals related to deformation. For example, in talc-tremolite schists found in intervals 209-1271B-12R-1, 0–12 cm, 24–33 cm, and 42–55 cm, and 3R-1, 17–22 cm, talc accounts for as much as 35% of the schist. Additional talc alteration is present in Section 209-1271B-10R-1 (intervals 7–10 cm, 21–24 cm, 26–30 cm, 36–39 cm, and 106–118 cm), where as much as 15% of the rock is altered to talc. In relatively fresh dunites (e.g., Sections 209-1271B-12R-1 and 13R-1), rare orthopyroxene is replaced by talc, which has potential implications for reconstructing the conditions of serpentinization (see "Discussion," p. 14, below).

Orange clay and iron oxyhydroxide weathering is minor; however, it is locally present throughout the core (e.g., Sections 209-1271B-1R-1, 37–41 cm, and 58–64 cm, and all of Section 4R-1, in particular, intervals 1–3 cm, 10–19 cm, and 50–63 cm). This low-temperature alteration affects relict primary phases much more than it affects hydrous phases produced by serpentinization. Therefore, where clay and iron oxyhydroxide are developed, they have probably replaced relict olivine (and to lesser extent orthopyroxene).

Brown Amphibole Gabbro. Highly to completely altered BAG is present throughout the core, with the exception of the upper 18 and the lower 15 m of Hole 1271B (Fig. F25). The secondary mineral assemblages in the BAG do not show significant variation with depth. BAG is altered to secondary amphibole, talc, chlorite, and sericite with a trace of zeolite. Brown amphibole and minor talc replace former clinopyroxene, and plagioclase is altered to quartz, sericite, secondary plagioclase, and minor amphibole. A remarkable feature of the BAG is the presence of rutile (up to 2%). Rutile intergrown with quartz appears to replace primary Fe-Ti oxides in a few instances, suggesting that rutile may form hydrotherm-

F25. Alteration intensity, Hole 1271B, p. 66.
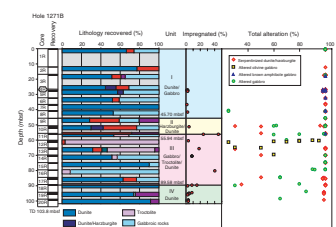
ally. The presence of rutile, rather than titanite, may indicate alteration under amphibolite facies conditions.

Tremolite-talc schists probably represent highly sheared and retrogressed BAG. A tremolite-talc schist from interval 209-1271B-3R-1, 18–22 cm, is composed of acicular to prismatic tremolite (50%–60%) with fibrous talc (30%–40%) and minor chlorite. Anastomosing gabbroic veins or dikes are present in amphibole-bearing dunite (intervals 209-1271B-11R-1, 44–49 cm, 72–76 cm, and 82–108 cm) and exhibit similar talc-amphibole–dominated secondary mineral assemblages while showing complex relationships between hydrothermal alteration and deformation (see "Discussion," p. 14).

Gabbros and Microgabbros. In addition to the BAG, a second type of variably altered gabbro and microgabbro is present in various sections of Hole 1271B (e.g., interval 209-1271B-10R-1, 11–20 cm) (Fig. F25). These rocks are volumetrically less significant than the BAG. They are moderately to completely altered to secondary plagioclase, green amphibole, chlorite, and minor talc and quartz.

Alteration of Hybrid Rocks. Two rock types have tentatively been described as affected by crystallization of interstitial gabbroic material from intergranular melt (see "Igneous and Mantle Petrology," p. 2): (1) the development of diffuse vein networks and patches of chlorite, talc, and minor green amphibole within ultramafic rocks and (2) amphibolites that appear to penetrate into dunite and locally engulf dunite fragments.

The chlorite + talc–rich veinlets were described above. Their origin is unknown. They are present in fresh dunite as well as in completely serpentinized dunite, and they contrast markedly in style and geometry with other veins that are clearly metamorphic (see below). A preliminary interpretation of these features is that plagioclase and pyroxene crystallized from melts migrating along grain boundaries in dunite and harzburgite and subsequently were hydrothermally altered to talc, chlorite, and minor amphibole.

Amphibole-bearing dunites in which the dunite is commonly relatively fresh first appear in Section 209-1271B-10R-1. Green amphibole with minor chlorite and traces of quartz is interstitial to olivine. A few samples include relict coarse-grained plagioclase, suggesting that the protolith of the amphibole + chlorite + quartz assemblage was gabbro. The contacts between dunite and amphibole-bearing assemblages are variable and complex. The general impression is that of intrusions of mafic material into dunite, locally disaggregating it and engulfing centimeter-sized dunite fragments, while forming apophyses and veins in other sections of the core. Alteration of the dunite to serpentine begins along irregular cracks that form a mesh network, usually with fresh olivine in the mesh centers (Fig. F26). Olivine is also replaced by amphibole, particularly in proximity to the contacts with mafic material. Amphibolitization of olivine is pseudomorphic and preserves the magnetite rims of mesh texture in olivine (Fig. F27). Orthopyroxenes with vermicular spinel are altered to talc, even in relatively fresh dunite (e.g., Sample 209-1271B-10R-1, 40–43 cm) (Fig. F28). In Section 209-1271B-13R-1 the relationship between the presence of amphibolite and the extent of olivine preservation is best developed. It appears that dunite in contact with mafic material is much less serpentinized than dunite in sections of the core that do not contain mafic material. A sharp reaction front between completely serpentinized dunite and relatively fresh

F26. Chlorite-sericite-amphibole in olivine-bearing dunite, p. 67.
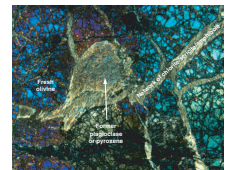
F27. Olivine replaced by amphibole, chlorite, and sericite, p. 68.
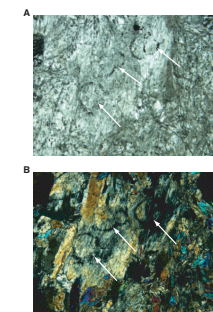
F28. Talc-altered orthopyroxenes with relict vermicular spinel, p. 69.

dunite with amphibole veins is present in Section 209-1271B-10R-1 (Fig. F29).

Alteration in Fault Zones. Fault breccia is present in interval 209-1271B-3R-1, 48–54 cm, which is composed of completely serpentinized clasts of dunite with a small amount of talc in a carbonate/green clay matrix. However, similar to intervals 209-1270A-2R-1, 101–104 cm, and 1R-1, 7–13 cm, fault breccia is volumetrically insignificant. Green serpentine mud, presumably representing a fault zone, is present in intervals 209-1271B-19R-1, 4–10 cm, 50–57 cm, 73–83 cm, and 96–103 cm.

Metamorphic Veins

Serpentine and magnetite dominate the vein mineralogy of Hole 1271B, jointly accounting for 77% of the volume of the veins and 3.1% of the volume of the core (Fig. F30; Table T3). Other vein minerals are talc, carbonate, amphibole, quartz, and minor chlorite, epidote, iron oxide, and clay.

Black serpentine + magnetite veins are the dominant vein type in Hole 1271B. Locally, they form anastomosing networks (e.g., Section 209-1271B-6R-1) and persist through areas of intense orange clay and iron oxyhydroxide weathering (see "Alteration of Harzburgite and Dunite," p. 12, in "Hydrothermal Alteration," above). They are crosscut by a second generation of serpentine + magnetite veins and are subsequently crosscut by white sigmoidal chrysotile veins (e.g., Section 209-1271B-3R-1). All of these generations are crosscut by late serpentine + magnetite veins in interval 209-1271B-6R-1, 9–12 cm, and green and white picrolite veins in Sections 209-1271B-1R-1 and 3R-1. Given the complex crosscutting relations between the various generations of serpentine veins, it is difficult to interpret the exact timing of each of these generations, and some may be emplaced synchronous to others. All generations of serpentine veins are developed throughout the core.

Late, vuggy aragonite veins crosscut all other vein generations (as in Hole 1271A). They are composed of coarse-grained, acicular to prismatic aragonite aggregates with minor green clay (Sections 209-1271B-2R-1, 4R-1, 7R-1, and 15R-1). Aragonite veins are particularly abundant in interval 209-1271B-15R-1, 37–68 cm, where the serpentinized harzburgite is strongly weathered.

Quartz, quartz-amphibole-rutile, quartz-epidote-zeolite, quartz-zeolite, and epidote veins are present in the BAG (e.g., Sections 209-1271B-3R-1 and 5R-1). Whereas these veins are volumetrically insignificant (Table T3), their variable mineral compositions may indicate multiple episodes of veining and fluid flow under a range of conditions. Talc veins are especially well developed in the uppermost 17 m of Hole 1271B.

Discussion

Three major distinct lithologies are present in Hole 1271B: (1) serpentinized harzburgite and dunite, (2) BAG, and (3) amphibole-bearing dunite. In addition, there are subsidiary gabbros distributed throughout the core that are volumetrically insignificant. The distribution of these lithologies is outlined above in the summaries of vein alteration and background alteration where, for clarity, they were discussed separately. Here, we combine their metamorphic features into a coherent history of alteration and deformation for Hole 1271B.

F29. Incomplete serpentinization of dunite, p. 70.
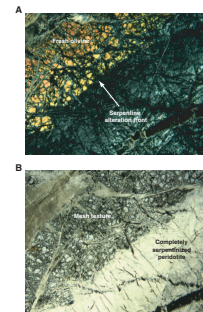
F30. Vein mineralogy, Hole 1271B, p. 71.
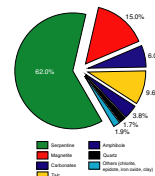
Brown Amphibole Gabbro and Amphibole-Chlorite Schists

The earlier parageneses that can be recognized in the BAG are brown amphibole, plagioclase, and Fe-Ti oxides. On textural evidence, it is not possible to discern if the amphibole is igneous or is an alteration product replacing primary pyroxene. The absence of pyroxene, even in BAG that has abundant apparently fresh plagioclase, could indicate that (1) brown amphibole is a primary phase or (2) the BAG underwent pervasive amphibolite-facies alteration during which plagioclase was stable. The partial breakdown of primary Fe-Ti oxides to rutile and quartz in interval 209-1271B-5R-1, 12–14 cm, is consistent with relatively high temperature alteration but does not rule out a magmatic origin for the brown amphibole. Late, secondary green amphibole along with chlorite and minor talc is present in varying proportions in BAG.

In mylonitic BAG the brown amphibole has been deformed in a ductile manner. In these mylonites, brown amphibole was deformed as large porphyroclasts and recrystallized to neoblasts (Fig. F31A, F31B) or as neoblast bands with intense grain size reduction (in the margins of Fig. F31A and F31B). Although plagioclase in these samples is completely altered, textural observations indicate that plagioclase underwent a similar type of deformation before static breakdown to sericite, quartz, and secondary plagioclase (the secondary plagioclase must have relatively high CaO to account for the whole-rock CaO of 11.7 wt% compared to the amphibole CaO content of 12.5 wt%). This is suggested by large altered plagioclase grains that retain the polysynthetic twinning of plagioclase porphyroclasts and are embedded in a matrix of smaller neoblasts of (altered) plagioclase (interval 209-1271B-14R-1, 25–29 cm) (Fig. F31). These observations indicate that the BAG underwent ductile deformation localized in shear bands affecting brown amphibole and plagioclase. Following ductile deformation, plagioclase in these shear bands was statically altered to sericite, quartz, and secondary plagioclase.

Most BAG samples record later pervasive, brittle, retrograde alteration. This event led to the breakdown of brown amphibole along schistose bands or veins in BAG. In places this breakdown is static, but more commonly it is pervasive, in particular in schistose amphibole-chlorite bands. Retrogression of brown amphibole formed fine-grained, fibrous aggregates of green amphibole and chlorite that were synkinematically deformed, likely under greenschist facies conditions (Fig. F31D, F31E). The amphibole-chlorite schist locally shows a well-developed foliation and folding of the schistose fabric.
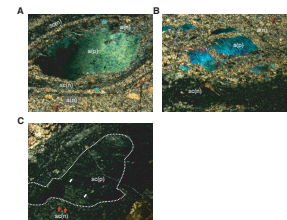
Troctolites and Amphibole-Bearing Dunite

Rare troctolites show textural evidence for static plagioclase breakdown to chlorite and amphibole in the proximity of olivine. We tentatively relate plagioclase breakdown to retrograde greenschist facies assemblages.

Amphibole-bearing dunites are the most common olivine-bearing rock type other than peridotite. They are found in close proximity to BAG. The earliest secondary phase that can be observed in these rocks is coarse amphibole crystals in textural equilibrium with olivine (Fig. F32A). These large amphibole crystals fill the intergranular space between round olivine grains and display continuous extinction (Fig. F32A). There is no evidence that the amphibole is replacive after a specific primary igneous phase.

Amphibole-bearing dunites underwent high-temperature ductile deformation, manifest in elongated porphyroclasts of deformed amphi-

F31. Evolution of BAG during deformation, p. 72.

F32. Deformation-metamorphism path in amphibole-bearing dunite, p. 74.
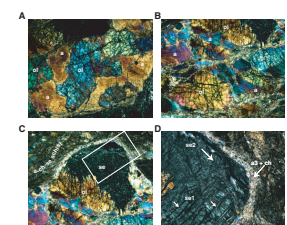
bole surrounded by a mantle of fine-grained amphibole neoblasts (Fig. F32B). The ductile overprint in olivine is weak (wavy extinction and kink bands), indicating deformation temperatures <900°C. Sharp boundaries between olivine and amphibole suggest that both phases were in equilibrium during ductile deformation. We tentatively relate ductile deformation in amphibole-bearing dunites to the same deformation event recorded in BAG because amphibole did not break down during deformation in either lithology. These observations indicate that BAG and amphibole-dunite underwent ductile deformation in the high-temperature amphibolite facies, with variable strain localization into mylonitic bands, in both lithologies.

Most amphibole-bearing dunites record greenschist facies retrogression. This resulted in the alteration of coarse, early amphibole to a retrograde assemblage of fibrous green amphibole and chlorite. As this retrograde assemblage formed, it propagated along grain boundaries and along fractures in the surrounding olivine (Fig. F32C, F32D). These textural relations indicate brittle conditions during greenschist overprint. Greenschist facies metamorphism appears to be contemporaneous with serpentinization because the partial breakdown of early amphibole to secondary amphibole + chlorite and serpentinization are both developed near mylonitic bands composed of the retrograde assemblage (Fig. F32C, F32D). During retrogression, serpentinized olivine porphyroclasts were partially replaced by coronas of secondary amphibole and chlorite (Fig. F32D). In addition, olivine porphyroclasts are locally transformed to amphibole needles growing topotactically on serpentine (Fig. F32E). Early amphibole porphyroclasts were transformed to fibrous amphibole and chlorite along retrograde, sheared amphibole-chlorite bands (Fig. F32F). However, elsewhere in the amphibole-bearing dunite (e.g., interval 209-1271B-13R-1, 20–24 cm) there is evidence for static replacement of olivine by the retrograde mineral assemblage. Here, former grain boundaries of olivine, outlined by rims of magnetite, are still visible in the retrograde mineral assemblage of secondary amphibole, chlorite, and sericite (Fig. F27). This suggests that in zones of limited resistance to deformation dynamic alteration processes actively altered early amphibole and olivine. Where shear strength was limited, for example in the strong, semirigid matrix of fresh olivine, alteration and overprinting was static.

In terms of texture and mineralogy, this retrograde event in amphibole-bearing dunites is consistent with the alteration and deformation history preserved in amphibole-chlorite bands replacing BAG. The strain displayed in both units is consistent with high-temperature shearing followed by, or continuing as, synkinematic to static greenschist facies alteration, resulting in the breakdown of early amphibole into discrete zones of retrograde secondary amphibole that locally form amphibole-chlorite schists.

Harzburgite and Dunite

The relationships between serpentinization in harzburgite and dunite and the metamorphic events preserved in the other lithologies are not clear. Some serpentinization clearly predates the alteration of former gabbroic dikelets in the amphibole-bearing dunite, as veins composed of secondary amphibole + chlorite + sericite are observed crosscutting serpentine veins (Fig. F33). However, these amphibole veins are subsequently cut by serpentine veins that resemble the earlier serpentine vein generation. The relative timing of serpentinization and

F33. Serpentinization of olivine and later alteration, p. 76.
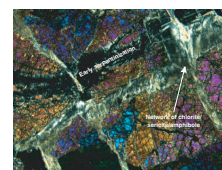
synkinematic greenschist facies alteration is difficult to distinguish, and these events may be synchronous.

Evidence for syndeformational serpentinization is limited to discrete areas that show deformation fabrics sharply juxtaposed with essentially strain-free areas of serpentinite. Early serpentinization followed by greenschist facies alteration, which was contemporaneous with a second serpentinization event, could account for the textural relationships observed in the serpentine and the complex crosscutting relationships observed between serpentine and the greenschist facies assemblages. Multiphase serpentinization is also consistent with the complex crosscutting relationships between the various generations of serpentine veins in Hole 1271B (cf. "Metamorphic Veins," p. 14, above).

## Discussion of Phase Relations at Site 1271

The presence of incompletely serpentinized dunites and minor harzburgites at Site 1271 provides the opportunity to speculate about potential serpentinization reaction paths. Field and experimental studies suggest that serpentinization at low to moderate temperature (<250°C) is a nonequilibrium process during which dissolution of olivine proceeds at rates faster than precipitation of talc and serpentine (e.g., Nesbitt and Bricker, 1978; Martin and Fyfe, 1970).

Figure F34A displays a Mg-Ca-Si-O-H mineral-fluid phase diagram for 200°C and 500 bar. The fluid composition will be driven toward the stability fields of serpentine and brucite, which represent the lowest-energy mineral assemblage (e.g., Hemley et al., 1977). The proposed reaction path (black arrow in Fig. F34A) is strongly curved, owing to rapid dissolution of olivine and consumption of acidity, followed by a shoaling of the trend due to dissociation of orthosilicate at high pH. The last part of the proposed reaction path is controlled by the forsterite dissolution boundary. At pH = 10 and silica concentrations similar to that of seawater, the Lost City vent fluids (Kelley et al., 2001), when respeciated at 200°C and 500 bar, have aqueous silica activities that put them right on the serpentine/brucite boundary, suggesting that the Lost City fluid is saturated in both phases. Also shown in Figure F34A is a schematic reaction path for fluids from a harzburgite-seawater interaction experiment (Seyfried and Dibble, 1980) that trends toward the chrysotile/brucite boundary. In contrast, fluids from a lherzolite-seawater experiment at 200°C and 500 bar (Janecky and Seyfried, 1986) do not evolve toward brucite saturation because the high abundance of pyroxenes keeps the fluid pH low and the silica activity of the fluids high (Fig. F34A).

The effect of pyroxene on solution chemistry is even stronger at higher temperatures (>250°–300°C), where pyroxenes react faster than olivine (Martin and Fyfe, 1970; Allen and Seyfried, 2003). Figure F34B demonstrates that high-temperature (365°C) black smoker fluids from the Logatchev and Rainbow peridotite-hosted hydrothermal systems (e.g., Charlou et al., 2002), when respeciated at 400°C and 500 bar, are pinned by fluid saturation in metastable pyroxene and that talc and possibly tremolite should form at the expense of pyroxene. As long as pyroxenes are present (and dissolve fast) the pH of the interacting fluids is low and the silica activity high (cf. Allen and Seyfried, 2003). Only when the fluid is no longer pyroxene saturated can it evolve to higher pH and lower silica activity.

These mineral-fluid phase relationships are relevant for the interpretation of the serpentine-brucite and olivine-amphibole-talc assemblages observed in cores from Site 1271. A possible interpretation of the rela-

F34. Mineral/fluid phase diagram, p. 77.
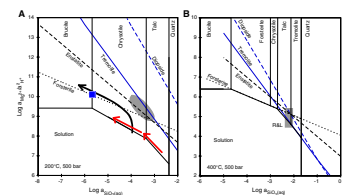
tively fresh dunites with rare talc-altered orthopyroxene pseudomorphs is that these rocks reacted with hydrothermal fluids at high temperatures (>300°C) where orthopyroxene reacts faster than olivine. The proximity of mafic material (amphibolites) to intervals of unaltered dunite may suggest that the presence of pyroxene and amphibole kept the silica activity of the interacting fluids high so that serpentinization of olivine was inhibited. Formation of talc after olivine is thermodynamically favored (Fig. F34B) but kinetically sluggish (e.g., Nesbitt and Bricker, 1978). Replacement of orthopyroxene by talc, on the other hand, is commonly observed in alpine and abyssal serpentinites (e.g., Aumento and Loubet, 1971; Hostetler et al., 1966). As the system moves toward lower silica activity after pyroxenes are exhausted, talc that had formed during initial alteration will react to serpentine. This explains the scarcity—or complete lack—of talc as part of the background alteration in completely serpentinized rocks from Site 1271.

The brucite-bearing dunites (and minor harzburgites) from the bottom of Holes 1271A and 1271B require a different genetic model (see Fig. F34A). The phase relations indicate that these lithologies reacted with fluids of high pH and low silica activity. Such fluids are generated when alteration is controlled by rapid olivine dissolution and relatively sluggish hydrous mineral precipitation. Thermodynamically and kinetically, conditions for brucite-serpentine formation are favorable at low temperatures and in the absence of pyroxenes. The abundance of brucite at Site 1271 may suggest that the circulating fluids are dominantly high pH and low silica activity, which could be explained if the basement at Site 1271 consists dominantly of dunite.

STRUCTURAL GEOLOGY

We present the results of detailed structural observations of the core recovered from two holes (1271A and 1271B) drilled at Site 1271 followed by a discussion of preliminary interpretations of the structural history. Holes 1271A and 1271B are located ~90 m apart and show similar structural features (Fig. F35). They are, therefore, discussed together in this section. Four categories of observations were recorded in spreadsheet format including crystal-plastic deformation, magmatic textures, brittle deformation, and orientation of metamorphic veins. These were supplemented by microstructural observations in 43 thin sections. The relatively high degree of alteration required that many high-temperature features be observed only in pseudomorphs, leading to ambiguity in their interpretation. Details of the structural classification scheme for each feature are given in "Structural Geology," p. 9, in the "Explanatory Notes" chapter.

Crystal-Plastic Deformation

Holes 1271A and 1271B record similar events corresponding to an extended history of ductile deformation under varying thermal conditions. Crystal-plastic deformation textures in the 45-m section of largely undeformed dunite recovered from Hole 1271A contrasts with the 104-m section of variably deformed dunite, dunite with intergranular mafic material, harzburgite, orthopyroxene-bearing dunite, and spinel-bearing and orthopyroxene-bearing dunite recovered from Hole 1271B (Fig. F36). The perceived differences between these holes, however, may be due to the poor recovery and lack of crystal-plastic defor-

F35. Locations of shear zones and impregnated horizons, p. 78.
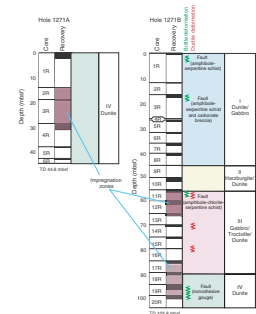
F36. Crystal-plastic deformation intensities, p. 79.
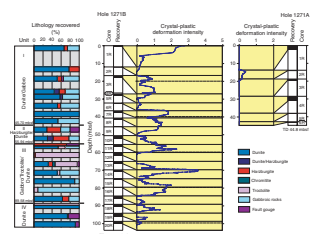
mation indicators such as pyroxene grains and spinel concentrations in Hole 1271A. Where core containing magmatic veins was recovered in Hole 1271A, deformation patterns appear similar to those of Hole 1271B.

High-Temperature, Low Strain–Rate Mantle Fabrics

The earliest evidence of crystal-plastic deformation in the Hole 1271A and 1271B cores is found in the peridotites and comprises textures commonly associated with high-temperature, low strain–rate mantle flow. At Site 1271, spinel foliations suggest that this phase of deformation may have been concurrent with melt migration and the formation of dunite with local chromite concentrations. Peridotites recovered from Hole 1271A consist largely of dunite with very minor harzburgite. There is little evidence of an early deformation history in the dunites. However, rapid strain recovery in olivine in monomineralic dunite at high temperature would largely eliminate evidence of any early deformation history. In intervals where pseudomorphed orthopyroxene porphyroclasts are present in the orthopyroxene-bearing dunites and harzburgites, evidence of an early high-temperature, low strain–rate deformation event is preserved.

The total deformation intensity in harzburgite and orthopyroxene dunite is low in both Holes 1271A and 1271B (Hole 1271 average = 0.3 and Hole 1271B average = 0.07) (Fig. F37). Protogranular and proto-intergranular textures predominate in these lithologies (Fig. F38A). Orthopyroxene dunite and spinel- and orthopyroxene-bearing dunite record higher degrees of crystal-plastic deformation than the harzburgites, even though they contain significantly fewer deformation markers. There is physical evidence in several Hole 1271B orthopyroxene-bearing dunites that porphyroclastic textures developed prior to dunite formation. Elongated orthopyroxene porphyroclasts rimmed by vermicular chrome spinel are present in orthopyroxene dunites. Asymmetry of orthopyroxene porphyroclasts indicates normal sense of shear along a plane dipping 20°–30°. However, if the sample was significantly rotated after high-temperature deformation, it is possible that this was a reverse sense shear zone. Spinel is concentrated at the long ends of the grains in a manner that resembles asymmetric porphyroclast tails (Fig. F38B, F38C). The delicate vermicular spinel rimming the pyroxene is unlikely to have survived the deformation that formed porphyroclastic textures, indicating that spinel crystallized later. Higher degrees of high-temperature deformation in orthopyroxene dunites compared to harzburgites in Holes 1271A and 1271B may be evidence for strain localization in horizons of concentrated melt flow and dunite formation in the shallow mantle (e.g., Kelemen and Dick, 1995).

Well-developed spinel foliations were measured in dunites from both Hole 1271A and 1271B (e.g., Figs. F38D, F39A). These foliations define a girdle relative to paleomagnetic north in a lower hemisphere stereographic projection (Fig. F40). This contrasts with porphyroclastic foliations in Hole 1268 harzburgites (Fig. F77, p. 134, in the "Site 1268" chapter), which define a local concentration of points in the stereographic projection. Site 1271 dunite spinel foliations may record folding not seen in the enclosing peridotite wallrocks. This is common in podiform dunites in ophiolitic peridotite massifs (e.g., Ramp, 1961) and may reflect a very different rheology in the dunites during their formation.
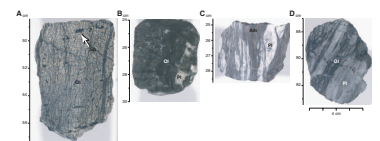
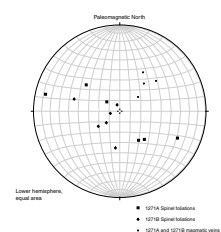**F37.** Lithology, deformation fabrics, and crystal-plastic deformation, p. 80.
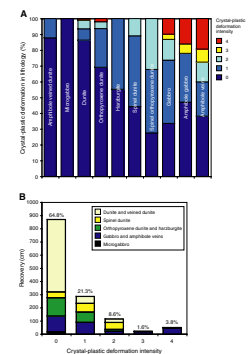
F38. Peridotite textures, Site 1271, p. 81.
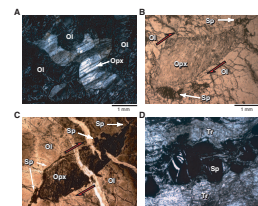
F39. Examples of crystal-plastic deformation, p. 82.

F40. Orientation of magmatic veins and spinel foliations in dunite, p. 83.

Subsolidus Crystal-Plastic Deformation

Gabbro and peridotite samples drilled at Site 1271 experienced distributed crystal-plastic deformation over a wide temperature range, beginning in granulite facies and continuing along a down-temperature path through amphibolite facies. Strain appears to have been partitioned into gabbro intrusions and veins.

Hole 1271A and 1271B dunites and harzburgites host extensive gabbroic intrusions that form magmatic net vein complexes. Because these veins were intensely altered to amphibole, chlorite, and talc, their original composition is uncertain (see "Igneous and Mantle Petrology," p. 2). However, several veins preserve sufficient primary mineralogy to be identified as troctolites and troctolitic gabbros (Figs. F39B, F41A). Several of these samples are undeformed or exhibit evidence for weak crystal-plastic deformation, including minor recrystallization along the boundaries of plagioclase (Fig. F41B) and clinopyroxene grains and formation of deformation twins in plagioclase. Other veins are strongly deformed, such as those in interval 209-1271B-11R-1 (Piece 17, 87–93 cm) (Fig. F41C, F41D). This olivine amphibole mylonite was highly deformed at granulite or upper-amphibolite facies conditions during which olivine was dynamically recrystallized into a fine-grained aggregate.

BAG (see "Igneous and Mantle Petrology," p. 2) underwent varying degrees of crystal-plastic deformation. An example is shown in Figure F39C (interval 209-1271B-14R-1, 25–30 cm). This mylonite contains alternating layers of fine-grained brown amphibole and fine-grained high-relief minerals (presumably prehnite, zoisite, and/or hydrogrossular replacing plagioclase). These layers enclose coarse brown amphibole augen (Fig. F41D) that are commonly weakly deformed, with bent crystals and/or undulatory extinction.

Textures in the BAG suggest that the main phase of crystal-plastic deformation occurred under granulite facies conditions and that brown amphiboles are secondary, replacing pyroxenes. Samples 209-1271B-18R-1, 20–23 cm, and 16R-1, 24–27 cm, contain veins of brown amphibole at right angles to the brown amphibole bands that define the mylonitic foliation (Fig. F41E, F41F). Within these veins, the amphibole fibers are often randomly oriented, suggesting growth under dominantly static conditions. Other samples contain textural evidence for dominantly static overprinting of granulite facies deformation textures by colorless amphibole. Secondary colorless amphibole in Sample 209-1271B-14R-1, 32–35 cm, replaces a stretched pyroxene augen and the enclosing foliated groundmass (Fig. F42). The amphibole in the augen has cleavage at right angles to the foliation, even in the tail of the porphyroclast.

Samples 209-1271B-17R-1, 17–19 cm, and 18R-1, 114–117 cm, display textures that suggest that crystal-plastic deformation continued during amphibolite-grade metamorphism. Amphiboles in Sample 209-1271B-17R-1, 17–19 cm, contain arrays of parallel subgrains, suggesting recrystallization due to crystal-plastic strain (Fig. F43A). This sample also contains arrays of fine-grained, fibrous, secondary amphibole, talc, and chlorite that formed during deformation under greenschist facies conditions (Fig. F43B, F43C). These textures formed concurrent with minor cataclasis and are discussed in greater detail in "Brittle Features," p. 23, below. The last-formed crystal-plastic deformation textures observed at Site 1271 include minor shearing along late amphibole veins (Fig. F43D).
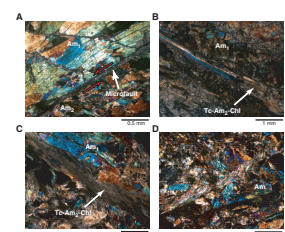
F41. Deformed and undeformed gabbroic veins, p. 84.
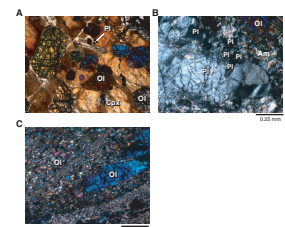
F42. Gabbro mylonite pseudomorphed by amphibole, p. 86.
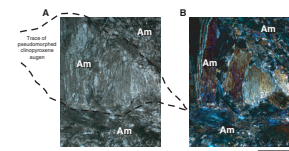
F43. Late brittle-ductile deformation in troctolitic gabbros and dunites, p. 87.

Distribution and Total Intensity of Crystal-Plastic Deformation

The dunites and peridotites from Site 1271 lack the porphyroclastic deformation textures found in the peridotite samples from Holes 1268A, 1270D, and 1270C. Despite this, the overall crystal-plastic deformation intensity is relatively high, with 14% of the rocks having deformation intensities >2. Only 6.7% of the rocks from Hole 1268A have intensity >2. Hole 1271A and 1271B gabbros are substantially more deformed than those at Sites 1268 and 1270. Ductile strain at Site 1271 appears to have been preferentially localized into gabbroic veins, as it was at Sites 1268 and 1270. Downhole, the distribution of crystal-plastic deformation is quite variable, indicating that deformation was localized and not penetrative as it commonly is in mantle peridotites with well-developed porphyroclastic fabrics.

Magmatic Textures

The primary magmatic features that are observed at Site 1271 include one impregnation horizon in Hole 1271A and two impregnation horizons in Hole 1271B (Fig. F35). These comprise dunite and orthopyroxene-bearing dunite containing variable proportions of gabbroic material. Interstitial clinopyroxene and plagioclase are interpreted to be cumulate phases crystallized from melt migrating along olivine grain boundaries, forming "impregnated" peridotites. Some sections of Hole 1271B that contain high proportions of gabbroic material (as much as 40% in Unit III; see "Igneous and Mantle Petrology," p. 2) have the appearance of gabbroic cumulates. The textures in the impregnated sections are not uniform and may record decreasing temperatures during multiple impregnation events.

In Sections 209-1271A-3R-1 and 4R-1, the impregnating material is interstitial to olivine in the dunite, similar to near-equilibrium melt textures observed in laboratory experiments (Fig. F44A–F44C). The distribution of impregnating material on the grain scale, however, appears patchy, which contrasts with relatively uniform melt distributions observed in laboratory experiments (e.g., Faul, 2000). Within other intervals of Section 209-1271A-4R-1 (e.g., Pieces 11–13) a second generation of interstitial gabbroic material with irregular boundaries overprints the earlier formed textures (Fig. F44D).

Hole 1271B has two impregnation horizons (Fig. F35). Textures in the upper horizon suggest multiple impregnation events that followed formation of the dunite. In interval 209-1271B-11R-1, 110–113 cm, an early coarse-grained pyroxenite vein has been partially impregnated by a second crosscutting generation of gabbroic material (Fig. F45). The impregnation textures observed in Cores 209-1271B-11R to 13R do not resemble those of equilibrated partial melts. Olivine grains in the most heavily impregnated intervals are not in contact with one another. Figure F46 shows olivine that is angular in appearance, implying disaggregation of the dunite during liquid infiltration. The boundaries between olivine crystals and impregnating material are relatively sharp, but it is possible that olivine reacted with the liquid (see "Igneous and Mantle Petrology," p. 2). Figure F47 (interval 209-1271B-12R1, 42–54 cm) shows that the impregnated horizon is crosscut by a later generation of possibly more evolved gabbro dikes or veins that are very abundant within several intervals. These late magmatic veins (Fig. F39D) appear
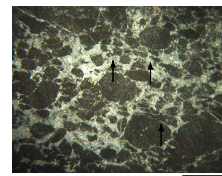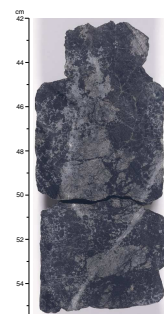
F44. Impregnation textures, p. 88.
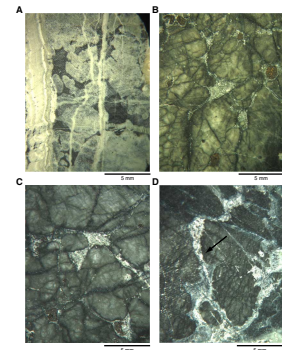
F45. Pyroxenite vein cut by late gabbroic vein, p. 89.
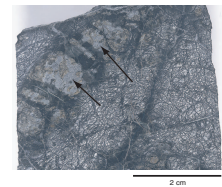
F46. Impregnated dunite with gabbroic material, p. 90.

F47. Impregnated dunite crosscut by a later gabbroic vein, p. 91.

to localize ductile shear deformation in a similar fashion to the magmatic veins observed in Holes 1270C and 1270D.

Textures in portions of the lower impregnation horizon (Cores 209-1271B-19R and 20R) resemble experimentally produced melt migration textures (similar to those in Cores 209-1271A-3R and 4R). The volume fraction of impregnating material is relatively low, in contrast to the upper horizon. Figure F48A shows a large olivine crystal outlined by the surrounding impregnating material with intragranular, rounded spinel grains. Irregular veinlike impregnation textures are also present in the lower impregnation horizon over interval 209-1271B-19R-1, 10–16.5 cm (Fig. F48B). These observations indicate that this horizon may have been infiltrated several times by increasingly evolved liquids.

Orientations of two magmatic veins from Hole 1271A and two from Hole 1271B were measured using methods described in "Structural Geology," p. 9, in the "Explanatory Notes" chapter. The measurements are restored to a common orientation by rotation in the core frame of reference such that the azimuth of the stable remnant magnetization points north. The reorientation of the veins using paleomagnetic data is discussed in "Structures in Peridotite and Gabbroic Intrusions," p. 8, in "Mantle Upwelling, Melt Transport, and Igneous Crustal Accretion" in the "Leg 209 Summary" chapter. The reoriented data are plotted on a lower hemisphere stereonet in Figure F40. Poles to foliation planes are clustered relatively tightly at an orientation striking northwest and dipping ~60° southwest in the reference frame we used to plot the data, ~45° from the mean orientation of the spinel foliation measured in Hole 1271B (see "Spinel Fabrics" below).

Spinel Fabrics

Spinel foliations were measured in spinel-rich dunite intervals of Site 1271 core. The foliations were measured on six 4- to 5-cm-long quarter cores that were cut from the working half of cores from Hole 1271A. In Hole 1271B, it was possible to measure spinel foliations directly on the archive half of the core. Spinel foliation orientations corrected with paleomagnetic measurements are plotted in a common orientation reference frame in Figure F40. The orientations in Hole 1271A were measured over a 10-m interval beginning at Section 209-1271A-3R-1 (Piece 11, 60 cm) and ending at 4R-1 (Piece 7C, 126 cm). Poles to spinel foliation planes measured in Hole 1271A appear to loosely fall on a great circle with a near-horizontal pole trending northeast in our common reference frame. Spinel foliations in Hole 1271B were measured over an interval from Section 209-1271B-5R-1 (Piece 9, 42 cm) to 20R-1 (Piece 16, 81 cm). Poles to spinel foliation planes measured in Hole 1271B are more clustered but could lie within the great circle defined by spinel foliations in Hole 1271A. This interval covers the drilled depth range from 30 to 102 mbsf.

Cross-Fiber Serpentine Foliation

Foliation in serpentinite defined by anastomosing sets of serpentine and magnetite veins is present in varying degrees through much of the Site 1271 core. The most pronounced example of serpentine foliation is the yellow- and black-striped serpentinized dunite recovered from the upper half of Hole 1271A (e.g., intervals 209-1271A-1R-1, 52–142 cm, and 1R-2, 0–35 cm) (Fig. F49B). The strong subvertical foliation over this interval is defined by a mixture of planar and anastomosing ser-

F48. Textures from the lower impregnation horizon, p. 92.
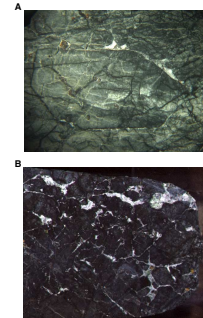
F49. Metamorphic veins cutting dunites, p. 93.
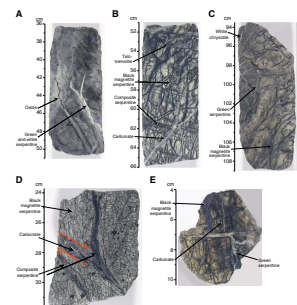
pentine and magnetite veins that have largely replaced the serpentinized dunite host rock. Serpentine fibers composing veins are commonly oriented perpendicular to vein walls and are not deformed. Veins defining the striped texture are more planar and less anastomosing than veins forming cross-fiber serpentine foliation in serpentinized harzburgite from Sites 1268 and 1270. The amplitude of anastomosing waves in the foliation at these locations appears to be a function of the size and concentration of pyroxene porphyroclasts and the degree to which veins are deflected around them. Veins at Site 1270 are likely more planar due to the limited number of pyroxene porphyroclasts in the dunite. This fabric appears to be a variant on ribbon texture serpentine as described by O'Hanley (1996) and is produced by dilational fracturing during serpentinization rather than shear deformation. It is unknown if this strong foliation mirrors a previous crystal-plastic deformation fabric.

Cross-fiber serpentine foliation in Hole 1271B appears in intervals of nonimpregnated harzburgite and dunite. Where cross-fiber serpentine foliation appears in dunite, foliation and veins are dominantly planar, as was observed in the upper portion of Hole 1271A (e.g., interval 209-1271B-17R-1, 127–135 cm). Where serpentine foliation appears in harzburgite, foliation and veins tend to form anastomosing waves similar to those observed in Hole 1268A (e.g., intervals 209-1270B-10R-1, 93–127 cm, and 13R-1, 69–74 cm). Serpentine fibers are most commonly aligned perpendicular to vein walls, indicating formation of the foliation by dilatant fracturing rather than shear deformation.

Brittle Features

Amphibolite and Greenschist Semibrittle Shear Zones

Shear zones composed of schistose amphibole and chlorite schist overprint some gabbroic veins in Holes 1271A and 1271B. Deformation occurred during alteration of the primary components of gabbroic intrusions to pale brown and colorless amphibole (see "Metamorphic Petrology," p. 9). Textures of amphibolite range from randomly oriented aggregates of bladed crystals ranging 0.1–2 mm in size (e.g., Sample 209-1271B-12R-1, 126–131 cm) to strongly foliated schistose arrays of fine-grained (<0.01 mm) amphibole (e.g., Sample 12R-1, 126–131 cm). Random aggregates of bladed crystals are interpreted to have grown under dominantly static conditions. Foliated schistose amphibole is interpreted to have grown during localized shear deformation. Highly localized strain during amphibolite alteration is suggested by variations between static and highly schistose textures on the centimeter scale. This contrasts with observations of gabbroic veins in Holes 1270C and 1270D, in which amphibolites are deformed in nearly all occurrences.

Sample 209-1271B-11R-1, 88–91 cm, contains deformation textures and mineral assemblages that suggest semibrittle deformation at amphibolite and greenschist facies conditions that overprints crystal-plastic deformation. This sample contains foliation-parallel bands of finely recrystallized olivine mylonite, intermediate grain–size amphibole, fine-grained schistose amphibole, and schistose serpentine. Intermediate grain–size amphibole comprises bladed to highly elongate pale brown and slightly pleochroic crystals (up to 0.5 mm) aligned subparallel to the shear foliation (Fig. F50). Fine-grained colorless amphibole ranges 0.03–0.06 mm in size and is elongate parallel to the shear foliation (Fig. F50). Serpentine bands comprise schistose fibrous serpentine

F50. Fine-grained amphibole and serpentine schist, p. 94.

with a long dimension ranging 0.02–0.05 mm and a short dimension ranging 0.01–0.03 mm. Serpentine schist appears to have formed concurrently with fine-grained amphibole during deformation. Intermediate grain–size amphibole may have formed concurrently with or following crystal-plastic deformation of olivine. Fine-grained colorless amphibole and schistose serpentine likely formed during lower-amphibolite to greenschist facies deformation following crystal-plastic deformation. This indicates a prolonged strain history under conditions of progressively decreasing temperature.

Serpentine-Chlorite Schist

Two intervals of core in Hole 1271B contain semibrittle shear zones composed of schistose serpentine, chlorite, clay minerals, and possibly hydrogrossular (Figs. F51, F52). These include several pieces in the upper portion of the hole (intervals 209-1271B-1R-1, 1–16 cm, and 3R-1, 18–22 cm) and within Core 11R near strongly deformed amphibole schist (discussed above) (intervals 11R-1, 14–17 cm, and 53–57 cm). Strain was likely accommodated by diffusive mass transfer and cataclasis in the presence of aqueous fluid at temperatures <300°C based on textures indicating syndeformation, subgreenschist-grade alteration. Serpentine-chlorite schist zones may represent a low-temperature deformation overprint on the amphibole schist described above, due to continuous deformation at decreasing temperature.

Brittle Faults

The lower part of Hole 1271B experienced intense brittle deformation late in the deformation history of Site 1271. Several intervals of partially cohesive fault gouge are present in Cores 209-1271B-19R and 20R (intervals 19R-1, 3–4 cm, 49–50 cm, 72–73 cm, 65–73 cm, and 96–97 cm, and 20R-1, 34–35 cm). Gouges are matrix-supported breccias with gray clay- and/or serpentine-rich matrices. Clasts are subrounded to angular, altered serpentinite ranging 0.1–0.8 cm in size. Breccias also contain rare larger clasts of serpentinite (5 cm diameter). Intervals of core bordering gouge zones are variably fractured, including conjugate sets of planar to slightly anastomosing magnetite-filled shear fractures with 1 to <0.2 cm offset. Slickenfibers visible on fracture surfaces suggest dip slip to oblique slip but do not indicate an unambiguous shear sense. Intervals of core bordering gouge zones also appear to have a higher degree of clay alteration of serpentinite than other intervals in Hole 1271B. It is likely that the gouge intervals represent splays of a major brittle fault system. It is possible that recovery from gouge zones was low and that only a small percentage of the true thickness of the fault zone was sampled by drilling. It is also likely that characteristics of the gouge were modified by the drilling process, and thus deformation observed in the gouge may partly be a consequence of drilling.

Other brittle features recovered at Site 1271 include cohesive carbonate-matrix breccias in intervals 209-1271B-3R-1, 19–22 cm, and 48–55 cm. These breccias are composed of angular to subrounded clasts of serpentinite and rare chrome spinel crystals supported by a partially recrystallized, micritic carbonate matrix. Breccias are interpreted to be of tectonic rather than sedimentary origin because of fibrous bands and a weak foliation in the carbonate matrix (Fig. F53).

Minor fractures and small fault zones are present throughout Holes 1271A and 1271B, but in most cases do not appear to represent a signif-

F51. Low-temperature schist, p. 95.

F52. Serpentine-chlorite schist from a semibrittle shear zone, p. 96.

F53. Carbonate-matrix fault breccia, p. 97.

icant degree of shear deformation. Minor faults are commonly associated with serpentine and carbonate veins. Slickenfibers, where visible on small faults, typically indicate dip slip but no unambiguous shear sense.

Downhole Distribution of Brittle and Semibrittle Deformation

Figures **F54** and **F55** show the downhole distribution of brittle deformation intensity at Site 1271. The intensity of brittle deformation was measured using the intensity scale outlined in **"Structural Geology,"** p. 9, in the "Explanatory Notes" chapter. Several brittlely and semibrittlely deformed samples were recovered in Hole 1271A, but no highly deformed samples or concentrations of brittle deformation were recognized in this hole (Fig. **F54**).

Hole 1271B contains three zones of concentrated brittle deformation (Fig. **F55**). The first zone is composed of brittlely deformed rocks in Sections 209-1271B-1R-1 and 3R-1 that include amphibole schist, serpentine schist, and carbonate-matrix fault breccia. The second zone of brittle deformation is in Core 209-1271B-11R, where amphibole schist and serpentine schist shear zones overprint high-temperature ductile deformation associated with gabbroic intrusion. The last brittle shear zone in Hole 1271B is in Cores 209-1271B-18R, 19R, and 20R, where concentrated, late, pure brittle deformation forms noncohesive fault gouge and highly fractured rocks.
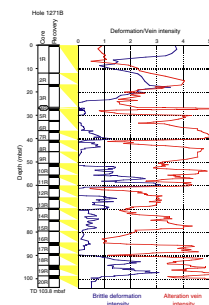
Alteration Veins

The BAGs contain a few quartz and quartz-amphibole-rutile veins. The dunites/harzburgites show extensive veining throughout both Holes 1271A and 1271B. Veins in peridotite include both continuous, planar veins and sigmoidal, discontinuous veinlets and range in from a few millimeters to 20 cm in length and from 0.1 mm to 0.5 cm in width. There are several generations of veins, but the veins are dominantly serpentine with subsidiary talc-tremolite, carbonate, and oxide veins. The relative timing of all of these vein sets is difficult to determine. However, a simplified order is as follows. The first generation is an almost ubiquitous, dense, anastomosing network of black serpentine + magnetite veins (Fig. **F49B–F49E**). This network is overprinted by later, less pervasive generations of green and white serpentine (picrolite) veins, composite black (exterior) and green (interior) serpentine/magnetite banded veins, white chrysotile veins, talc-tremolite veins, and late carbonate/aragonite and oxide veins. Figure **F49** shows various examples of the different vein sets and their crosscutting relationships in Sections 209-1271A-1R-1 and 1R-2 and 209-1271B7R-1 and 2R-1.

Brittle faults offset both the anastomosing network of black serpentine + magnetite veins and the later composite black and green serpentine veins in intervals 209-1271B-7R-1, 24–32 cm, and 2R-1, 4–10 cm (Fig. **F49D, F49E**). Section 209-1271B-2R-1 (Piece 2) shows later green and white serpentine and carbonate veins that apparently followed a fault, and therefore postdate an earlier brittle event. This relationship is consistent with a complex series of serpentine veining events occurring synchronously with brittle faulting. Many of the larger green and white serpentine veins have slickenfibers on exposed surfaces on the edges of the pieces. These suggest shear deformation associated with the formation of these later serpentine veins. The late carbonate veins probably

F54. Brittle deformation and alteration vein intensities, Hole 1271A, p. 98.
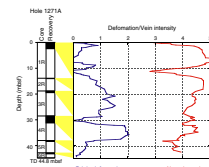
F55. Brittle deformation and alteration vein intensities, Hole 1271B, p. 99.

formed at shallow levels, associated with seawater alteration. A more detailed discussion of the mineralogy of the alteration veins can be found in "Metamorphic Petrology," p. 9.

The intensity of veins was measured using the intensity scale outlined in "Structural Geology," p. 9, in the "Explanatory Notes" chapter. The intensity of these veins is a measure of their average frequency in a 10-cm piece of core. The total intensity of alteration veining with depth for Holes 1271A and 1271B is shown in Figures F54 and F55. The alteration vein intensity in both holes is high, with most of the dunites/harzburgites being pervasively net veined with vein intensities of 3–5. The lower alteration vein intensities of 1–2 in Hole 1271B correspond to occurrences of the BAG, for example, in Sections 209-1271B-3R-1 and 5R-1 (20–30 mbsf), to the troctolites and gabbros of Unit III from Sections 11R-1 to 18R-1 (56–89 mbsf), and to the fault rocks recovered in Section 1R-1 (0–12 mbsf).

Orientation of Veins and Brittle Fractures

The orientation of veins and brittle fractures was measured using the procedures outlined in "Structural Geology," p. 9, in the "Explanatory Notes" chapter. Twelve brittle fractures and shear zones were measured in Hole 1271A, and nine were measured in Hole 1271B. Dips of brittle features range 0°–85° in Hole 1271A and 16°–85° in Hole 1271B. The variation of the dip of the alteration veins with depth for Holes 1271A and 1271B is shown in Figure F56. Only 12 orientations could be measured in each hole. Dips vary from 26° to 90° in Hole 1271A and from 38° to 85° in Hole 1271B. Figure F57 is a lower hemisphere plot showing the poles to the late alteration veins (green serpentine and composite black and green serpentine veins) and the brittle fractures and shear zones. Orientations were restored by rotation around a vertical axis such that the azimuth of the stable remnant magnetization for the piece measured points to the north. The reorientation of the veins using paleomagnetic data is discussed in "Structures in Peridotite and Gabbroic Intrusions," p. 8, in "Mantle Upwelling, Melt Transport, and Igneous Crustal Accretion" in the "Leg 209 Summary" chapter. The plot shows that the veins have approximately random orientations. These orientations may simply be a consequence of volume expansion during metamorphism. Brittle fractures also have a random orientation, suggesting a complex deformation history or that the fractures formed in response to near-hydrostatic stresses created by volume expansion during metamorphism.

Summary

Core recovered from Site 1271 records a deformation history for the peridotite and intrusive gabbroic material that follows a general downtemperature path from high-temperature crystal-plastic deformation, possibly in the presence of melt, to low-temperature brittle deformation. Spinel foliations observed in dunitic intervals may record a supersolidus deformation event that occurred during porous flow of melt and formation of dunite horizons. At least two generations of magmatic features cut Site 1271 dunites and harzburgites. The first magmatic event appears to have occurred under dominantly static conditions and produced intergranular textures that resemble those observed in laboratory experiments on olivine-melt assemblages. These are inferred to result from crystallization of plagioclase and pyroxene from melt migra-

F56. Dips of alteration veins, p. 100.
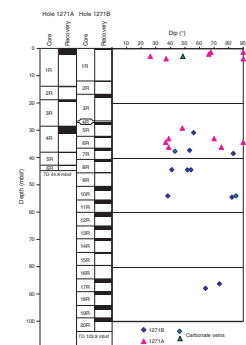
F57. Poles to alteration veins and brittle shear zones, p. 101.
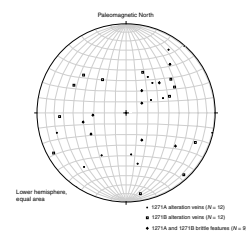
tion by porous flow along olivine grain boundaries. A later generation of magmatic veining and impregnation appears to have occurred under static conditions over some core intervals and within granulite-grade ductile shear zones over other intervals. Ductile strain is localized in peridotite only where it includes gabbroic material.

Late stages of crystal-plastic deformation occurred under hydrous, amphibolite facies conditions, during which clinopyroxene and olivine were altered to pale brown amphibole. Amphibolite alteration occurred under static conditions in some samples, where it produced random crystal arrays that partially to completely obscure granulite facies deformation fabrics. Samples in which strain was localized during late stages of crystal-plastic deformation contain schistose arrays of parallel pale brown amphibole interlayered with recrystallized olivine and/or plagioclase. In these samples, late crystal-plastic deformation occurred concurrently with semibrittle deformation in amphibole mats where strain was accommodated by cataclasis and diffusive mass transfer.

Semibrittle shear zones composed of intensely foliated colorless amphibole, serpentine, chlorite, clays, and possibly hyrogrossular cut crystal-plastic shear zones. Strain was localized into intervals of intense alteration of gabbro veins and/or host peridotite at greenschist or subgreenschist facies conditions. Core from the base of Hole 1271B contains a series of partially cohesive fault gouges. These likely formed on brittle faults late in the deformation history of Site 1271. Crosscutting relations to constrain the timing of these faults in relation to semibrittle shear zones are not present in the recovered core, but it is reasonable to assume that brittle faulting was the last deformation event.

GEOCHEMISTRY

We performed chemical analyses on eight peridotites and two gabbros from Site 1271 selected by the shipboard scientific party, using inductively coupled plasma–atomic emission spectrometry (ICP-AES) for determining major and trace element concentrations and gas chromatography for H_2O and CO_2. These 10 samples are representative of the rocks recovered from the two holes drilled at Site 1271. In Hole 1271A we sampled three dunites. In addition, from Hole 1271B we sampled two gabbros and one dunite from Unit I, one harzburgite from Unit II, and two peridotites (one harzburgite and one dunite with intergranular gabbroic material) from Unit III (see "Hole 1271B," p. 3, in "Igneous and Mantle Petrology" and "Hole 1271B," p. 12, in "Metamorphic Petrology" for the characterization of the lithologic units in Hole 1271B). Also in Unit III, Hole 1271B, one sample was taken from a thin chromite layer in order to quantify the spinel composition. However, only ~20% of the sample had dissolved after the $LiBO_4$ digestion, with most spinels remaining undissolved. Discrete amphibole and plagioclase samples were taken from a BAG from Unit III, Hole 1271B, for analysis. The results for the major and trace elements, in both serpentinized peridotites and mafic rocks and in mineral separates are reported on a volatile-free basis in Tables T4 and T5, respectively.

Serpentinized Peridotites

Bulk rock analyses of serpentinized peridotites from Site 1271 show that the composition of all of these rocks was modified to different extents by alteration, leading to the addition of variable amounts of vola-

tile constituents to the original composition. Site 1271 peridotites are characterized by high loss on ignition (LOI) values (8.6–14.9 wt%) and high H_2O contents (10.5–17.5 wt%). These high LOI values and H_2O concentrations are consistent with the visual core descriptions and X-ray diffraction results (see "Metamorphic Petrology," p. 9) that show that Site 1271 peridotites are altered predominantly to serpentine and, to a lesser extent, brucite (mainly associated with veins). Both of these minerals are characterized by high water content and LOI values (Fig. F58). We note that the highest LOI values (>14 wt%) are found in samples in which brucite was observed (see "Metamorphic Petrology," p. 9). Sample 209-1271B-12R-1, 134–139 cm, described as a dunite containing a small fraction of altered interstitial material between olivine pseudomorphs and interpreted as an impregnated dunite (see "Igneous and Mantle Petrology," p. 2), displays the lowest LOI and water content. This is consistent with the thin section description, which suggests that part of the primary mineral content, in particular olivine (~40%) and small relics of clinopyroxene, were preserved.

There are no systematic relationships between the volatiles (carbon, hydrogen, and sulfur) and other elements in the Site 1271 peridotites. Sulfur in the analyzed peridotites ranges 760–1330 ppm (Table T4). One sample (Sample 209-1271B-10R-1, 109–112 cm) shows a distinctly higher CO_2 content (1.5 wt%) compared to the other peridotites (0.11–0.30 wt%). This particular sample is crosscut by coarse-grained carbonate veins (see "Site 1271 Thin Sections"). The presence of these veins has apparently led to elevated calcium and strontium contents as well as high CO_2.

Site 1271 harzburgites contain the major element oxides SiO_2 (42.5–43.2 wt%), MgO (42.5–46.5 wt%), and Al_2O_3 (~0.4 wt%) (Fig. F58). Site 1271 dunites display wider ranges of SiO_2 (38.3–44 wt%), MgO (41.3–46.2 wt%), and Al_2O_3 (0.05–0.99 wt%) than Site 1271 harzburgites. We note that the highest MgO values for dunites (45.8–46.2 wt%) and harzburgites (46.5 wt%) correspond to Samples 209-1271A-4R-2, 32–37 cm, and 106–111 cm, and 209-1271B-17R-1, 107–109 cm, in which significant amounts of brucite, a secondary mineral with as much as 69 wt% MgO, were described (see "Metamorphic Petrology," p. 9).

Site 1271 harzburgites and dunites are depleted in Al_2O_3 (0.05–0.99 wt%) and CaO (<0.04 wt%), with the exception of Sample 209-1271B-10R-1, 109–112 cm. This sample displays significantly higher CaO content (2.1 wt%), which can be attributed to the addition of carbonates, revealed by visual core description and thin section observation (see "Metamorphic Petrology," p. 9) and by high CO_2 contents.

The most striking characteristic of Site 1271 peridotites is their high Fe_2O_3 content compared to peridotites previously analyzed during Leg 209. The Site 1271 dunites display the highest Fe_2O_3 values (11–14.15 wt%). As a result, Site 1271 dunites are characterized by low and variable Mg# (Mg/[Mg+Fe]), in the range of 85%–89%, whereas Site 1271 harzburgites display Mg#s of 90%–92%, comparable to those of massif peridotites, ophiolite mantle, and abyssal peridotites studied previously (Fig. F59). Although the bulk rock analyses of Site 1271 peridotites show that they have been modified to some extent by alteration, these low Mg#s appear to rule out MgO enrichment associated with the formation of brucite during alteration. The low Mg#s of Site 1271 dunites may therefore reflect enrichment in Fe relative to Mg before alteration. Sample 209-1271B-12R-1, 134–139 cm, interpreted as an impregnated dunite (see "Igneous and Mantle Petrology," p. 2), displays higher

F58. LOI, SiO_2, and Al_2O_2 vs. MgO, p. 102.
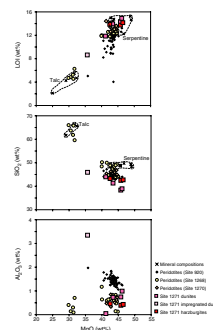
F59. FeO vs. MgO whole-rock concentrations, p. 103.
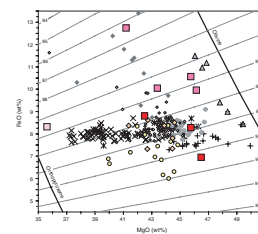
SiO_2 (45.9 wt%), Al_2O_3 (3.35 wt%), and CaO (3.5 wt%) contents and lower MgO (35.6 wt%) than other Site 1271 peridotites. These values are consistent with the presence of gabbroic material interstitial to olivine, as suggested by thin section description (see **"Igneous and Mantle Petrology,"** p. 2).

Trace element compositions of Site 1271 harzburgites, in particular Ni (2500–2950 ppm), Cr (2500–2850 ppm), and V (24.3–33 ppm), plot in the same range as peridotites previously analyzed during Leg 209 (Fig. **F60**). The Ni contents (2100–2850 ppm) of Site 1271 dunites also plot in the same range of values. Site 1271 dunites are characterized by highly variable Cr (50–9100 ppm) and, to a lesser extent, V (6–36 ppm), probably due to high and variable proportions of spinel present as euhedral grains as large as 3 mm (see **"Igneous and Mantle Petrology,"** p. 2). Spinel concentrates all of the Cr and a significant amount of V in these rocks. The presence or absence of spinel could explain the scattering in Al_2O_3 content observed in dunites, as aluminum in spinel contributes significantly to the bulk rock aluminum budget in these highly refractory peridotites.

Sample 209-1271B-12R-1, 134–139 cm, displays slightly lower Ni concentrations (1790 ppm) than the other Site 1271 peridotites. As Ni is mainly concentrated in olivine, the low Ni content in Sample 209-1271B-12R-1, 134–139 cm, coupled with its low MgO content relative to other Site 1271 dunites, results from the lower olivine proportion in this sample. The Cr content (3560 ppm) in the same sample (209-1271B-12R-1, 134–139 cm) plots in the same range as other Site 1271 dunites. The sample is enriched in V (88 ppm) compared to Site 1271 peridotites. As in the other 1271 dunites, the high Cr content is controlled by the amount of spinel sampled. However, the high V content of Sample 209-1271B-12R-1, 134–139 cm, does not correlate with its Cr content and probably results from the addition of clinopyroxene, a mineral into which V is preferentially partitioned.

With the exception of Sample 209-1271B-12R-1, 134–139 cm, Site 1271 peridotites are depleted in TiO_2 (<0.02 wt%), Y (<2 ppm), Zr (<2–5.2 ppm) and, to a lesser extent, Sc (<4–8 ppm) compared to Leg 153 peridotites. They are also depleted in Sr (<5 ppm) except for Sample 209-1271B-10R-1, 110–112 cm, which displays higher Sr content (290 ppm), as a result of the presence of carbonates that led also to high Ca and CO_2 values (see above). Site 1271 peridotites plot in the same range of Al_2O_3, TiO_2, V, and Sc concentrations as Site 1268 and 1270 peridotites (Fig. **F61**). These are moderately incompatible elements, preferentially partitioning into the liquid during partial melting. Their concentration range suggests that, like the Site 1268 and 1270 peridotites, Site 1271 peridotites underwent higher degrees of partial melting than Leg 153 peridotites.

Sample 209-1271B-12R-1, 134–139 cm, which is interpreted as an impregnated dunite (see **"Igneous and Mantle Petrology,"** p. 2), displays higher TiO_2 (0.09 wt%), Y (16 ppm), and Zr (35 ppm) than the other Site 1271 peridotites. These high values are consistent with the addition of small amounts of gabbroic material as indicated by thin section description (see **"Igneous and Mantle Petrology,"** p. 2).
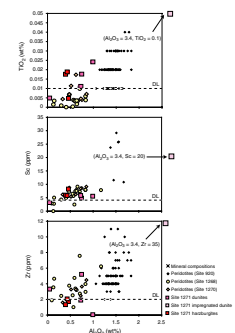
Gabbroic Rocks

We analyzed two gabbroic rocks from Site 1271, one of which was described as a BAG (see **"Igneous and Mantle Petrology,"** p. 2, for more

F60. V and Cr vs. Al_2O_3, p. 104.
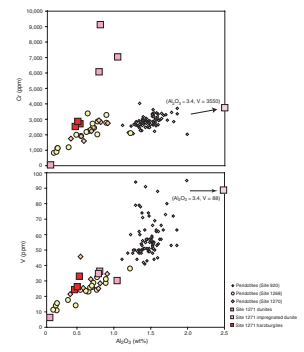
F61. TiO_2, Sc, and Zr vs. Al_2O_3, p. 105.

details). We also analyzed plagioclase and amphibole separates from one BAG from Unit III (Sample 209-1271B-11R-1, 66–67 cm). Both the gabbro and the BAG from Site 1271 have relatively low LOI values (1.8–2.5 wt%) and H_2O contents (2.3–3.5 wt%), which are similar to the gabbroic rocks analyzed from Site 1268 (Fig. F62).

Major element geochemistry of the gabbro and BAG shows that they are similar in composition for SiO_2 (~48 wt%), Al_2O_3 (~16 wt%), and CaO (~12 wt%). However, the gabbro and BAG have very different concentrations of TiO_2 and Fe_2O_3. The gabbro has a lower concentration of TiO_2 (0.77 wt%) and higher Fe_2O_3 (10 wt%), whereas the BAG has higher TiO_2 (3.3 wt%) and lower Fe_2O_3 (4.7 wt%) (Fig. F63).

Trace element geochemistry also discriminates between the gabbro and BAG. The gabbro has Cr (640 ppm), Ni (223 ppm), Sr (84 ppm), Ba (65 ppm), and low concentrations of incompatible elements. The BAG has higher Ni (598 ppm) and Ba (498 ppm) but lower Cr (69 ppm) (Fig. F64) and higher concentrations of incompatible elements such as V, Y, Zr, and Sc compared to the gabbro.

The plagioclase separate taken from a BAG (Sample 209-1271B-11R-1, 66–67 cm) was also analyzed for major and trace element geochemistry: SiO_2 (46.8 wt%), Al_2O_3 (32.8 wt%), CaO (15.5 wt%), and Na_2O (2.1 wt%). The plagioclase is close to the detection limit for most trace elements apart from Sr (687 ppm) and Ba (337 ppm). An anorthite content of 81 mol% was calculated for the plagioclase. The amphibole sample, taken from the same interval as the plagioclase, has also undergone some alteration to chlorite (see "Site 1271 Thin Sections"). The amphibole contains SiO_2 (51.5 wt%), TiO_2 (1.6 wt%), Al_2O_3 (5.5 wt%), MgO (19.9 wt%), and CaO (12.6 wt%). This composition represents a mixture of tremolite/actinolite, pargasite, and hastingite end-members, with tremolite/actinolite composing about two-thirds of the solid solution. Apart from Sr, Y, and Zr, the amphibole contains high concentrations of trace elements, for example, Ni (887 ppm), V (588 ppm), and Sc (135 ppm). This may be because the trace element composition of the sample represents the original clinopyroxene and not the secondary amphibole. Unfortunately, the plagioclase and amphibole separates that were analyzed are >28 m away from the whole-rock BAG sample and are from a separate igneous unit. Because the original mineral compositions have been altered and the mineral separates were taken at a distance from the whole-rock sample, it is not certain that the whole-rock composition should correspond to a mixture of the analyzed plagioclase and amphibole. However, the BAG sample does appear to lie along a simple mixing line between the plagioclase and amphibole compositions for most elements, apart from Fe_2O_3, Cr, and TiO_2 (Figs. F63, F64). The differences are probably due to the presence of minor amounts of rutile and/or olivine in the BAG whole-rock sample, as seen in "Site 1271 Thin Sections" and reported in "Igneous and Mantle Petrology," p. 2.

When compared to gabbros recovered from previous drill sites, the gabbro from Site 1271 lies within the major element range of Al_2O_3, TiO_2, and Fe_2O_3 observed for the Site 1270 microgabbros. This is also true for the moderately incompatible trace elements V and Sc. The Site 1270 microgabbros and the Site 1271 gabbro are, in general, more enriched than the Site 1268 gabbros but less enriched than the Site 1270 oxide gabbros for those elements that are concentrated in the oxide phases (e.g., TiO_2, V, and Fe_2O_3). The BAG also falls in the range of the Site 1270 microgabbros for most other elements, apart from Cr, Fe_2O_3,
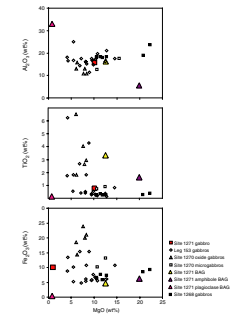
F62. H_2O vs. SiO_2 in gabbros, p. 106.
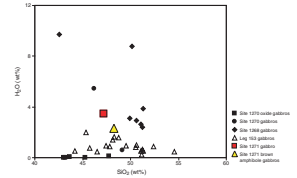
F63. V, Sc, and Cr vs. Al_2O_3 in gabbros, p. 107.
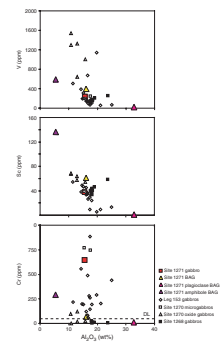
F64. Al_2O_3, TiO_2, and Fe_2O_3 vs. MgO in gabbros, p. 108.

and TiO$_2$. The BAG is enriched in TiO$_2$ and depleted in Cr and Fe$_2$O$_3$ compared to the Site 1271 gabbro and the Site 1270 microgabbros; indeed, it is more depleted in Fe$_2$O$_3$ than the Site 1268 gabbros and has a comparably low Cr content. At Site 1268, low Cr contents in gabbros were interpreted to indicate that the original gabbronorite protolith was more evolved than the Leg 153 gabbros.

Discussion

The composition of serpentinized peridotite and gabbroic rocks from Site 1271 was modified to some extent by alteration, leading to the addition of significant amounts of volatile constituents to the original composition and the modification of the protolith Ca and Sr content in at least one of the studied peridotites.

Compared to Site 1270 peridotites, Site 1271 peridotites display a wider range of compositions for major elements. This reflects mainly the variability of lithology sampled at Site 1271. The bulk rock composition of Site 1271 harzburgites is similar to that of Site 1270 peridotites for major and trace elements. Site 1271 dunites are distinguished from Site 1271 harzburgites and Site 1270 peridotites by Fe enrichment (Mg# = 86–89), which is interpreted as a primary feature. However, Site 1271 dunites have Ni contents in the same range as Site 1271 harzburgites and Site 1270 and 1268 peridotites. Ni partitions preferentially into olivine. As a result, fractional crystallization of olivine leads to low and variable Ni contents in olivine cumulates. Therefore, the high Ni content of Site 1271 dunites precludes a cumulate origin for these rocks despite their low Mg#. Like Site 1271 dunites, abyssal peridotites sampled at fast-spreading ridges (e.g., Niu and Hekinian, 1997) and peridotites from the mantle transition zone in ophiolites (e.g., Godard et al., 2000; Korenaga and Kelemen, 1997; Koga et al., 2001) display low Mg# and often have impregnation textures. Such impregnated dunites are thought to be the product of porous melt flow involving high melt fluxes at near-solidus conditions. In these rocks, relatively low Mg# compared to residual peridotites does not indicate a cumulate origin, but instead it is evidence for widespread melt-rock reactions between peridotite and olivine-saturated basaltic melt at shallow levels (e.g., Niu and Hekinian, 1997). These melt-rock reactions involve Fe-Mg exchange and, potentially, pyroxene dissolution and olivine precipitation (e.g., Kelemen, 1990) at high melt/rock ratios. We suggest that a similar process accounts for Site 1271 dunite composition.

As with other gabbros recovered during Leg 209, the major and trace element composition of these rocks is consistent with their primary mineralogical constitution as described in thin section descriptions. The low Cr contents of the BAG (<100 ppm), comparable to the Cr concentration in Site 1268 gabbros, indicates that the initial BAG was more evolved than the other Site 1271 gabbros. The amphibole analysis from the BAG has a major element composition close to 28 mol% pargasite and 72 mol% tremolite/actinolite with minor hastingite. Its low Al$_2$O$_3$ content suggests that it crystallized at relatively low temperature, suggesting a low-temperature igneous or high-temperature metamorphic origin (replacement of the initial gabbroic mineralogy). However, the trace element concentrations in the amphibole point reflect to an original clinopyroxene composition (e.g., high V and Sc).

PHYSICAL PROPERTIES

The physical properties of the peridotites and gabbros cored in Holes 1271A and 1271B were characterized through a series of measurements on whole-core sections, split-core pieces, and discrete samples as described in "Physical Properties," p. 18, in the "Explanatory Notes" chapter. We measured natural gamma ray (NGR) activity and magnetic susceptibility on the multisensor track (MST) system and thermal conductivity, compressional wave velocity, density, and porosity. The rock names reported in data tables correspond to the primary lithologies determined by the igneous core description group.

Natural Gamma Radiation

All cores recovered during Leg 209 were measured using NGR logger on the MST at intervals of 10 cm with a time period of 30 s. Results are output in counts per second. The cores from Holes 1271A and 1271B display natural radioactivity in the same range as the background radiation in the core laboratory on board the *JOIDES Resolution*. No significant peak was recorded in the NGR data in these cores.

Magnetic Susceptibility

Magnetic susceptibility values were acquired on the MST at 2.5-cm intervals for all recovered cores. Most cores from Site 1271 have high magnetic susceptibility (Fig. F65), which is related to the presence of magnetite in the serpentinized peridotites. The magnetic susceptibilities of the peridotites at Site 1271 are comparable to those at Site 1270 (see Fig. F105, p. 159, in the "Site 1270" chapter) and the peridotites from Hess Deep (Gillis, Mével, Allan, et al., 1993) and the Kane Fracture Zone (MARK) area (Cannat, Karson, Miller, et al., 1995) (see Fig. F88, p. 145, in the "Site 1268" chapter).

Thermal Conductivity

Thermal conductivity measurements were made at irregularly spaced intervals along cores from Holes 1271A and 1271D in six peridotite samples and one troctolite. The data are summarized in Table T6. The thermal conductivities of the peridotite samples range 2.5–3.2 W/(m·K) (mean = 2.87 W/[m·K]); the thermal conductivity of the troctolite ranges 2.88–2.93 W/(m·K). These values are comparable to the thermal conductivities of peridotite from ODP sites at Hess Deep (Gillis, Mével, Allan, et al., 1993) and MARK (Cannat, Karson, Miller, et al., 1995) and to the values measured at Sites 1268 and 1270 (Fig. F66).

As described in "Thermal Conductivity," p. 19, in "Physical Properties" in the "Explanatory Notes" chapter, measurements were taken in three directions on the cut face of the archive halves, whenever possible. The purpose of these measurements is to determine the degree of apparent anisotropy. The apparent thermal conductivity anisotropy of peridotites and the troctolite measured in cores from Site 1271 ranges 0.6%–5.5%. Apparent thermal conductivity anisotropies measured since the beginning of Leg 209 (including Sites 1268, 1270, and 1271) are compiled in Figure F67. Anisotropy ranges 0.2%–12.6% (mean = 4.63%) in gabbros, peridotites, and troctolites.

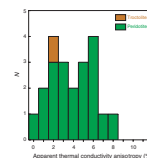F65. MST magnetic susceptibility, p. 109.
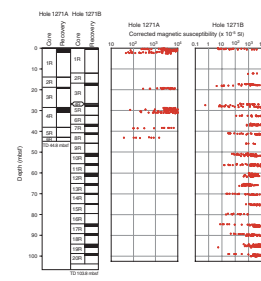
T6. Thermal conductivities, p. 124.

F66. Thermal conductivity, p. 110.
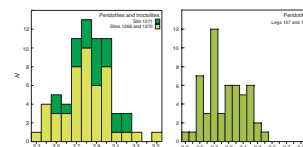
F67. Apparent thermal conductivity anisotropy, p. 111.

Porosity, Density, and Seismic Velocity

Bulk density, grain density, and porosity were measured on small sample chips (~3–6 cm³) from Holes 1271A and 1271D. *P*-wave velocity and wet bulk density were measured on cube samples, as described in "*P*-Wave Velocity," p. 20, and "Porosity and Density," p. 20, in "Physical Properties" in the "Explanatory Notes" chapter). These data are summarized in Table T7. With the exception of one troctolite, all of the samples are serpentinized peridotites.

The density and velocity data are compared with data from Legs 147 and 153, as well as Sites 1268 and 1270 (see "Porosity, Density, and Seismic Velocity," p. 38, in "Physical Properties" in the "Site 1268" chapter and "Porosity, Density, and Seismic Velocity," p. 41, in "Physical Properties" in the "Site 1270" chapter) in Figure F68. Velocity anisotropy in the serpentinized peridotite samples from Site 1271, which ranges from 2.4% to >8.1%, is comparable to the anisotropy in samples from Site 1268 and 1270. The lone troctolite sample is essentially isotropic. Velocities and densities in the peridotite and troctolite samples from Site 1271 are also comparable to the densities and velocities of the ultramafic samples from Sites 1268 and 1270 and are notably lower than the velocities and densities of samples from Legs 147 (Gillis, Mével, Allan, et al., 1993) and 153 (Cannat, Karson, Miller, et al., 1995) (Fig. F68). The velocity and density of the troctolite sample are comparable to the properties of gabbros from Leg 153.

PALEOMAGNETISM

Paleomagnetic measurements for Site 1271 were possible only on a small number of samples as a consequence of the low core recovery in both Holes 1271A (recovery = 12.9%) and 1271B (recovery = 15.3%). Remanence data were obtained from a total of 15 discrete samples and 47 archive-half pieces of altered peridotites (Tables T8, T9).

Continuous Measurements

Remanence measurements were made for archive-half pieces where the vertical orientation was unambiguous and the piece length was greater than ~8 cm. Data were obtained from the centers of core pieces, treating pieces <8 cm and intervals within 4 cm of piece ends as voids. This minimum length is still smaller than the overall width of the magnetometer response functions (~8 cm width at half height), and so some artifacts are inevitable. In addition, where only a small number of suitable pieces were present in a section, these pieces were measured alone to minimize any interfering signal from adjacent pieces with differing magnetization orientations. The archive-half data are thus far from ideal, but these data nonetheless provide some indication of the stable remanence directions and intensities at the site.

The overall low recovery from Holes 1271A and 1271B makes identification of downhole trends in the archive-half data difficult. For example, Hole 1271A yielded oriented pieces of sufficient length for continuous measurements only from Cores 209-1271A-1R and 4R. Natural remanent magnetization (NRM) intensities for both Holes 1271A and 1271B were generally between 1 and 10 A/m and were measurable in the 2G magnetometer at the slowest track speed. Intensities from Section 209-1271A-1R-1 were >10 A/m, resulting in residual counts (>1000)
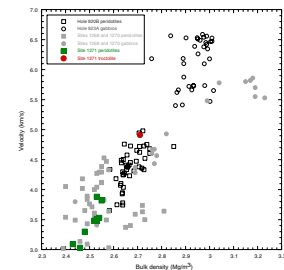
on the z-SQUID (superconducting quantum interference device) axis. Much lower intensities (3×10^{-4} to 5×10^{-4} A/m) were measured for two pieces (Sections 209-1271B-14R-1 [Piece 4] and 17R-1 [Piece 2]) of BAG (see "Igneous and Mantle Petrology," p. 2, for a discussion of the occurrence and significance of this rock type in the cores).

The remanence prior to demagnetization is commonly dominated by a substantial low-stability overprint (Fig. F69B, F69D, F69E). This steep, presumably drilling-related overprint was removed at peak demagnetizing fields of 20–30 mT. In a small number of core pieces, notably in the gabbro-impregnated peridotites from Cores 209-1271B-10R and 12R (Fig. F70D, F70E), the low-stability overprint constitutes a relatively minor portion of the remanence. After removal of this low-stability component, a variable percentage of remanence (1.5%–30% of the NRM) remained. Characteristic remanent magnetization (ChRM) directions were calculated by principal component analysis (Kirschvink, 1980) from the archive-half data over the demagnetization interval of 20 to 40–50 mT without anchoring the vectors to the origin. On average, the ChRM represents ~8% of the NRM (Table T9).
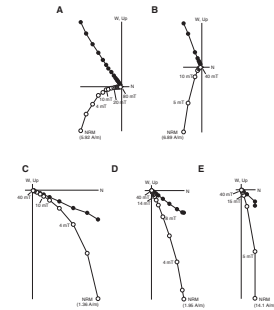
Discrete Samples

Nine samples from Hole 1271A and six samples from Hole 1271B were subjected to stepwise alternating-field (AF) demagnetization (Table T8). Five of the samples from Hole 1271A were quarter-round samples ($25–50$ cm^3). These were demagnetized using the in-line demagnetizer and measured in a single position with the 2G magnetometer. The remaining samples (cubes with a nominal volume of ~9 cm^3) were demagnetized using the off-line DTech demagnetizer and measured in three positions at each step (see "Paleomagnetism," p. 22, in the "Explanatory Notes" chapter).

The NRM intensities for these discrete samples (3.4–19.5 A/m) (Table T8) corroborate the values obtained from the continuous measurements. In contrast to the pass-through measurements, complete removal of the low-stability overprint was generally achieved at AF peak fields of ~15 mT (Figs. F69A, F69C, F69D, F70A–F70C). Linear trends directed toward the origin were obtained from 20 to 50 mT, and a characteristic remanent direction was calculated by principal component analysis (Kirschvink, 1980). As observed from previous sites, low median destructive fields (MDFs) ranging 3–12 mT (Fig. F71) are the consequence of the low-field isothermal remanence induced during drilling. The highest MDF value occurs in a troctolite (Sample 209-1271B-12R-1, 131–133 cm).

Remanence Directions

Comparison of stable remanence directions obtained from discrete samples and archive halves from the same interval shows generally good agreement. The low-stability overprint is more pronounced in the archive-half data (Fig. F70), but a similar final direction (average difference = 17° ± 7.4° for 15 data pairs) is commonly isolated in both types of data. A small number of intervals show angular discrepancies near 30°. Figure F69C–F69E illustrates a progression from a shallow ChRM direction in a standard-sized (~9 cm^3) discrete sample to a somewhat steeper direction in a larger quarter-round sample and the steepest direction in the corresponding archive-half data. These data might be interpreted as reflecting a more pronounced drilling-related overprint in
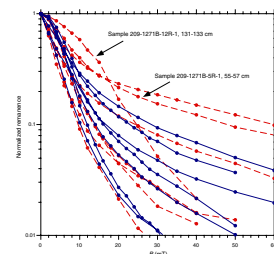
F69. Demagnetization of discrete and long-core samples, Hole 1271A, p. 113.

F70. Demagnetization of discrete and long-core samples, Hole 1271B, p. 114.
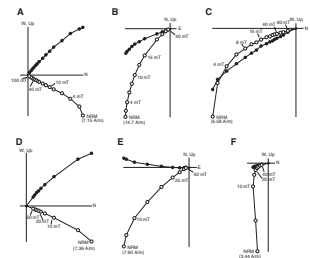
F71. Normalized magnetization decay curves of discrete samples, p. 115.

the exterior of the core. However, we find no systematic bias toward steeper inclinations in the archive halves relative to the discrete samples for the overall data set from Site 1271. The mean inclination discrepancy for the 15 data pairs is 5° ± 15°, with the discrete samples sometimes having the steeper inclinations (cf. Tables T8, T9). Despite these differences, the overall correspondence between the discrete and archive-half data is good.

Both archive halves and discrete samples yield exclusively positive inclinations suggestive of normal polarity (Fig. F72). A single archive half (Section 209-1271B-12R-1 [Piece 8]) with a negative inclination was later shown to be inverted prior to labeling (Table T9). The mean inclination for discrete samples from Site 1271 is 25.3° (+10.6°/–13.2°; κ = 10.3; N = 15; using the inclination-only method of McFadden and Reid, 1982). The mean inclination for archive halves is 29.0° (+3.4°/–4.6°; κ = 25; N = 46) and is not significantly different from the average discrete sample inclination. Neither value for mean inclination is significantly different from the reference geomagnetic dipole inclination (28°), and therefore no block rotation is required since the magnetization of the rocks was acquired.

## Anisotropy of Magnetic Susceptibility

Anisotropy of the magnetic susceptibility (AMS) was measured on all 10 cube samples. The degree of anisotropy (P = maximum/minimum eigenvalues) ranges 1.06–1.33 (Table T10). All samples are statistically triaxial (i.e., all three eigenvalues are distinct), but most have magnetic fabrics that tend toward oblate shapes. Although there is significant scatter, the minimum eigenvectors for these oblate fabrics include a weak cluster in the northeast and southwest quadrants that may indicate a preferred subvertical foliation oriented northwest–southeast (Fig. F73). Three samples have more pronounced lineations (ratio of maximum/intermediate eigenvalues is larger than the ratio of intermediate/minimum eigenvalues). The AMS fabrics reflect the preferred orientation or distribution of elongate magnetite grains or grain clusters (possibly along serpentinite veins) and thus may provide an estimate of the dominant orientation of magnetite-bearing veins.

MICROBIOLOGY

At Site 1271, one rock interval, Sample 209-1271B-7R-1 (Piece 6, 32–48 cm), was collected to characterize the microbial community inhabiting this environment. The rock sample is a completely serpentinized dunite.

The sample was prepared as described in "Igneous Rocks," p. 24, in "Microbiology" in the "Explanatory Notes" chapter. The type and extent of contamination caused by drill fluids was evaluated as described in "Contamination Tests," p. 26, in "Microbiology" in the "Explanatory Notes" chapter. The results for the perfluorocarbon tracer (PFT) showed that the PFT reached the exterior of the core and may have penetrated to the interior of the microbiology sample (Table T11; Fig. F74). A sample from Section 209-1271A-7R-1 (Piece 6) was rinsed in nanopure water, and the collected water (38 mL) was filtered and examined under a fluorescence microscope. Microsphere concentration was 9.43 × 10^5 microspheres/mL of wash. A 0.5-g interior piece of the sample was examined under a fluorescence microscope to detect microsphere pene-

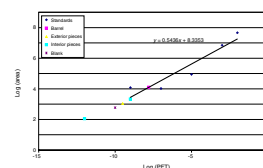F72. Paleomagnetic inclinations and declinations, p. 116.
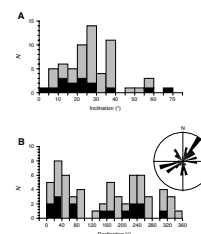
T10. AMS data, p. 128.
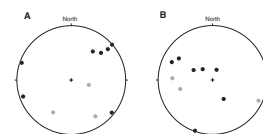
F73. Projections of minimum and maximum eigenvectors, p. 117.

T11. PFT in standards and core pieces, p. 129.

F74. PFT in standards and core pieces, p. 118.

tration. The results showed that the microspheres did not penetrate to the interior of the sample.

Aliquots of surface water were collected and prepared for deoxyribonucleic acid (DNA) analysis as described in **"Seawater and Water Samples,"** p. 26, in "Microbiology" in the "Explanatory Notes" chapter.

A mud sample was collected from Hole 1271A for microbial analysis. The sample was from sediment entrained in the core barrel during a push-in test to determine sediment thickness. Microscopic observation showed that the sample was reddish brown and composed of nannofossils and fine inorganic particles. Since no mudline was established, no curation sample designation was assigned other than hole number. A total of 20 g of mud and 10 mL of sterile artificial seawater (ASW) was placed in a sterile 50-mL tube for analysis. The sample was then mixed by shaking until the sediment was dispersed in the fluid. Direct counts and cultures of the samples were prepared as described in **"Direct Counts and Enrichment Cultures,"** p. 26, in "Sediments" in "Microbiology" in the "Explanatory Notes" chapter. Results of direct count assay were 1.89×10^6 bacteria/mL and 8.49×10^6 viruses/mL. A 10-µL aliquot from the sample (no clearing allowed) was added to 900 µL of ASW and filtered through a 45-µm nitrocellulose membrane filter and placed on a nutrient agar plate. Growth (colonies were too numerous to count) was noted on the filter surface and on particulates at the filter surface after 24 hr of incubation at room temperature (~23.0°C). Both the direct count data and the culture data indicate that bacteria were in interstitial spaces and attached to sediment particles. The remaining sample was stored at –70°C for shore-based DNA analysis of the microbial community.

DOWNHOLE MEASUREMENTS

Before the last core in Hole 1271B was retrieved, we decided not to displace the hole with sepiolite (as routine prior to logging) because of concerns with hole stability. The core recovery had been low throughout the coring operations (recovery = ~19.7%), and most of the recovered cores were fragmented pieces suggesting potential unstable hole conditions. Our thought was that displacing the volume of the hole with mud might fracture the formation and loosen more rock fragments that could potentially cause a risk to the logging tool strings. The operational strategy was to acquire logging data as quickly as possible to minimize any risks to the tools, starting with the triple combination (triple combo) geophysical tool string and followed by the Formation MicroScanner-sonic tool string.

Drilling operations reached a total depth of 104.5 mbsf, and the mechanical bit release was used to leave the rotary core barrel bit at the bottom of the hole. Shortly after releasing the bit, high torque, loss of circulation, and drag conditions were experienced while placing the BHA at logging depth. Ultimately, the BHA was placed at a logging depth of 3627 meters below rig floor, or 31 mbsf.

After the triple combo was rigged up, a conflict between the telemetry cartridge, the Accelerator Porosity Sonde (APS), and the Dual Induction–Phasor Resistivity Tool (DIT-E) was encountered. The telemetry cartridge was displaying a low voltage signal and both the APS and the DIT-E were displaying conflicting signals. Exchanging telemetry cartridges resolved the conflict.

Sea conditions were calm with ~1-m heave while the triple combo tool string was being deployed. During deployment of the first tool string, an obstruction was encountered at a logging depth of 35 mbsf, or 4 m below the end of the BHA. Three unsuccessful attempts were made to get past this obstruction by raising and lowering the tool string. In order to test the possibility that the bit had not released (since the distance to the apparent obstruction was so small), the tool string was raised until it was inside the pipe and the drill string was raised ~10 m. On lowering the tool string, the same total wireline length was deployed before the tool reached the obstruction, indicating the tool was several meters beyond the end of the pipe; thus, the bit must have been released. After three more attempts to pass the obstruction, logging operations were terminated. The wireline logging operations took ~7.5 hr from rig-up to rig-down.

REFERENCES

Agar, S.M., Casey, J.F., and Kempton, P.D., 1997. Textural, geochemical, and isotopic variations in gabbroic shear zones from the MARK area. *In* Karson, J.A., Cannat, M., Miller, D.J., and Elthon, D. (Eds.), *Proc. ODP, Sci. Results,* 153: College Station, TX (Ocean Drilling Program), 99–121.

Allen, D.E., and Seyfried, W.E., Jr., 2003. Compositional controls on vent fluids from ultramafic-hosted hydrothermal systems at mid-ocean ridges: an experimental study at 400°C, 500 bars. *Geochim. Cosmochim. Acta,* 67:1531–1542.

Arai, S., and Abe, N., 1995. Reaction of orthopyroxene in peridotite xenoliths with alkali-basalt melt and its implication for genesis of alpine-type chromitite. *Am. Mineral.,* 80:1041–1047.

Arai, S., and Matsukage, J.H., 1996. Petrology of gabbro-troctolite-peridotite complex from Hess Deep, equatorial Pacific: implications for mantle-melt interaction within the oceanic lithosphere. *In* Mével, C., Gillis, K.M., Allan, J.F., and Meyer, P.S. (Eds.), *Proc. ODP, Sci. Results,* 147: College Station, TX (Ocean Drilling Program), 135–155.

Arai, S., and Yurimoto, H., 1994. Podiform chromitites of the Tari-Misaka ultramafic complex, southwestern Japan, as mantle-melt interaction products. *Econ. Geol.,* 89:1277–1286.

Aumento, F., and Loubat, H., 1971. The Mid-Atlantic Ridge near 45°N. XVI. Serpentinized ultramafic intrusions. *Can. J. Earth Sci.,* 8:631–663.

Bodinier, J.-L., 1988. Geochemistry and petrogenesis of the Lanzo peridotite body, Western Alps., *Tectonophysics,* 149:67–88.

Boudier, F., and Nicolas, A., 1995. Nature of the Moho Transition Zone in the Oman Ophiolite. *J. Petrol.,* 36:777–796.

Cannat, M., Karson, J.A., Miller, D.J., et al., 1995. *Proc. ODP, Init. Repts.,* 153: College Station, TX (Ocean Drilling Program).

Casey, J.F., 1997. Comparison of major- and trace-element geochemistry of abyssal peridotites and mafic plutonic rocks with basalts from the MARK region of the Mid-Atlantic Ridge. *In* Karson, J.A., Cannat, M., Miller, D.J., and Elthon, D. (Eds.), *Proc. ODP, Sci. Results,* 153: College Station, TX (Ocean Drilling Program), 181–241.

Charlou, J.-L., Donval, J.-P., Fouquet, Y., Jean-Baptiste, P., and Holm, N., 2002. Geochemistry of high H_2 and CH_4 vent fluids issuing from ultramafic rocks at the Rainbow hydrothermal field (36°14′N, MAR). *Chem. Geol.,* 19:345–359.

Deer, W.A., Howie, R.A., and Zussman, J., 1992. *An Introduction to the Rock-Forming Minerals* (2nd ed.): Harlow, United Kingdom (Longman Scientific Technical).

Dilek, Y., Coulton, A., and Hurst, S.D., 1997. Serpentinization and hydrothermal veining in peridotites at Site 920 in the MARK area. *In* Karson, J.A., Cannat, M., Miller, D.J., and Elthon, D. (Eds.), *Proc. ODP, Sci. Results,* 153: College Station, TX (Ocean Drilling Program), 35–59.

Faul, U.H., 2000. Constraints on melt distribution in anisotropic polycrystalline aggregates undergoing grain growth. *In* Bagdassarov, N., Laporte, D., and Thompson, A.B. (Eds.), *Physics and Chemistry of Partially Molten Rocks:* Dordrecht (Kluwer Acad. Publ.), 67–92.

Fujiwara, T., Lin, J., Matsumoto, T., Kelemen, P.B., Tucholke, B.E., and Casey, J., 2003. Crustal evolution of the Mid-Atlantic Ridge near the Fifteen-Twenty Fracture Zone in the last 5 Ma. *Geochem., Geophys., Geosyst.,* 4:10.1029/2002GC000364.

Gillis, K., Mével, C., Allan, J., et al., 1993. *Proc. ODP, Init. Repts.,* 147: College Station, TX (Ocean Drilling Program).

Godard, M., Jousselin, D., and Bodinier, J.-L., 2000. Relationships between geochemistry and structure beneath a paleo-spreading centre: a study of the mantle section in the Oman ophiolite. *Earth Planet. Sci. Lett.,* 180:133–148.

Hebert, R., Adamson, A.C., and Komor, S.C., 1990. Metamorphic petrology of ODP Leg 109, Hole 670A serpentinized peridotites: serpentinization processes at slow

spreading ridge environment. *In* Detrick, R., Honnorez, J., Bryan, W.B., and Juteau, T., et al., *Proc. ODP, Sci. Results,* 106/109: College Station, TX (Ocean Drilling Program), 103–115.

Hemley, J.J., Montoya, J.W., Shaw, D.R., and Luce, R.W., 1977. Mineral equilibria in the $MgO-SiO_2-H_2O$ system-II. Talc-antigorite-forsterite-anthophyllite-enstatite stability relations and some geological applications. *Am. J. Sci.,* 277:353–382.

Hostetler, P.B., Coleman, R.G., Mumpton, F.A., and Evans, B.W., 1966. Brucite in alpine serpentinites. *Am. Mineral.,* 51:75–98.

Irvine, T.N., 1977. Origin of chromitite layers in the Muskox Intrusion and other stratiform intrusions: a new interpretation. *Geology,* 5:273–277.

Iturrino, G.J., Miller, D.J., and Christensen, N.I., 1996. Velocity behavior of lower crustal and upper mantle rocks from a fast-spreading ridge at Hess Deep. *In* Mével, C., Gillis, K.M., Allan, J.F., and Meyer, P.S. (Eds.), *Proc. ODP, Sci. Results,* 147: College Station, TX (Ocean Drilling Program), 417–440.

Janecky, D.R., and Seyfried, W.E., Jr., 1986. Hydrothermal serpentinization of peridotite within the oceanic crust: experimental investigations of mineralogy and major element chemistry. *Geochim. Cosmochim. Acta,* 50:1357–1378.

Johnson, J.W., Oelkers, E.H., and Helgeson, H.C., 1992. SUPCRT92: a software package for calculating the standard molal thermodynamic properties of minerals, gases, aqueous species, and reactions from 1 to 5000 bar and 0 to 1000°C. *Comput. Geosci.,* 18:899–947.

Kelemen, P.B., 1990. Reaction between ultramafic rock and fractionating basaltic magma, I. Phase relations, the origin of calc-alkaline magma series, and the formation of discordant dunite. *J. Petrol.,* 31:51–98.

Kelemen, P.B., and Dick, H.J.B., 1995. Focused melt flow and localized deformation in the upper mantle: juxtaposition of replacive dunite and ductile shear zones in the Josephine peridotite, SW Oregon. *J. Geophys. Res.,* 100:423–438.

Kelley, D.S., Karson, J.A., Blackman, D.K., Früh-Green, G.L., Butterfield, D.A., Lilley, M.D., Olson, E.J., Schrenk, M.O., Roe, K.K., Lebon, G.T., Rivizzigno, P., and Shipboard Party, 2001. An off-axis hydrothermal vent field near the Mid-Atlantic Ridge at 30°N. *Nature,* 412:123–128.

Kirschvink, J.L., 1980. The least-squares line and plane and the analysis of palaeomagnetic data. *Geophys. J. R. Astron. Soc.,* 62:699–718.

Koga, K.T., Kelemen, P.B., and Shimizu, N., 2001. Petrogenesis of the crust-mantle transition zone and the origin of lower crustal wehrlite in the Oman ophiolite. *Geochem., Geophys., Geosyst.,* 2:10.1029/2000GC000132.

Korenaga, J., and Kelemen, P.B., 1997. Origin of gabbro sills in the Moho transition zone of the Oman ophiolite: implications for magma transport in the oceanic lower crust. *J. Geophys. Res.,* 102:27729–27749.

Martin, B., and Fyfe, W.S., 1970. Some experimental and theoretical observations on the kinetics of hydration reactions with particular reference to serpentinization. *Chem. Geol.,* 6:185–202

Matveev, S., and Ballhaus, C., 2002. Role of water in the origin of podiform chromitite deposits. *Earth Planet. Sci. Lett.,* 203:235–243.

McFadden, P.L., and Reid, A.B., 1982. Analysis of paleomagnetic inclination data. *Geophys. J. R. Astron. Soc.,* 69:307–319.

Miller, D.J., and Christensen, N.I., 1997. Seismic velocities of lower crustal and upper mantle rocks from the slow-spreading Mid-Atlantic Ridge, south of the Kane Fracture Transform Zone (MARK). *In* Karson, J.A., Cannat, M., Miller, D.J., and Elthon, D. (Eds.), *Proc. ODP, Sci. Results,* 153: College Station, TX (Ocean Drilling Program), 437–454.

Nesbitt, H.W., and Bricker, O.P., 1978. Low temperature alteration processes affecting ultramafic bodies. *Geochim. Cosmochim. Acta,* 42:403–409.

Nicolas, A., 1989. *Structure of Ophiolites and Dynamics of the Oceanic Lithosphere:* Dordrecht (Kluwer).

Niu, Y., and Hekinian, R., 1997. Basaltic liquids and harzburgitic residues in the Garrett Transform; a case study at fast-spreading ridges. *Earth Planet. Sci. Lett.,* 146:243–258.

O'Hanley, D.S., 1996. Serpentinites: records of tectonic and petrological history. *Oxford Monogr. Geol. Geophys.,* Vol. 34.

Parkinson, I.J., and Pearce, J.A., 1998. Peridotites from the Izu-Bonin-Mariana forearc (ODP Leg 125); evidence for partial melting and melt-mantle interactions in a supra-subduction zone setting. *J. Petrol.,* 39:1577–1618.

Ramp, L., 1961. Chromite in southwestern Oregon. *Bull.—Oreg. Dep. Geol. Miner. Ind.,* 52:1–169.

Rampone, E., Hofmann, A.W., Piccardo, G.B., Vannucci, R., Bottazzi, P., and Ottolini, L., 1996. Trace element and isotope geochemistry of depleted peridotites from an N-MORB type ophiolite (Internal Liguride, N. Italy). *Contrib. Mineral. Petrol.,* 123:61–76.

Seyfried, W.E., and Dibble, W.E.J., 1980. Seawater-peridotite interaction at 300°C and 500 bars: implications for the origin of oceanic serpentinites. *Geochim. Cosmochim. Acta,* 44:309–321.

Snow, J.E., and Dick, H.J.B., 1995. Pervasive magnesium loss by marine weathering of perdotite. *Geochim. Cosmochim. Acta,* 59:4219–4235.

Zhou, M.-F., Robinson, P.T., and Bai, W.-J., 1994. Formation of podiform chromitites by melt/rock interaction in the upper mantle. *Miner. Deposita,* 29:98–101.

Figure F1. Bathymetric map indicating subsea camera survey tracks and hole locations. Bathymetric data courtesy of T. Fujiwara and T. Matsumoto of JAMSTEC (Fujiwara et al., 2003).
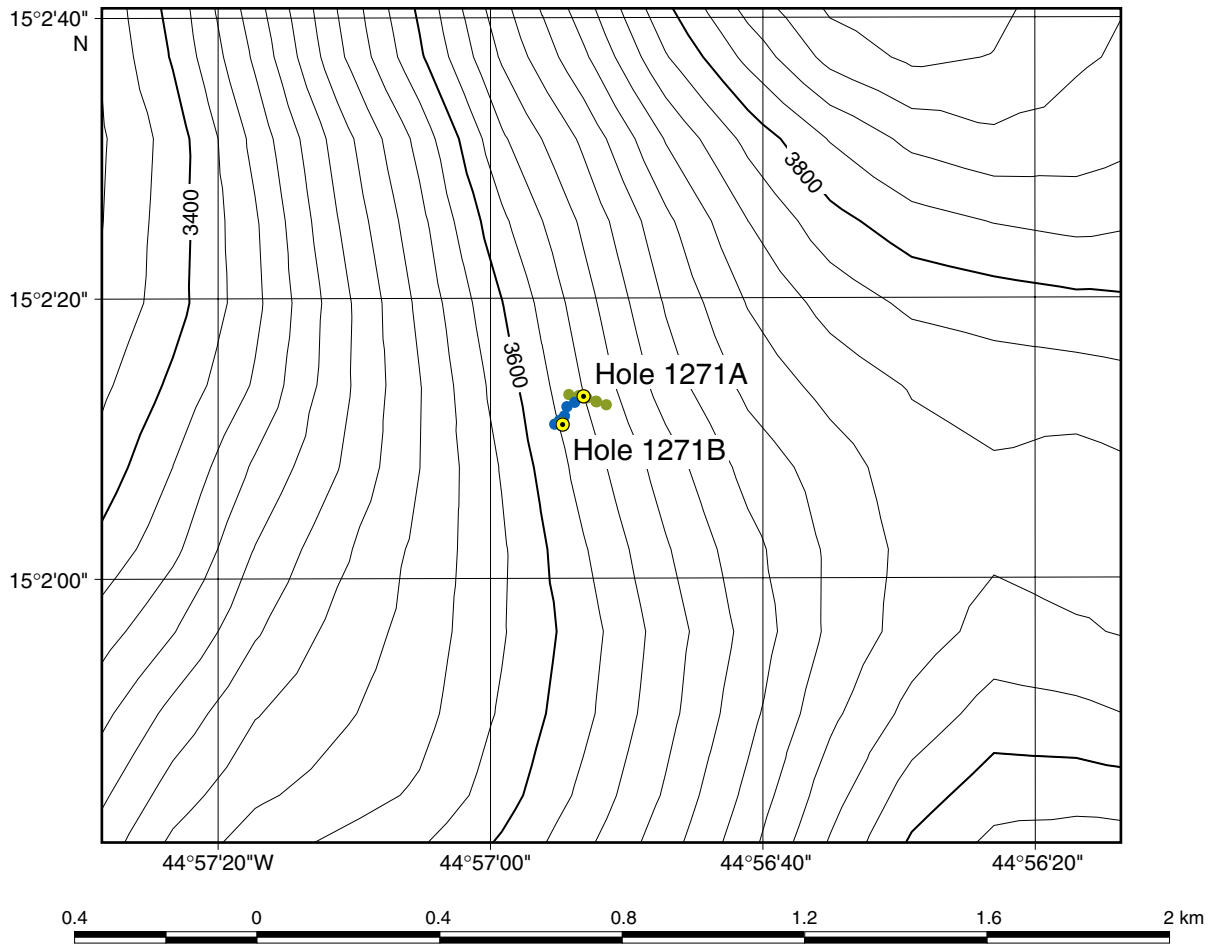
Figure F2. A. Location map with track of *Faranaut* Dive 7, locations and lithologies of samples from that dive, and the approximate positions of Holes 1271A and 1271B. (Continued on next page.)
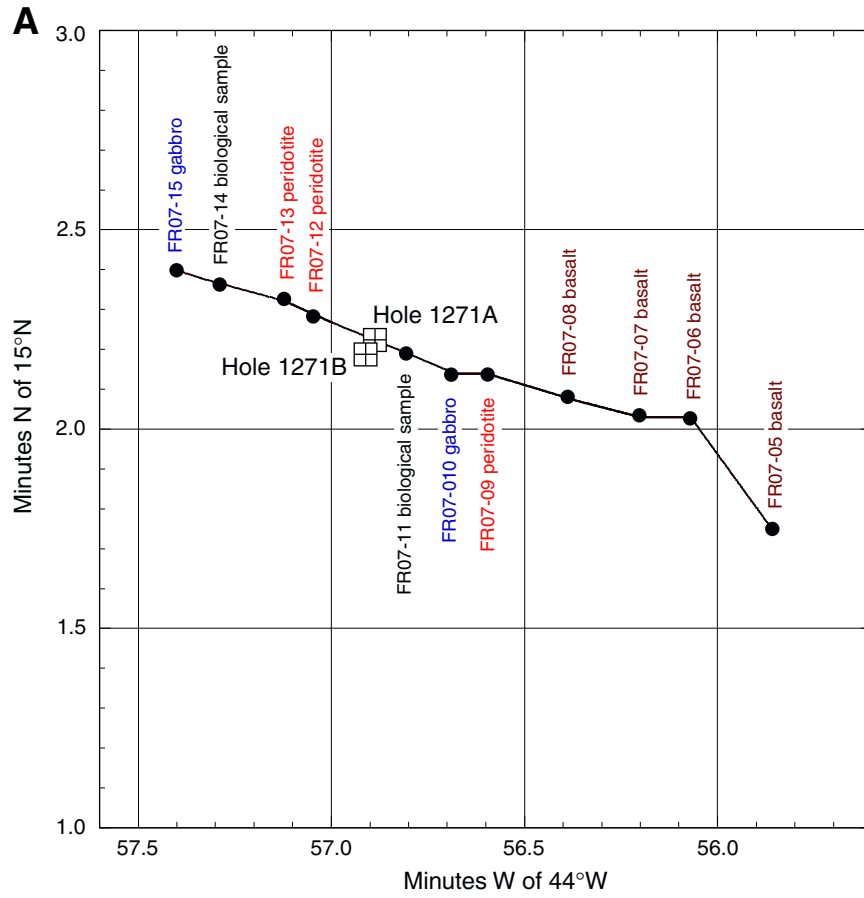
Figure F2 (continued). B. Bathymetric section based on *Faranaut* Dive 7, projected along 280° with no vertical exaggeration. Locations and lithologies of samples collected during the dive, as well as the approximate positions of Holes 1271A and 1271B are indicated.
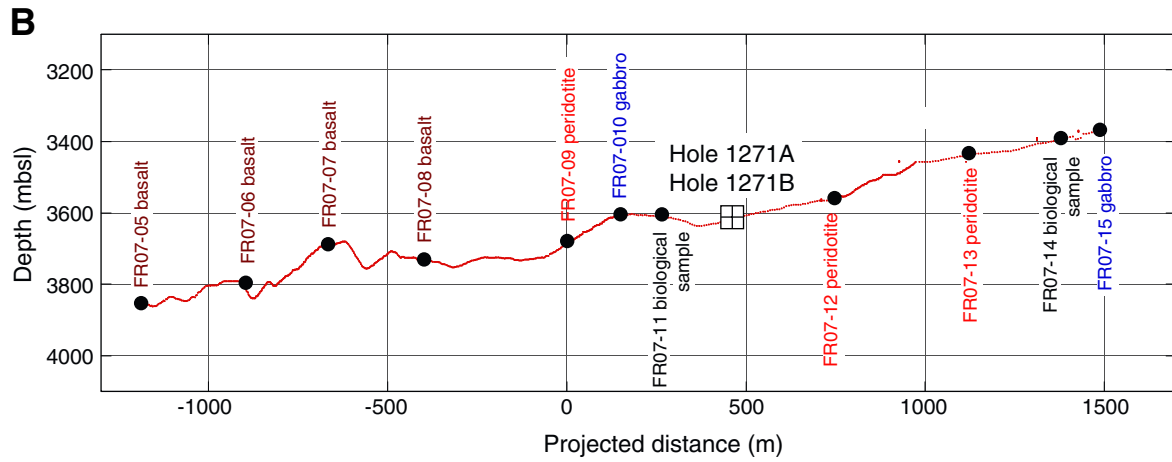
Figure F3. Hole 1271A lithology and stratigraphy. Lithologies include very highly to completely altered dunite, one rounded harzburgite sample, and a few rounded samples of microgabbro and breccia. Hole 1271A consists mainly of dunite. TD = total depth.
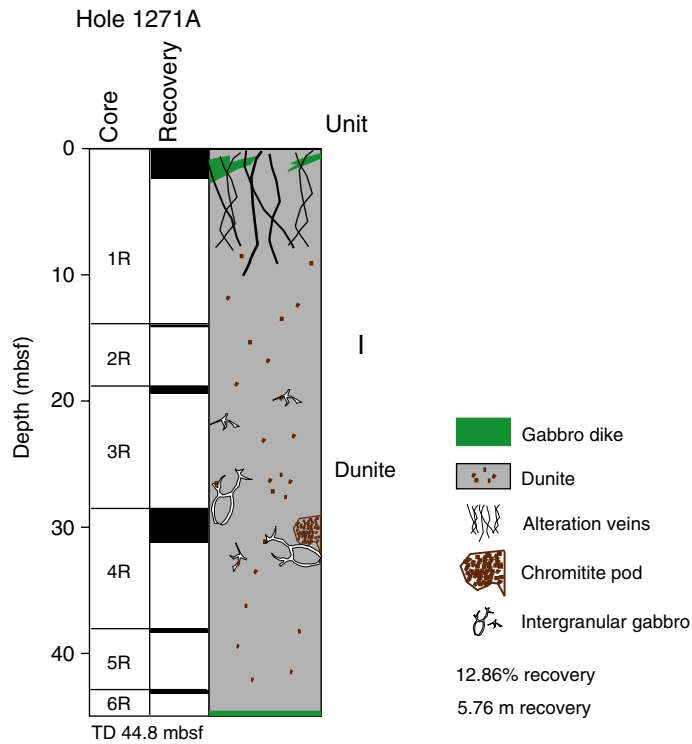
Figure F4. Close-up photograph of completely altered dunite cut by numerous alteration veins (interval 209-1271A-1R-1, 68–83 cm).
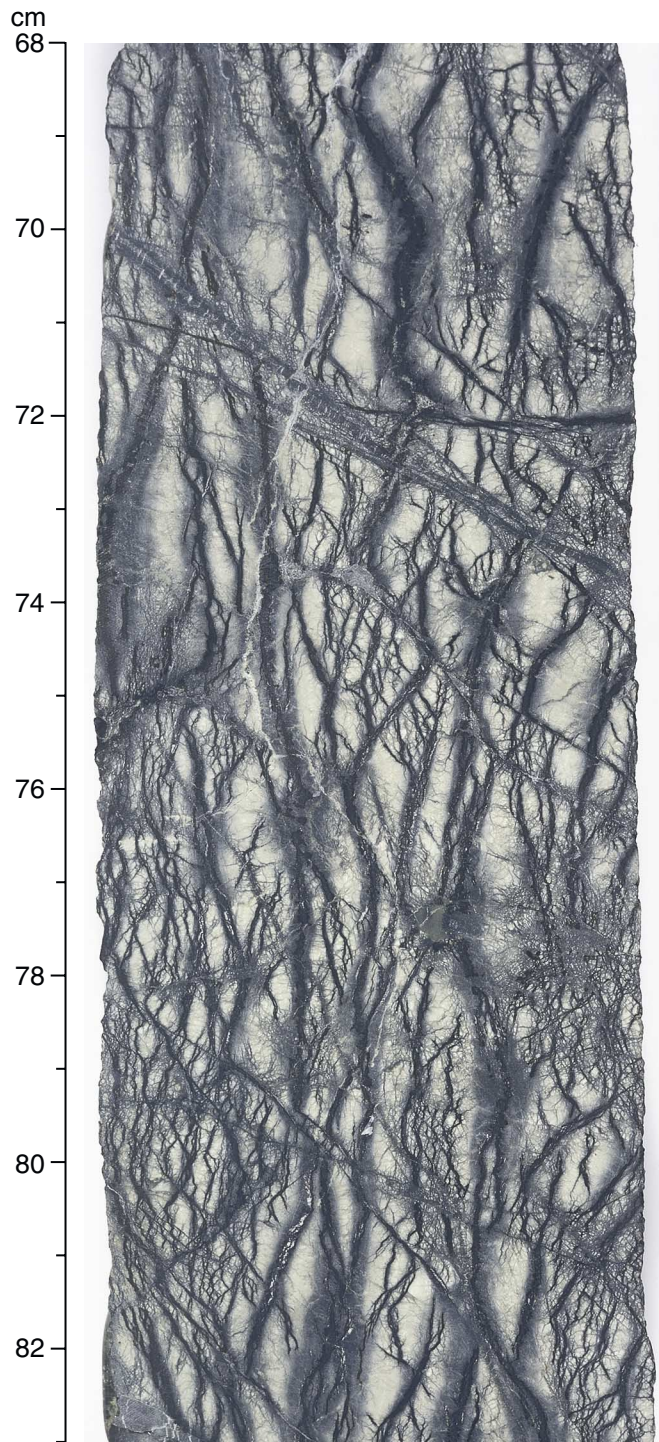
Figure F5. Photomicrograph showing orthopyroxene pseudomorph in dunite (Sample **209-1271A-1R-1, 42–45 cm**) (plane-polarized light: blue + light gray filters; field of view = 11 mm; image 1271A_009).
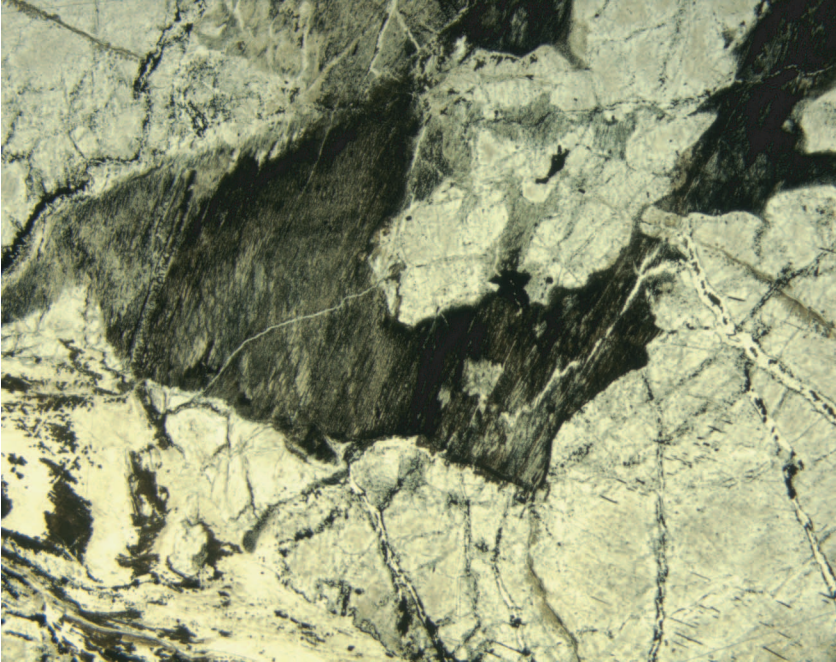
Figure F6. Photomicrograph showing a patch of plagioclase (now altered to low-temperature phases) and orthopyroxene pseudomorph in dunite (Sample **209-1271A-1R-1, 42–45 cm**) (plane-polarized light: blue + light gray filters; field of view = 11 mm; image 1271A_010).
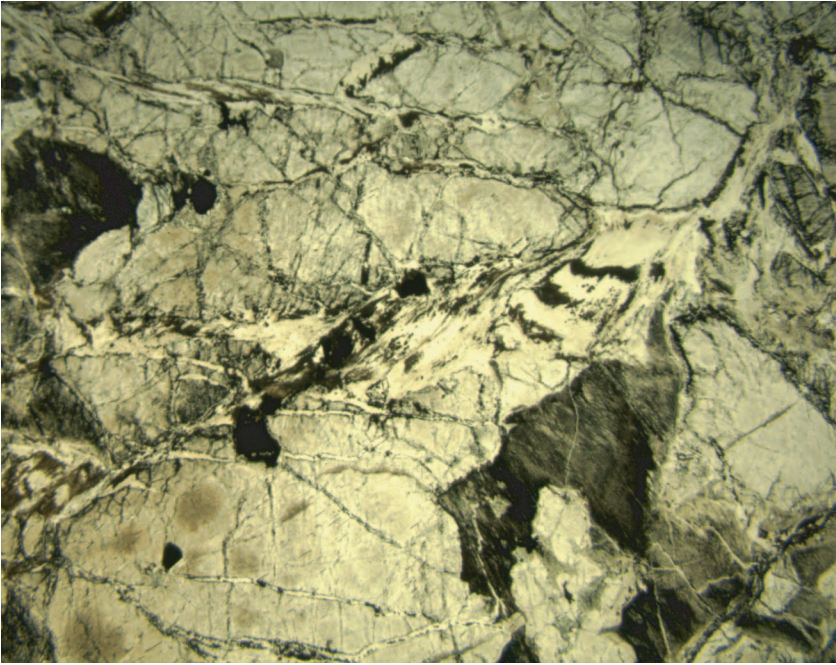
Figure F7. Photomicrograph showing olivine grains included in amphibolite (Sample **209-1271A-1R-1, 42–45 cm**) (plane-polarized light blue + light gray filters; field of view = 11 mm; image 1271A_006).
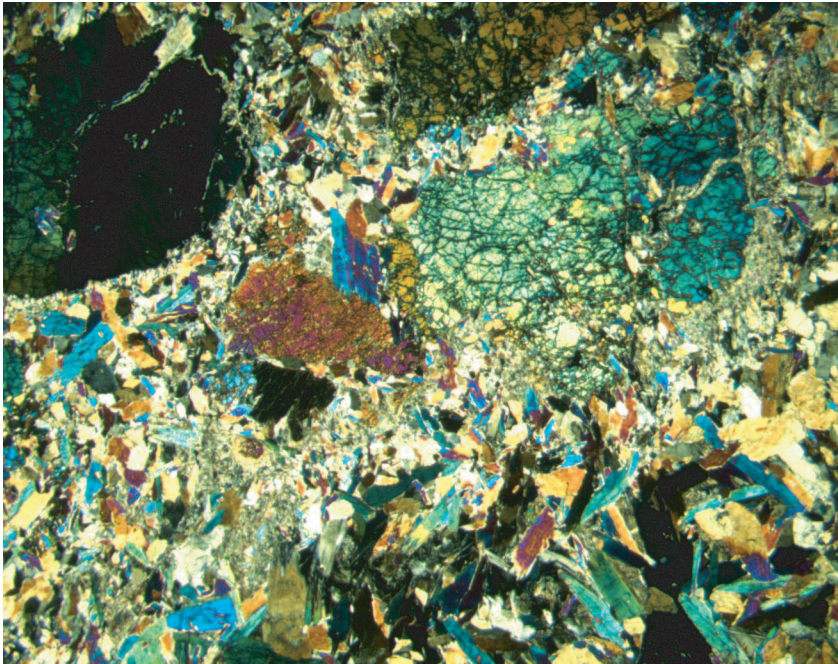
Figure F8. Photomicrograph showing coarse olivine grain separated in two parts in amphibolite (Sample 209-1271A-1R-1, 42–45 cm) (plane-polarized light: blue + light gray filters; field of view = 1.4 mm; image 1271A-007).
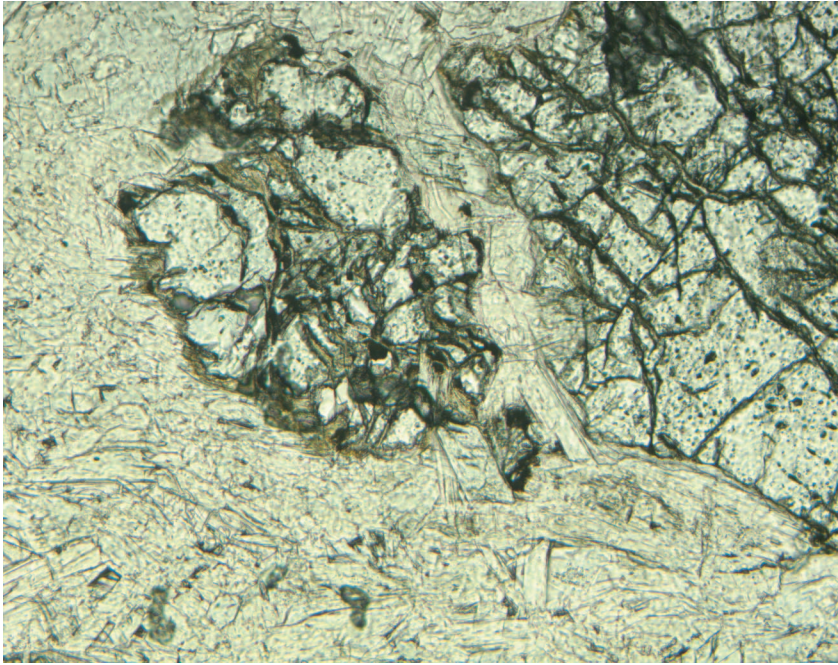
Figure F9. Close-up photograph of gabbroic material (white) along olivine grain boundaries (interval 209-1271A-4R-1 [Piece 13, 78–87 cm].

Figure F10. Close-up photograph of chromitite pod in dunite. The matrix surrounding chromite in the chromitite pod consists of chlorite (possibly replacing plagioclase) and amphibole. The host dunite intruded by the chromitite is also rich in chromian spinel (interval 209-1271A-4R-2 [Piece 2, 38–48 cm]).
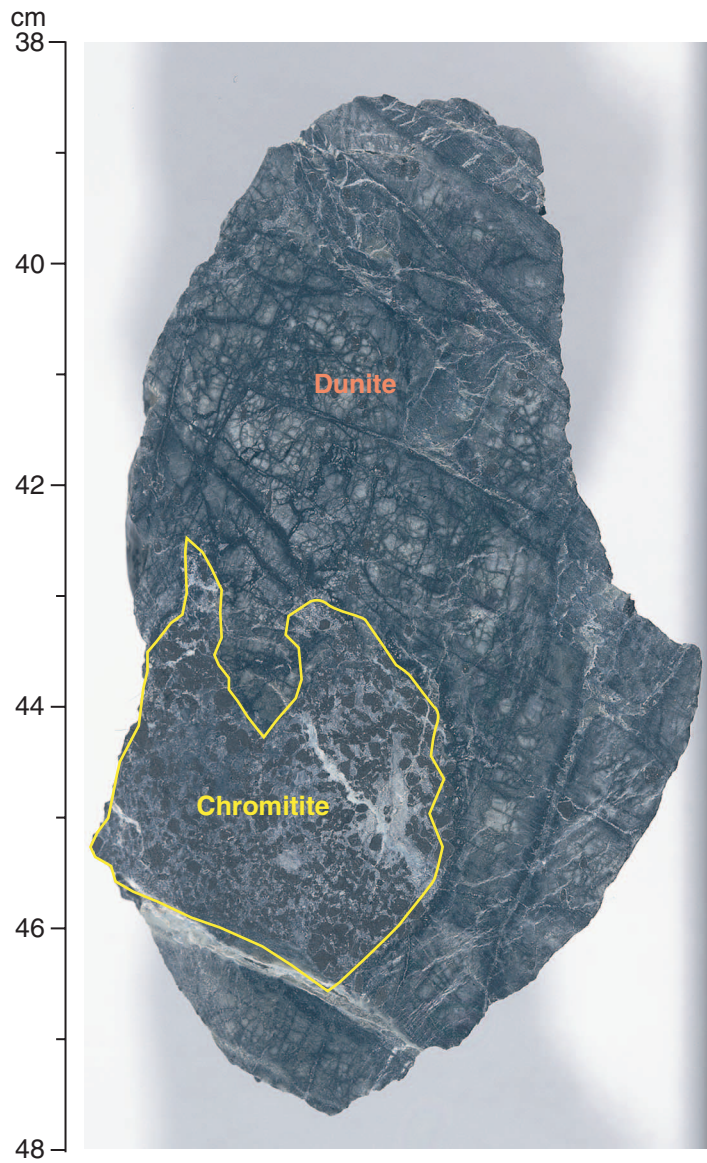
Figure F11. Photomicrograph showing rutile within chromitite (Sample **209-1271A-4R-2, 48 cm**) (cross-polarized light: no filter; field of view = 350 µm; image 1271A_017).
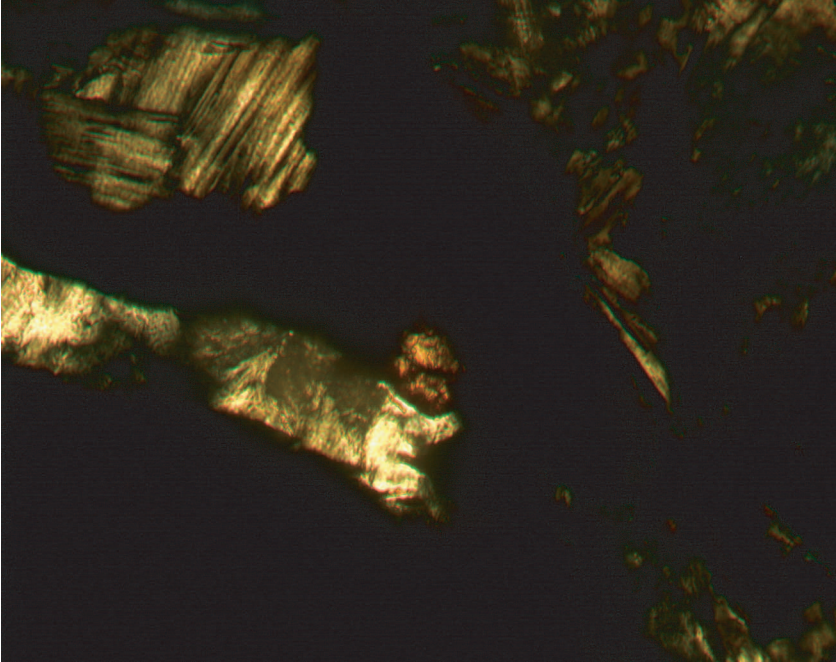
Figure F12. Photomicrograph showing reddish black chromitite, but altered grains and altered parts of grains are completely opaque. There are, or were, many inclusions of various sizes in chromite grains (Sample 209-1271A-4R-2 [Piece 2, 38–48 cm]) (plane-polarized light: blue + light gray filters; field of view = 11 mm; image 1271A_011).
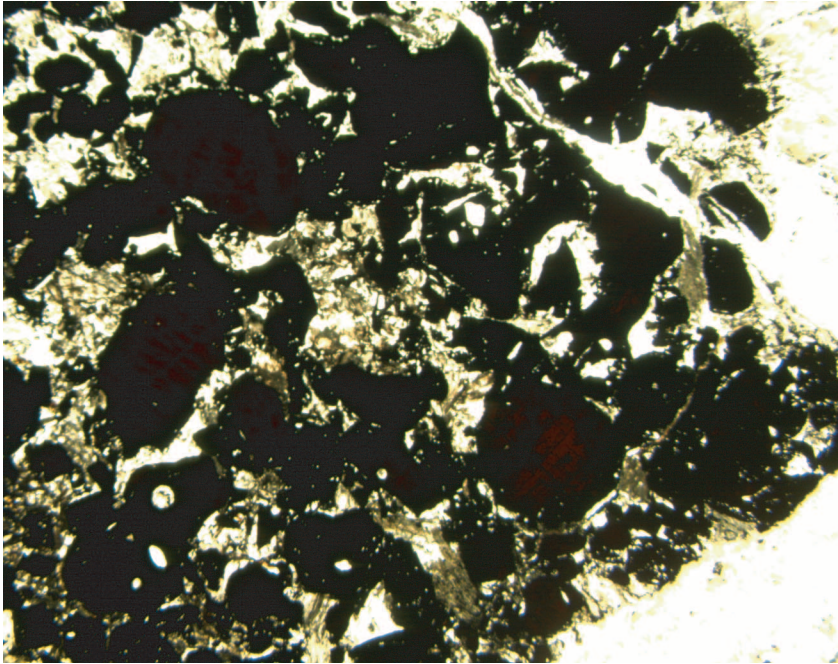
Figure F13. Hole 1271B lithology and stratigraphy. Also shown is the percentage of gabbroic material "impregnated" into the peridotites (averaged for each cored interval). TD = total depth.
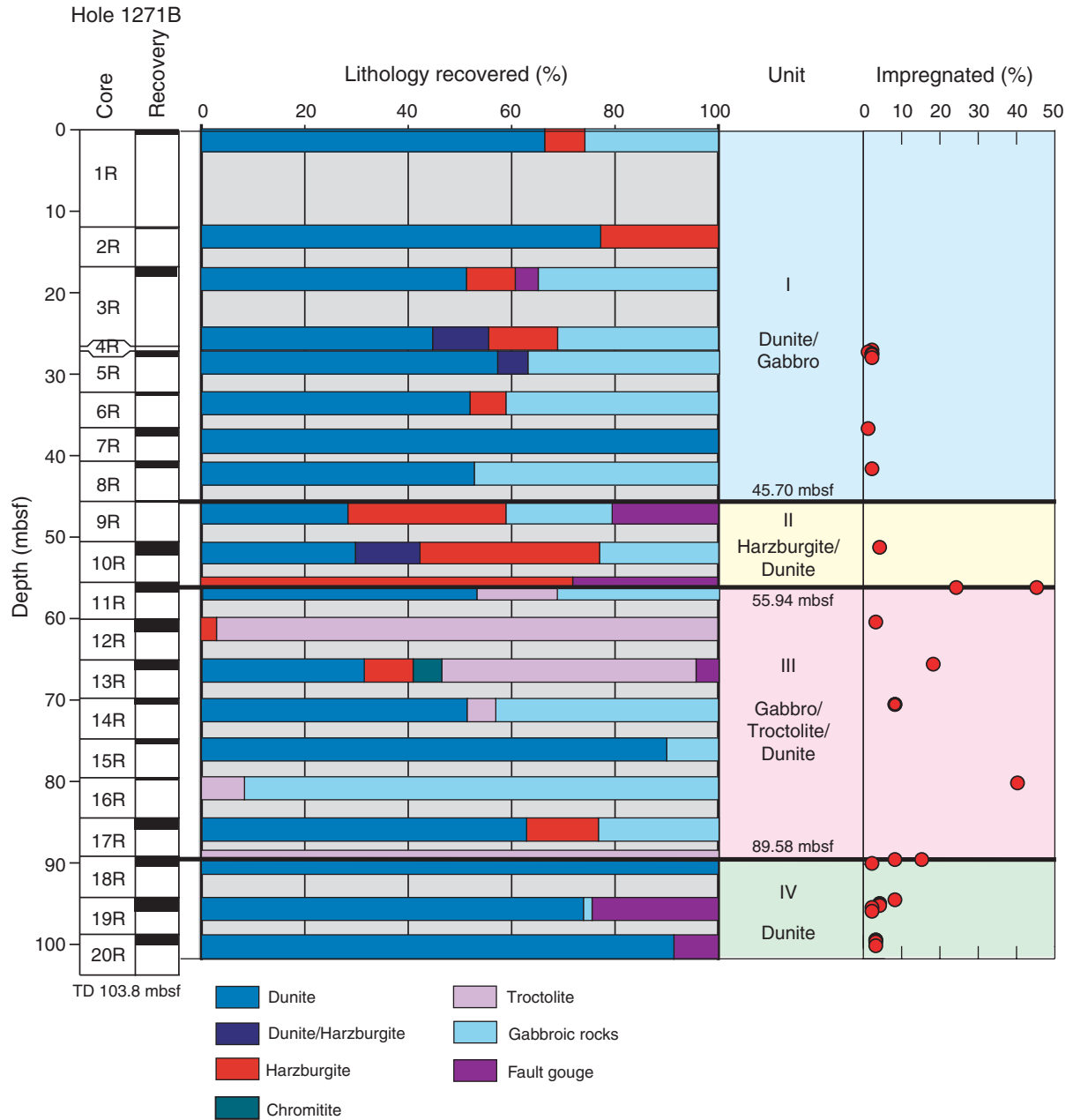
Figure F14. Gabbroic material in peridotites. **A.** Serpentinized dunite with intergranular gabbroic material now consisting of amphibole along grain boundaries and filling microcracks crosscutting olivine (interval 209-1271B-10R-1, 40–47 cm). **B.** Olivine gabbro with coarse oikocrystic texture enclosing schlieren of dunite and olivine xenocrysts (interval 209-1271B-18R-1, 20–26 cm). **C.** Troctolite enclosing dunite xenoliths and olivine xenocrysts (interval 209-1271B-16R-1, 24–30 cm). **D.** Serpentinized dunite with intergranular gabbroic minerals, mostly plagioclase with minor clinopyroxene, and crosscut by dikelets of gabbroic material (interval 209-1271B-19R-2, 1–12 cm).
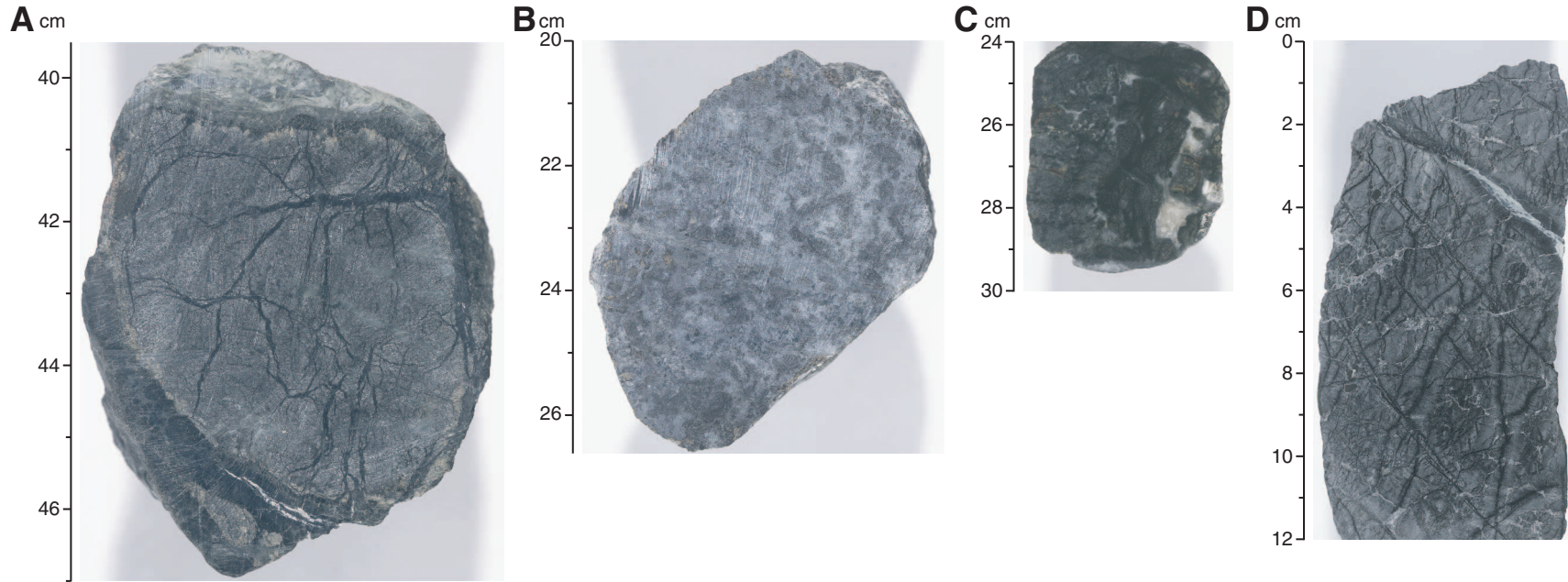
Figure F15. Photomicrographs showing reaction rims around olivine and spinel at a contact between dunite and gabbro. **A, B.** Symplectic intergrowths of spinel and alteration phases (possibly replacing plagioclase) around a spinel grain (Sample **209-1271B-7R-1, 26–29 cm**) (plane-polarized light [PPL]: blue filter); (A) field of view [FOV] = 2.75 mm; image 1271B_033; (B) close up of symplectic intergrowth (FOV = 1.4 mm; image 1271B_034). **C, D.** Symplectic intergrowths of spinel, olivine, and an alteration phase at a contact between olivine and an alteration phase similar to the one forming the intergrowth (Sample **209-1271B-10R-1, 40–43 cm**) (FOV = 0.7 mm); (C) PPL: blue + light gray + dark gray filters; image 1271B_022; (D) cross-polarized light [XPL]: blue filter; image 1271B_023. **E, F.** Symplectic intergrowths of spinel, olivine, and an alteration phase at an olivine/altered gabbro contact (Sample **209-1271B-10R-1, 40–43 cm**) (FOV = 1.4 mm); (E) PPL: blue + light gray filters; image 1271B_015; (F) XPL: dark gray filter; image 1271B_016.
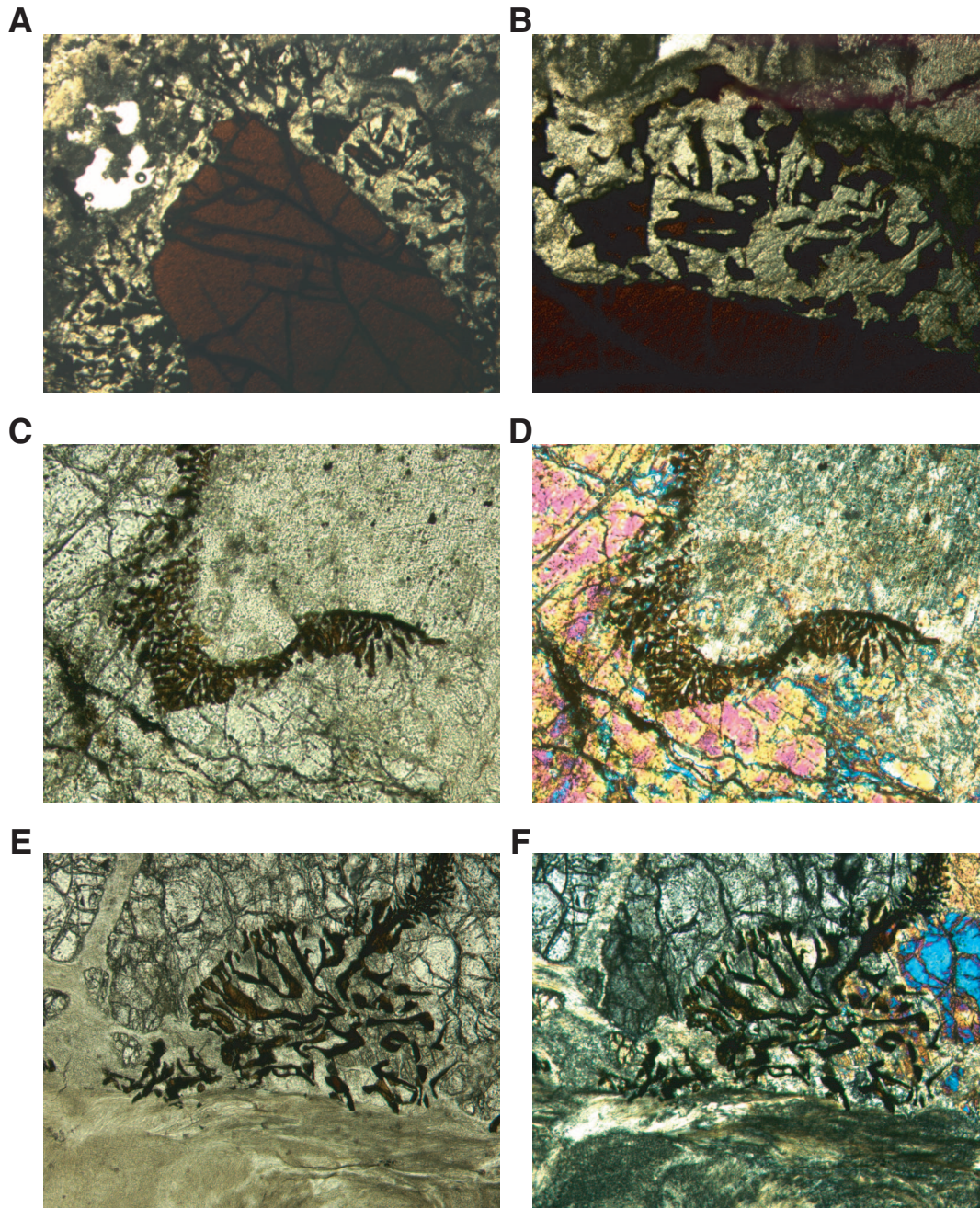
Figure F16. A, B. Photomicrographs showing an alteration phase and spinel enclosed within olivine (Sample 209-1271B-11R-1, 88–91 cm); (A) plane-polarized light: blue + dark gray filters; field of view [FOV] = 0.7 mm; image 1271B_013; (B) cross-polarized light [XPL]: blue + light gray filters; FOV = 0.7 mm; image 1271B_014. **C, D.** Coarse olivine grains in amphibolite (Sample 209-1271B-13R-1, 20–24 cm) (XPL: blue + light gray filters); (C) FOV = 2.75 mm; image 1271B_100; (D) Close-up view of C; euhedral amphibole enclosed within olivine (FOV = 0.7 mm; image 1271B_099).
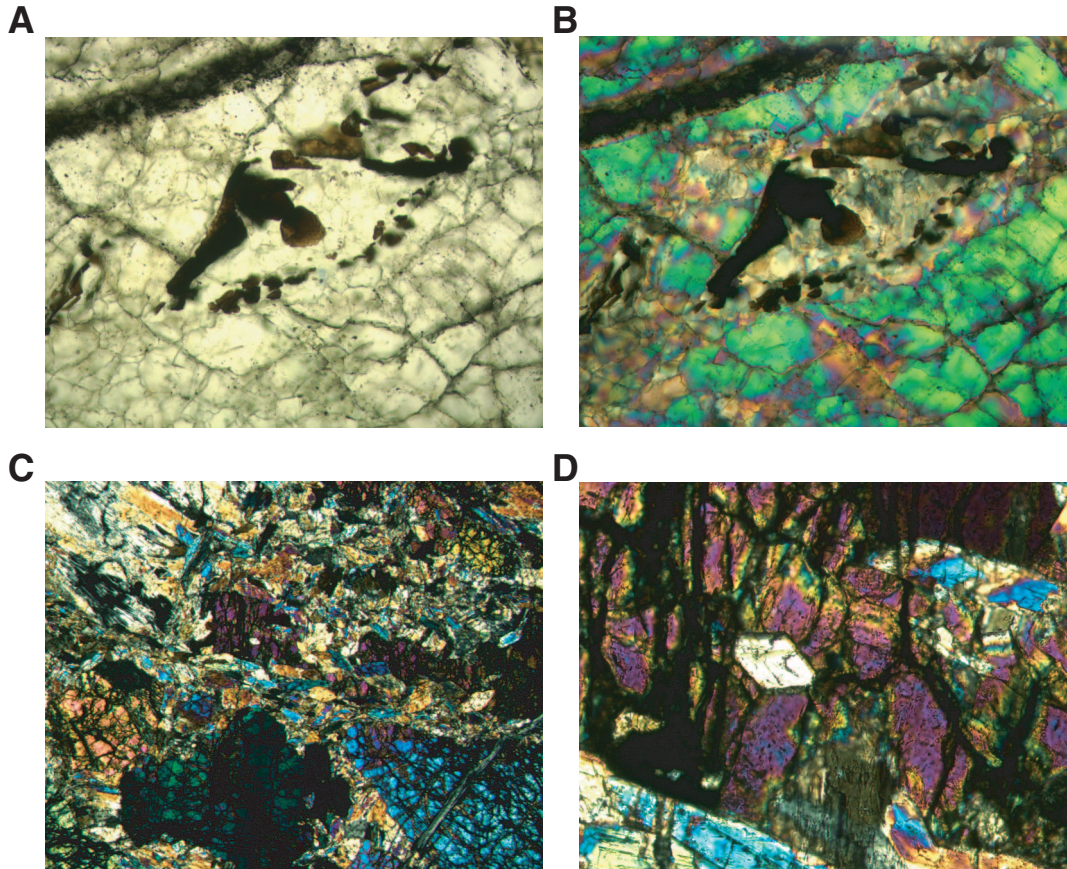
Figure F17. Photomicrographs showing incipient fragmentation of an olivine grain in dunite. The former gabbroic intrusion is now replaced by amphiboles. **A.** Sample **209-1271B-18R-1, 114–117 cm;** cross-polarized light [XPL]: blue filter; field of view [FOV] = 5.5 mm; image 1271B_082. **B–D.** Sample **209-1271B-12R-2, 16–19 cm;** (B) XPL: blue + light gray filters; FOV = 2.75 mm; image 1271_B_045; (C) XPL: blue + light gray filters; FOV = 2.75 mm; image 1271B_086; (D) XPL: blue filter; FOV = 5.5 mm; image 1271B_069.
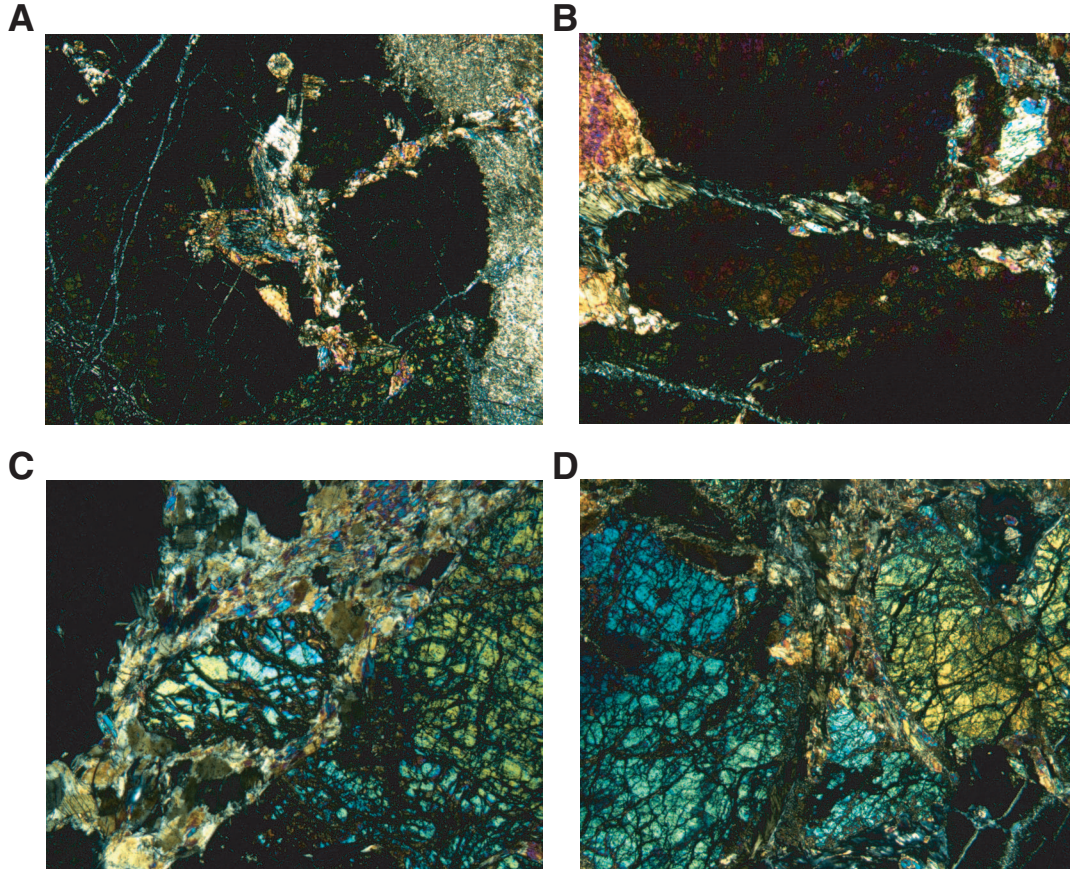
Figure F18. A–D. Photomicrographs showing olivine gabbro in which olivine and plagioclase are in textural equilibrium (Sample **209-1271B-18R-1, 20–23 cm**) (cross-polarized light: blue filter). (A) Olivine, plagioclase, and clinopyroxene assemblage (field of view [FOV] = 5.5 mm; image 1271BB_068). (B) Grains of olivine included in partially altered plagioclase (FOV = 5.5 mm; image 1271B_067). (C) Grains of olivine included in poikilitic clinopyroxene (FOV = 5.5 mm; image 1271B_040). (D) Close-up of image C showing plagioclase laths and olivine (FOV = 1.4 mm; image 1271B_041). **E, F.** Photomicrographs showing troctolite in which olivine and plagioclase are separated by amphibole (Sample **209-1271B-16R-1, 24–27 cm**) (plane-polarized light: blue + light gray filters). (E) Olivine grains within amphibole assemblages. Clusters of plagioclase form patches within the amphiboles (FOV = 5.5 mm; image 1271B_083). (F) Higher magnification image of E showing the three major mineral phases, plagioclase (P), amphibole (A), and olivine (O) (FOV = 1.4 mm; image 1271B_036).
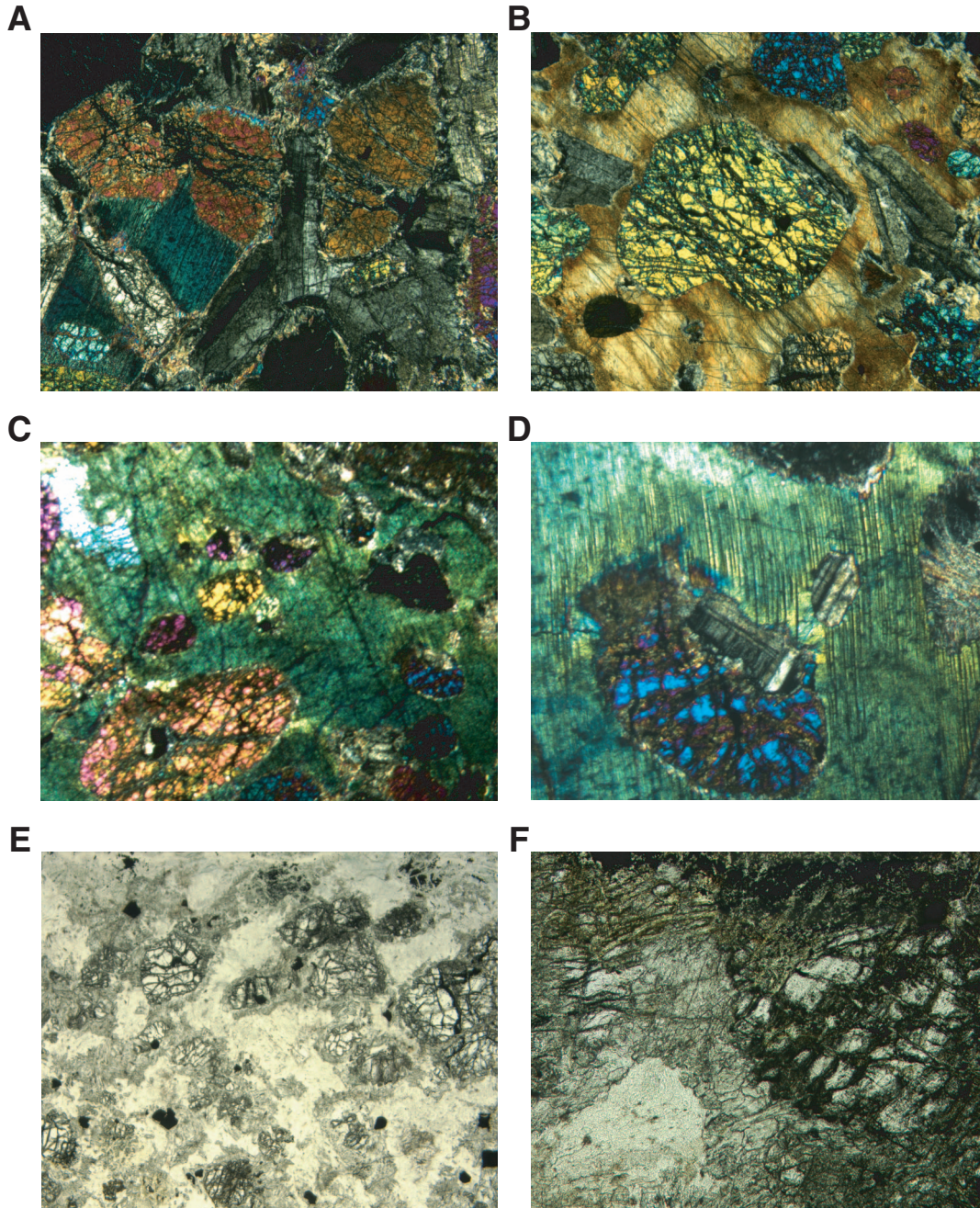
Figure F19. A. Close-up photograph of a 1-cm-wide xenolith of dunite in gabbroic material now replaced by amphibolite (interval 209-1271B-17R-1, 44.5–48 cm). **B, C.** Photomicrographs showing the reaction zone between xenolithic olivine and amphibolite at the contact between the xenolith in A (Sample 209-1271B-17R-1, 45–48 cm) (field of view = 5.5 mm); (B) ghosts of a symplectic mineral assemblage, now totally altered, are still recognizable (plane-polarized light: blue + light gray filters; image 1271B_085); (C) cross-polarized light: blue + light gray filters; image 1271B_084).
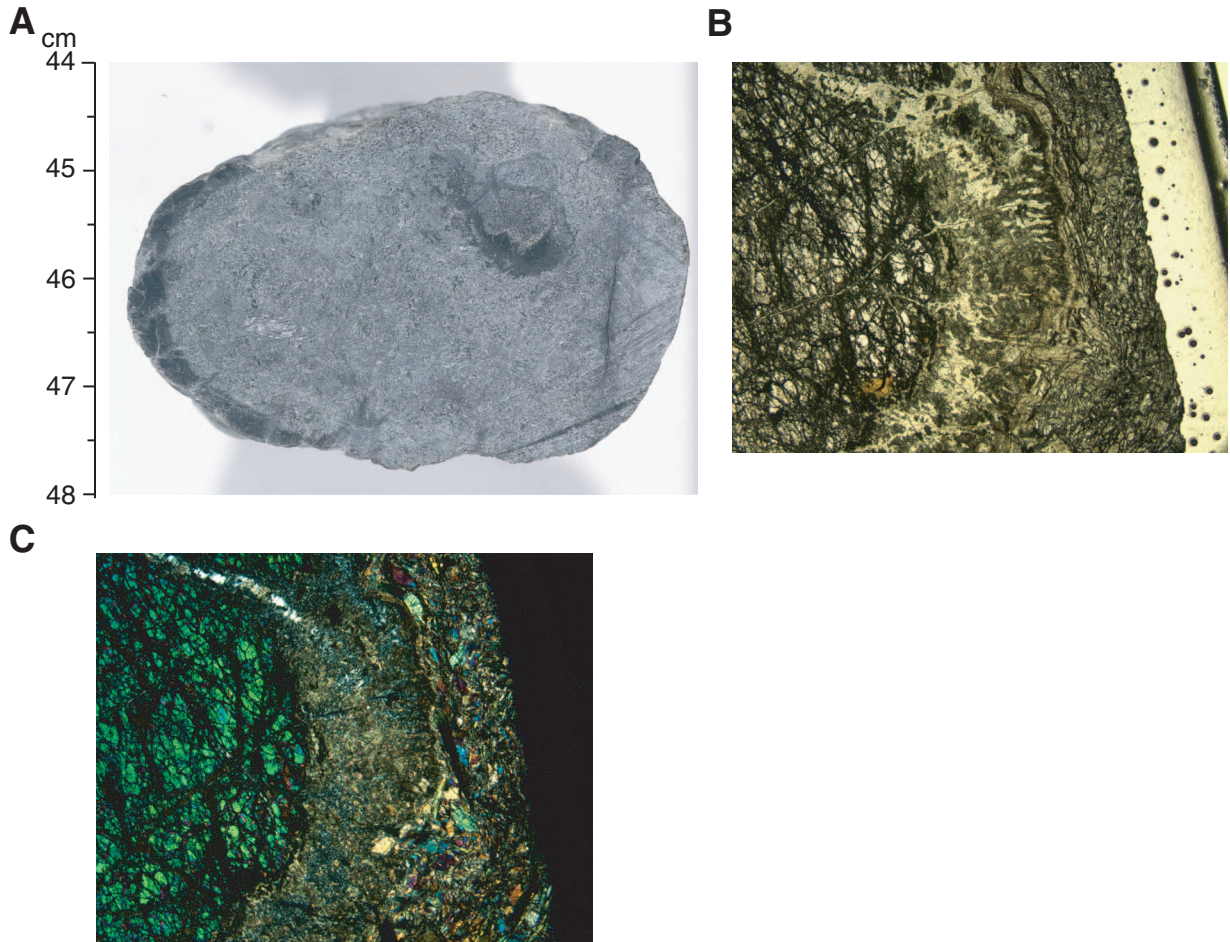
Figure F20. Photomicrographs showing gabbroic rocks from Hole 1271B. **A, B.** Sample 209-1271B-5R-1, 12–14 cm (cross-polarized light [XPL]: blue filter). (A) Euhedral brown amphibole grains in a matrix of altered plagioclase. Note that the upper grain is strained and so is not in complete optical continuity. Fresh plagioclase is preserved near the junction of the amphibole grains (field of view [FOV] = 5.5 mm; image 1271B_095). (B) Euhedral rutile grains (dark brown) included in, and at the boundaries of, small brown amphibole grains (FOV = 2.75 mm; image 1271B_096). **C.** Ophitic clinopyroxene enclosing subhedral plagioclase grains. Note how thin and laterally continuous clinopyroxene separates some of the plagioclase grains in the central cluster (Sample 209-1271B-5R-1, 5–7 cm) (XPL: blue filter; FOV = 5.5 mm; image 1271B_097). **D.** This brown amphibole grain has thin extensions into altered plagioclase, oriented orthogonal to the main amphibole grain. To the left of the field of view, the amphibole grain is massive and subhedral (Sample 209-1271B-5R-1, 24–27 cm) (XPL: blue filter; FOV = 5.5 mm; image 1271B_098).
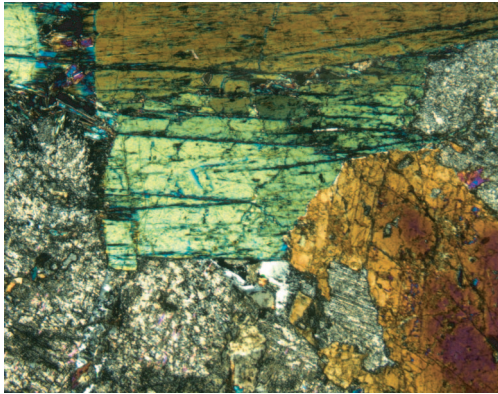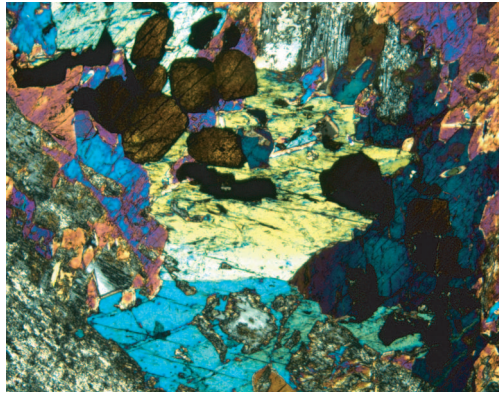
Figure F21. Downhole variability of alteration intensity based on macroscopic observations in Hole 1271A, which consists mainly of completely serpentinized harzburgite and dunite. TD = total depth.
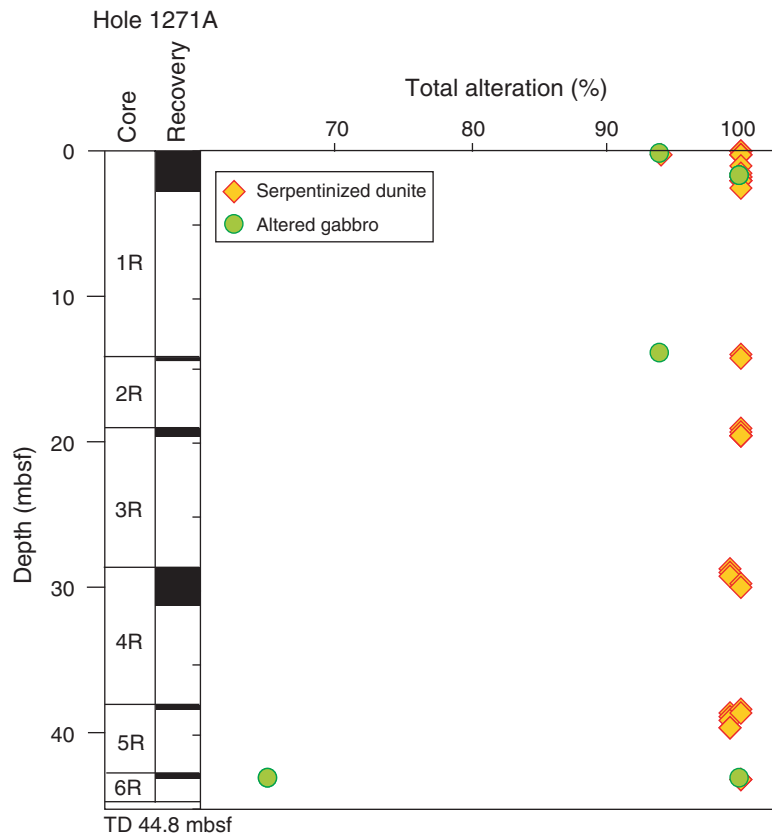
Figure F22. A. Close-up photograph of dunite that has a light green-gray groundmass hosting abundant, transgranular, black serpentine-magnetite veins oriented mainly parallel to the long axis of core (interval 209-1271A-1R-1, 70–80 cm). **B.** XRD analysis shows that the sample consists of serpentine and magnetite.

A

B

Lizardite-1T, aluminian: 11-386: $(Mg,Al)_3(Si,Al)_2O_5(OH)_4$
Magnetite, syn: JCPDS 19-0629: $FeFe_2O_4$
Chrysotile-2Mcl: 21-1262: $Mg_3Si_2O_5(OH)_4$

209-1271A-1R-1, 73-77 cm

$°2\theta\ CuK_\alpha$
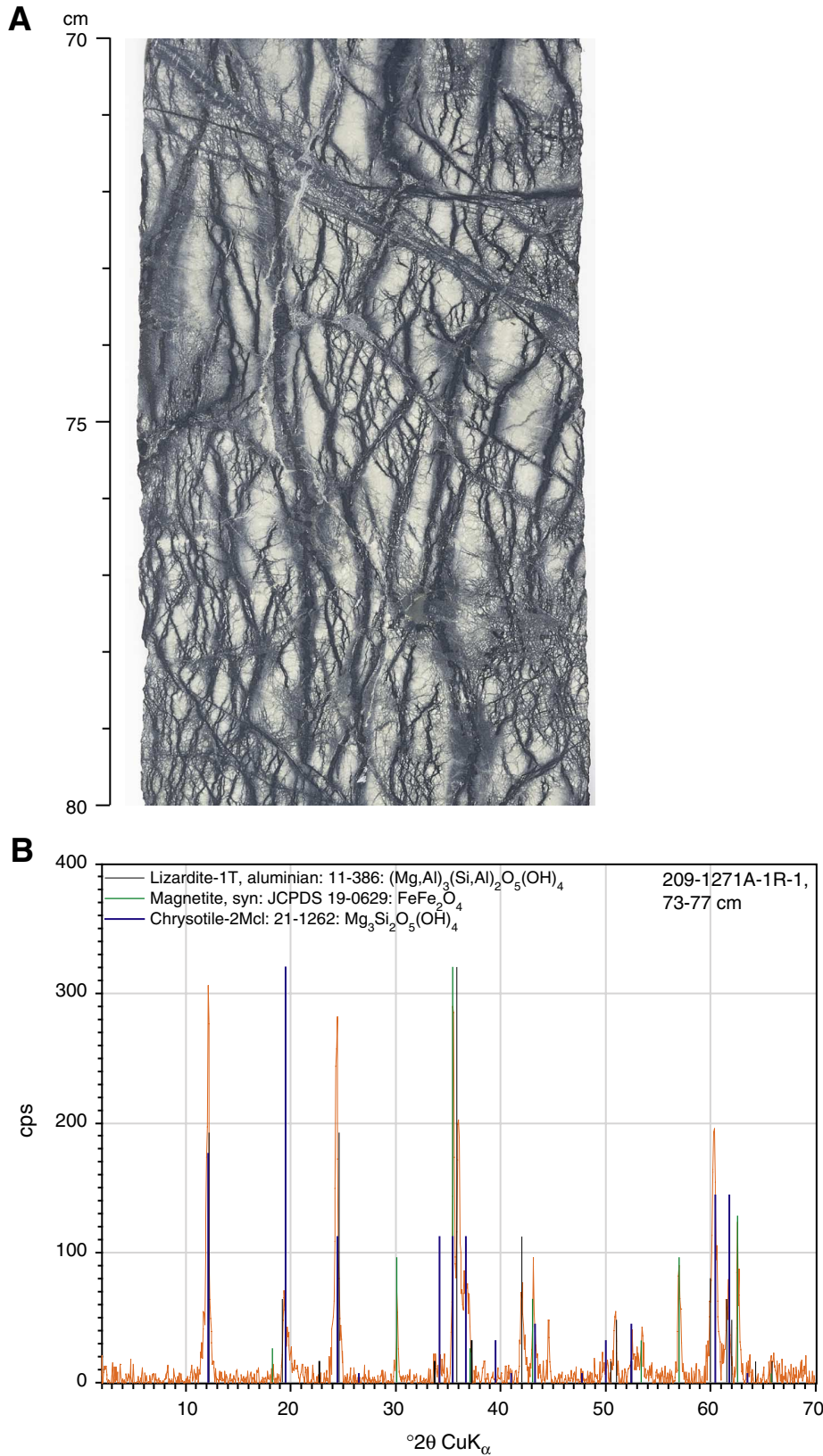
Figure F23. A. Close-up photograph of completely altered dunite has experienced substantial brucite alteration. This style of alteration is macroscopically indistinguishable from serpentinization (interval 209-1271A-4R-2, 24–36 cm). **B.** Photomicrograph showing that brucite forms aggregates of fine, elongate crystals with anomalous, brown interference colors surrounded and interpenetrated by serpentine. This indicates that the brucite has been partially transformed during serpentinization and that brucite formed prior to serpentine (Sample **209-1271A-4R-2, 29–31 cm**) (cross-polarized light: blue filter; field of view = 1.4 mm; image 1271A_005). **C.** XRD spectra for Sample 209-1271A-4R-2, 32–37 cm, shows prominent brucite peaks.
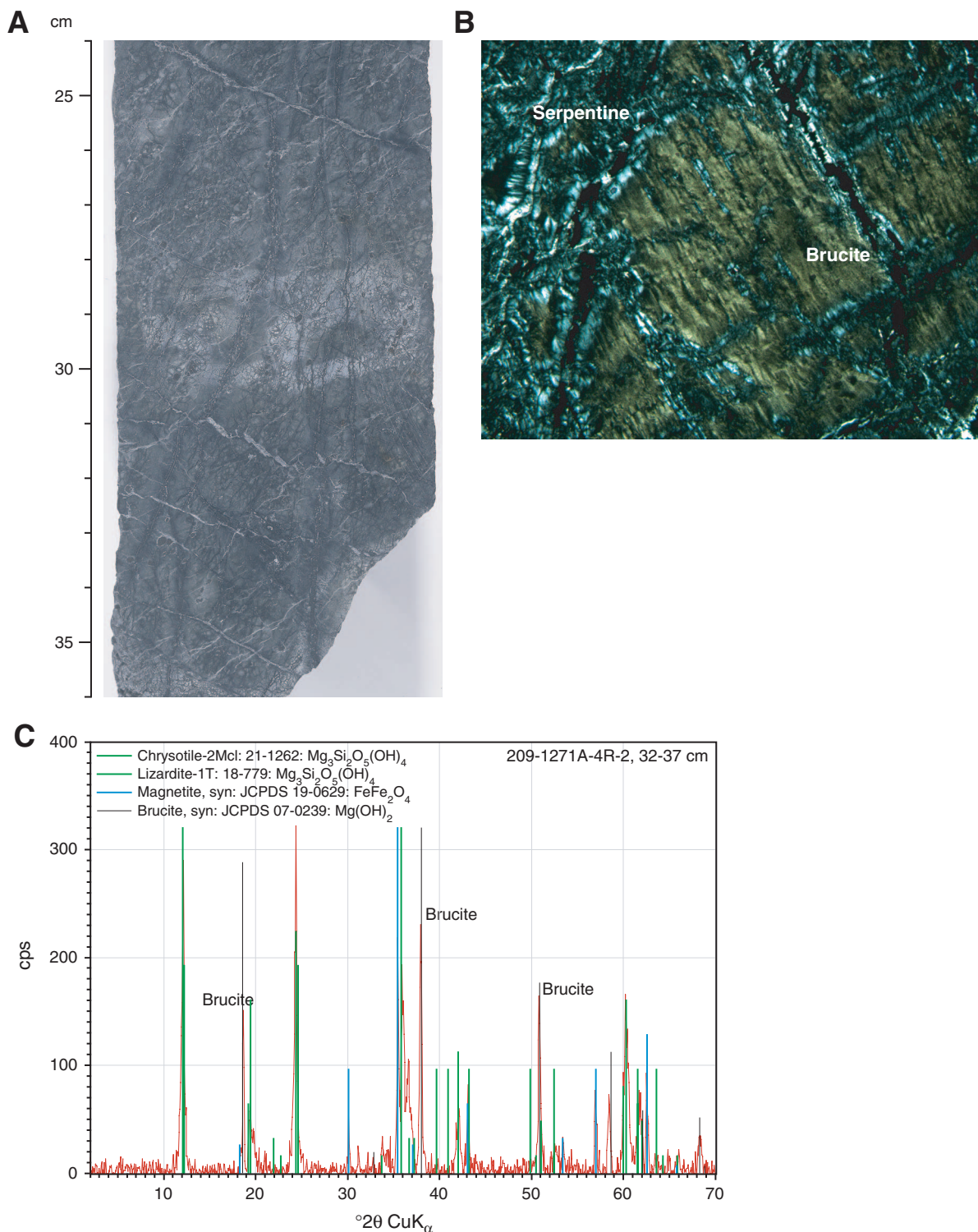
Figure F24. Veins in Hole 1271A consist predominantly of serpentine, followed by talc, amphibole, magnetite, and carbonates. Details of the vein statistics are presented in Table T3, p. 121. This pie chart has been generated using volume normalized data.
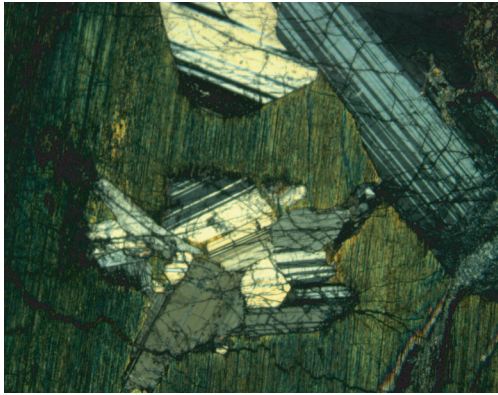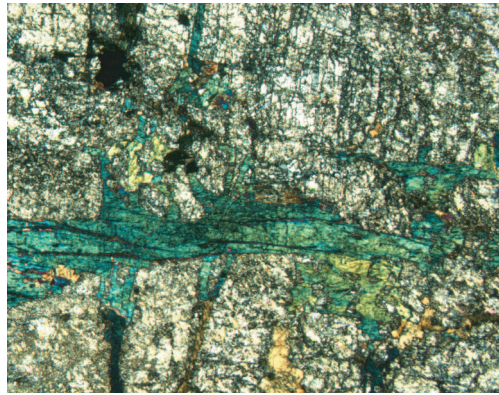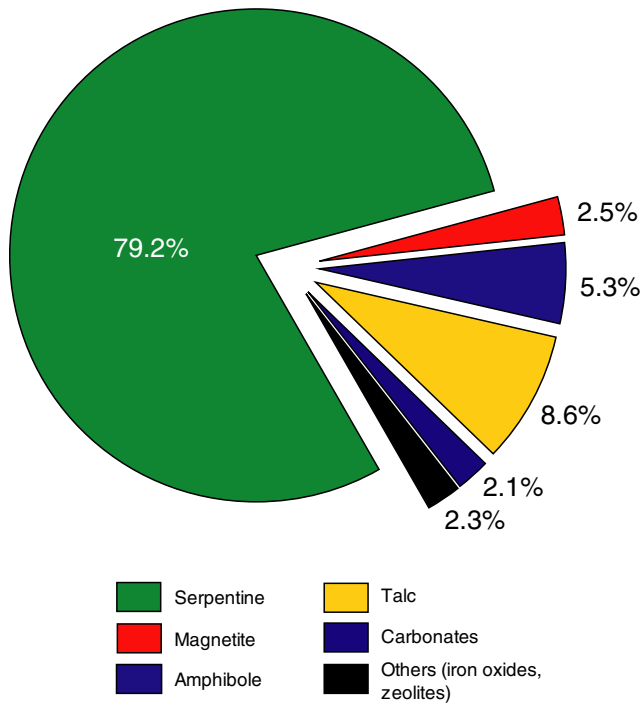
Figure F25. Downhole variability of alteration intensity based on macroscopic observations in Hole 1271B, which consists mainly of completely serpentinized harzburgite and dunite. TD = total depth.
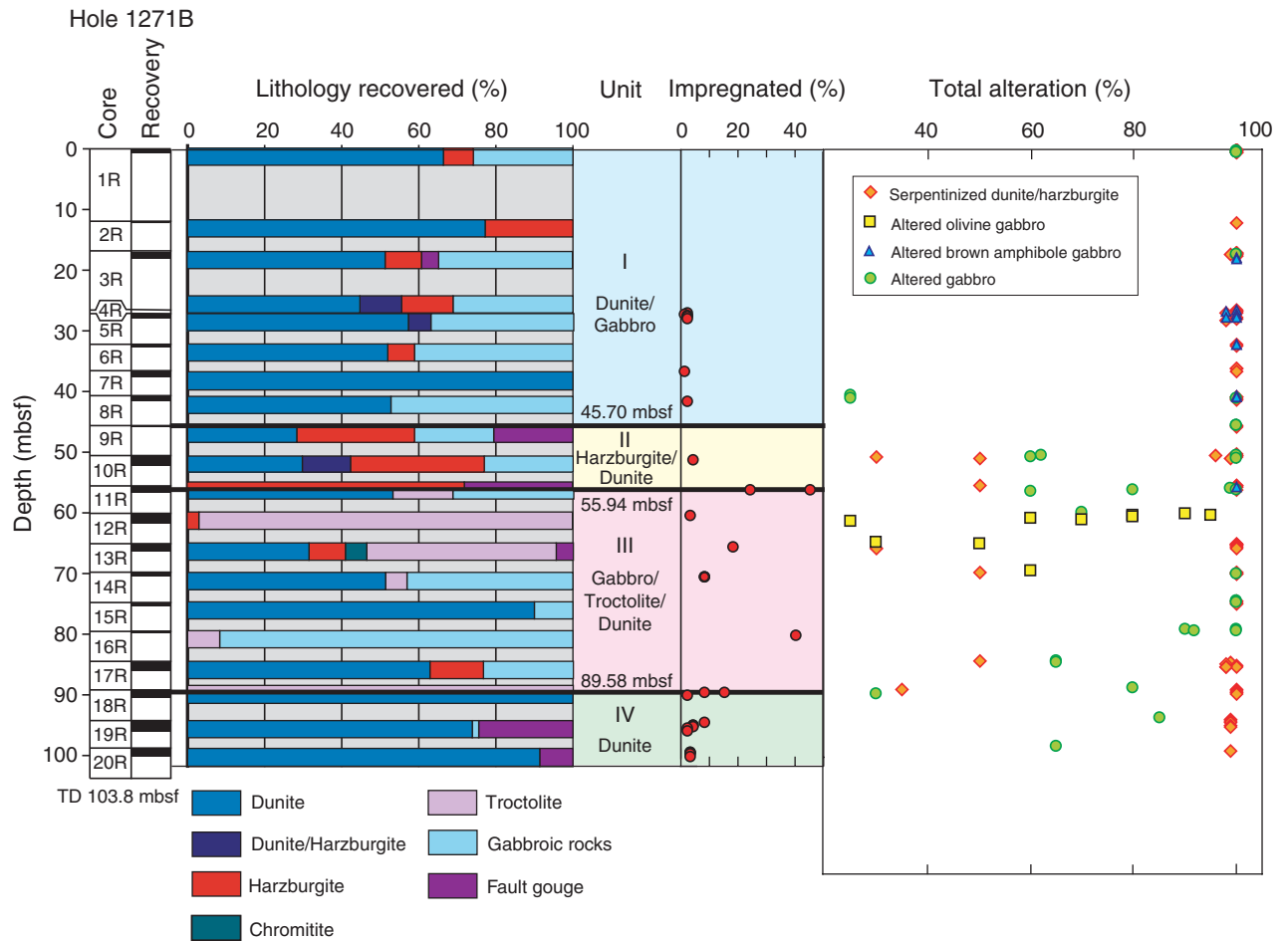
Figure F26. Photomicrograph showing networks of fine-grained chlorite-sericite-amphibole developed locally in fresh olivine-bearing dunite. Locally these assemblages replace primary minerals, possibly plagioclase or pyroxene. In contrast, olivine crystals are entirely fresh and show sharp boundaries to the chlorite-sericite-amphibole alteration assemblages (Sample **209-1271B-10R-1, 40–43 cm**) (cross-polarized light: blue + dark gray filters; field of view = 5.5 mm; image 1271B_029).
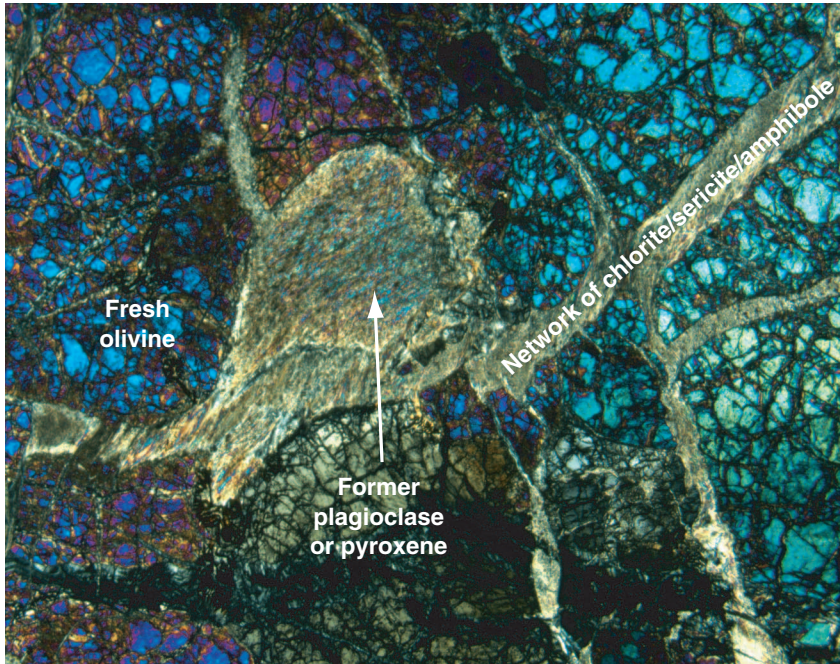
Figure F27. Photomicrographs showing olivine replaced by a fine-grained amphibole, chlorite, and minor sericite. The former olivine grain boundaries, outlined by rims of magnetite (arrows), are still recognizable (Sample 209-1271B-13R-1, 20–24 cm). **A.** Plane-polarized light: blue filter; field of view = 2.75 mm; image 1271B_051). **B.** Cross-polarized light: blue filter; field of view = 2.75 mm; image 1271B_052.

A

B
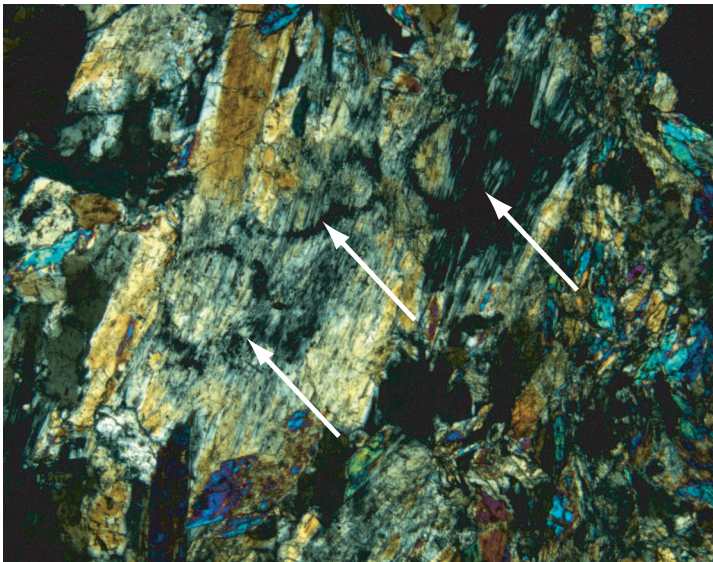
Figure F28. Photomicrograph showing completely talc-altered former orthopyroxenes with relict vermicular spinel (Sample **209-1271B-10R-1, 40–43 cm**) (cross-polarized light: blue filter; field of view = 2.75 mm; image 1271B_066).
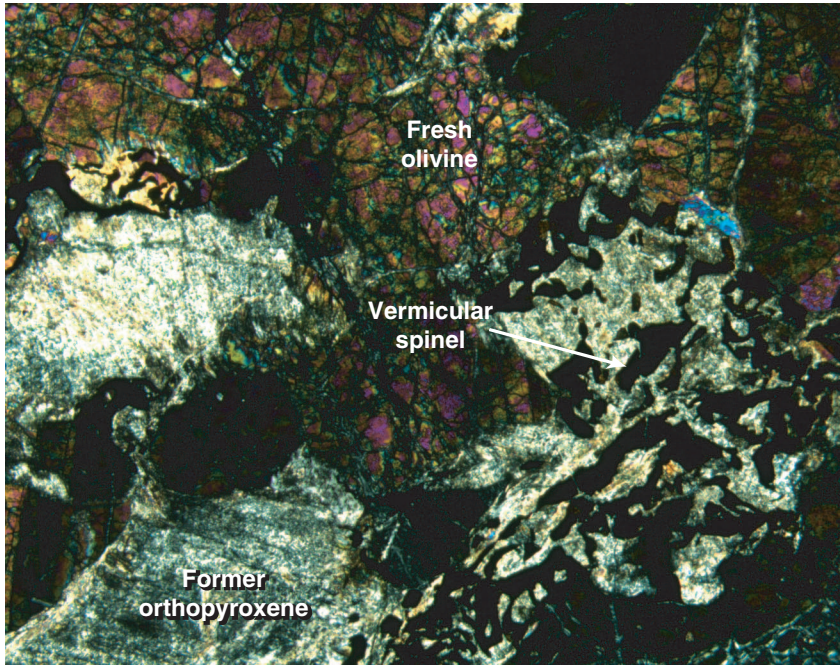
Figure F29. Photomicrographs showing incomplete serpentinization of olivine in a dunite. Relict fresh olivine with a mesh texture defined by serpentinization along internal cracks is bordering a domain of complete serpentinization (Sample **209-1271B-10R-1, 40–43 cm**). **A.** Cross-polarized light: blue filter; field of view = 5.5 mm; image 1271B_027. **B.** Plane-polarized light: blue + dark gray filters; field of view = 5.5 mm; image 1271B_028.
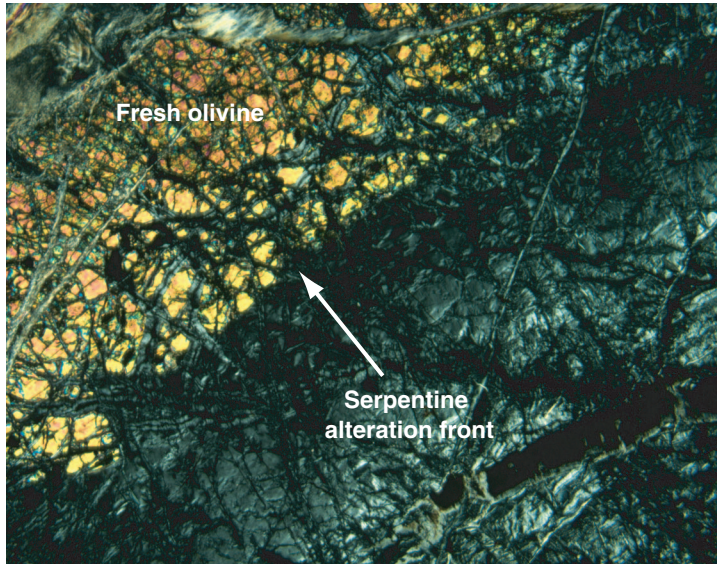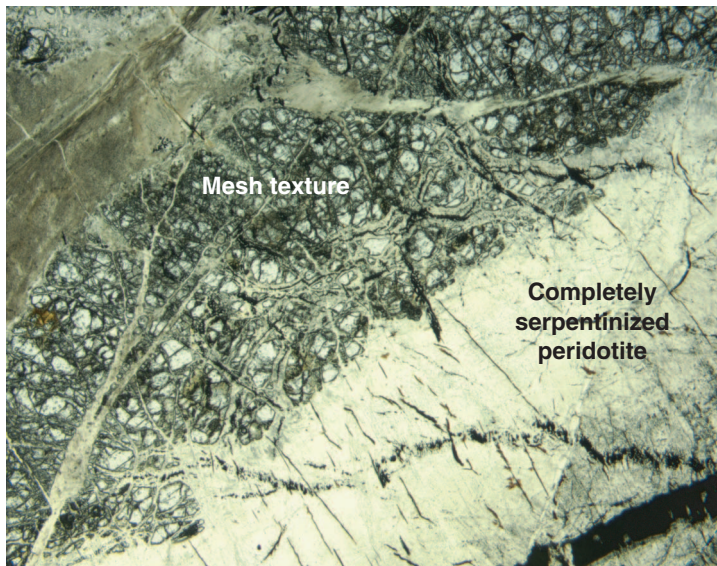
Figure F30. Veins in Hole 1271B consist of serpentine, magnetite, talc, carbonates and rare quartz. Details of the vein statistics are presented in Table T3, p. 121. This pie chart has been generated using volume-normalized data.
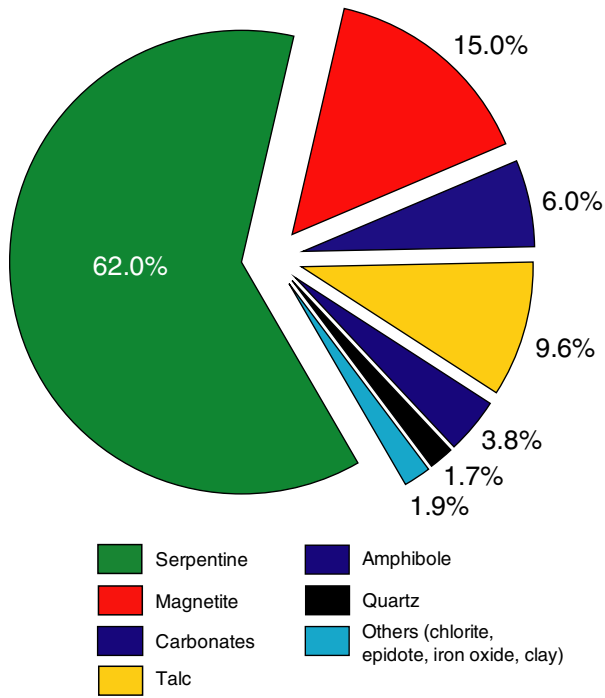
Figure F31. Photomicrographs illustrating the complex, multistage evolution of brown amphibole gabbro during deformation and metamorphism. A–C. Sample **209-1271B-14R-1, 25–29 cm** (cross-polarized light [XPL]: blue filter). (A) Ductile deformation. Amphibole porphyroclast with wavy extinction (a(p)) represents a microboudin that has been syntectonically recrystallized to fine-grained amphibole neoblasts (a(n)) along its margins (sc(n) = sericite-altered plagioclase neoblasts) (field of view [FOV] = 5.5 mm; image 1271B_058). (B) Amphibole porphyroclasts (a(p)) have been partially replaced by amphibole neoblasts (a(n)). The amphibole is surrounded by bands of former plagioclase neoblasts that have been statically altered to sericite-bearing assemblages (sc(n)) (FOV = 5.5 mm; image 1271B_059). (C) Outline of a "ghost" plagioclase porphyroclast replaced by sericite-bearing assemblages (sc(p)). The original polysynthetic twinning of the plagioclase porphyroclasts (white arrows) is pseudomorphed by sericite, quartz, and secondary plagioclase. Former plagioclase neoblasts are also pseudomorphically replaced by sericite aggregates (sc(n); red arrows) (FOV = 2.75 mm; image 1271B_060). (Continued on next page.)
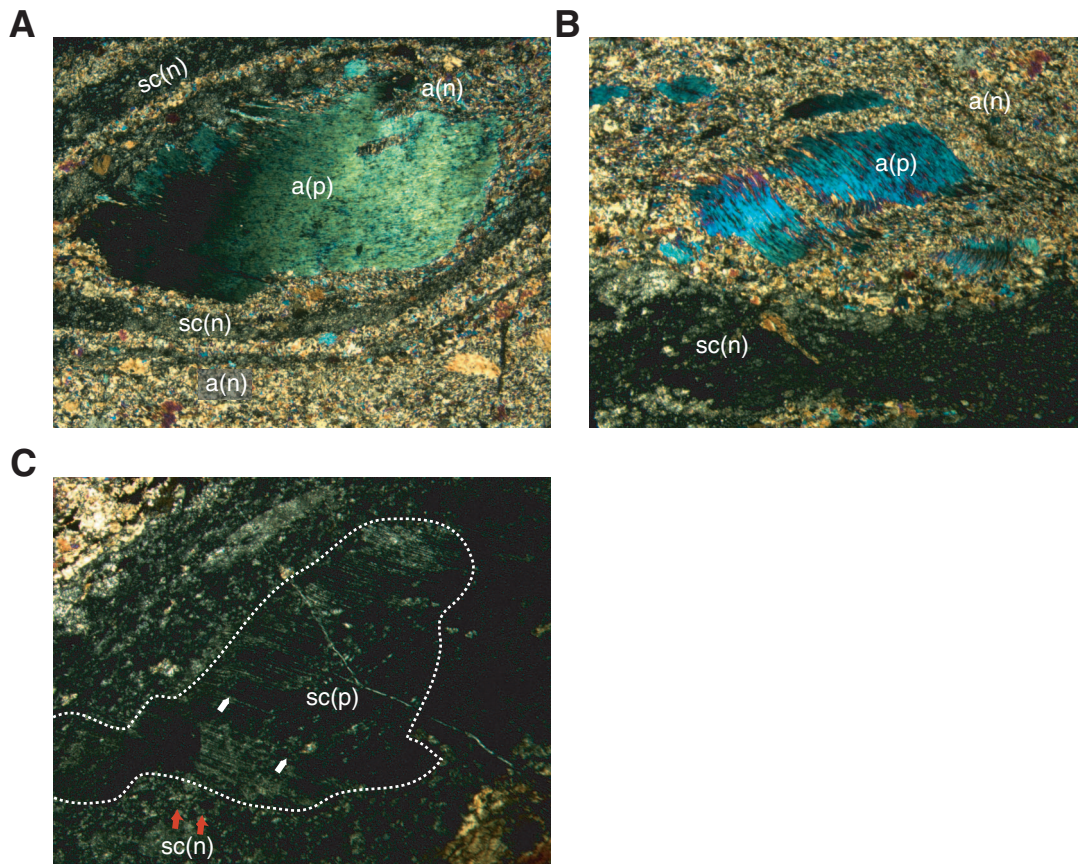
Figure F31 (continued). D, E, F. Sample **209-1271B-11R-1, 44–46 cm** (XPL: blue + dark gray filters; FOV = 1.4 mm). (D) Intergrowth of fibrous amphibole (a2) and chlorite (ch) after former high-temperature amphibole. Fibrous amphibole and chlorite are stretched and deformed along shear bands (image 1271B_049). (E) Amphibole-chlorite schists after gabbroic protolith. The secondary fibrous amphibole (a2), sericite (sc), and chlorite (ch) are stretched and banded, defining the schistosity (image 1271B_048). (F) Fold of fibrous amphibole (a2) in a amphibole-chlorite schists after gabbro. Chlorite (ch) crystallized in the pressure shadow of the inner part of the fold. The matrix is composed of fine fibrous aggregates of secondary amphibole (a2) and chlorite (a2ch may replace former high-temperature amphibole) alternating with dark bands of sericite and hydrogrossular (sc & hgr; may by replacing former plagioclase) (Sample **209-1271B-11R-1, 55–57 cm**) (XPL: blue + dark gray filters; FOV = 5.5 mm; image 1271B_053).
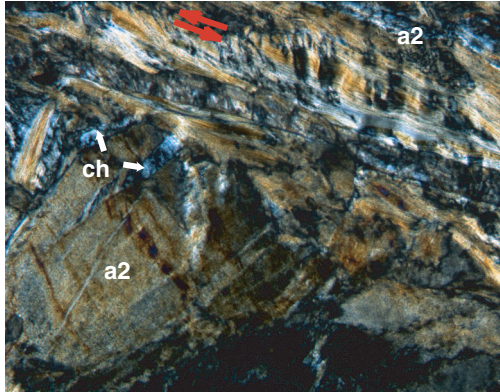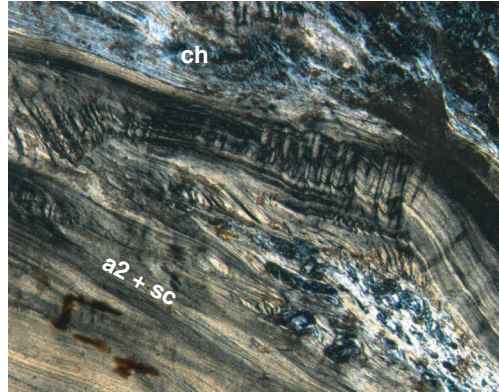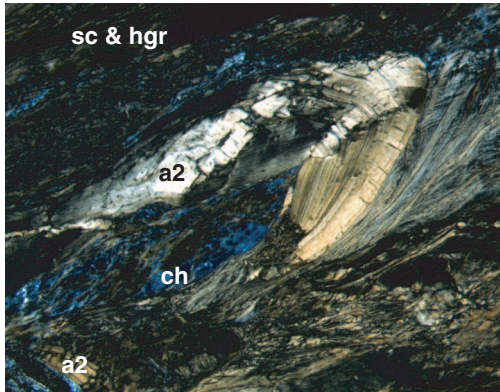
Figure F32. Photomicrographs showing deformation-metamorphism path in amphibole-bearing dunite as revealed by textural observations (Sample **209-1271B-12R-1, 126–131 cm**) (cross-polarized light: blue filter). **A.** Coarse-grained aggregate of subhedral olivine (ol) showing smooth, curved boundaries with interstitial amphibole (a). Continuous extinction of the interstitial amphibole indicates that it is a single crystal. The smooth grain boundaries suggest textural equilibrium with olivine. This is the earliest generation of amphibole that could be defined on a textural basis in this rock type (field of view [FOV] = 5.5 mm; image 1271B_087). **B.** The olivine-amphibole aggregates locally experienced ductile deformation. Evidence for ductile deformation in amphibole includes wavy extinction of large porphyroclasts that are surrounded by a mantle of amphibole neoblasts. These textures indicate a high-temperature ductile deformation of amphibole-bearing dunite aggregates (FOV = 5.5 mm; image 1271B_088). **C.** Coarse olivine (ol) and proto-amphibole (a) are replaced along a band consisting of fine-grained amphibole-chlorite-serpentine schist (a-ch-se) in a brittle microshear band. This shear band is subparallel to the ductile deformation plane defined by elongated amphibole porphyroclasts (a). Olivine is transformed to serpentine (se) along cracks that do not crosscut the shear band. These textural relationships suggest a retrograde breakdown of olivine under greenschist facies conditions coeval with the development of the amphibole-chlorite-serpentine schist (FOV = 5.5 mm; image 1271B_089). White rectangle is the outline of the enlargement shown in D. **D.** Detail of photomicrograph shown in C (white rectangle) illustrating the development of different serpentine textures. A fibrous and interlocking serpentine texture (se1) is generated along cracks (red arrows). This serpentine texture is overprinted by a second generation of banded serpentine (se2) subparallel to the schistosity defined by the amphibole-chlorite-serpentine band. The se2 texture is in turn replaced by a corona of fine-grained amphibole-chlorite (a3 + ch) in the contact with the amphibole-chlorite-serpentine schist (FOV = 2.75 mm; image 1271B_090). (Continued on next page.)
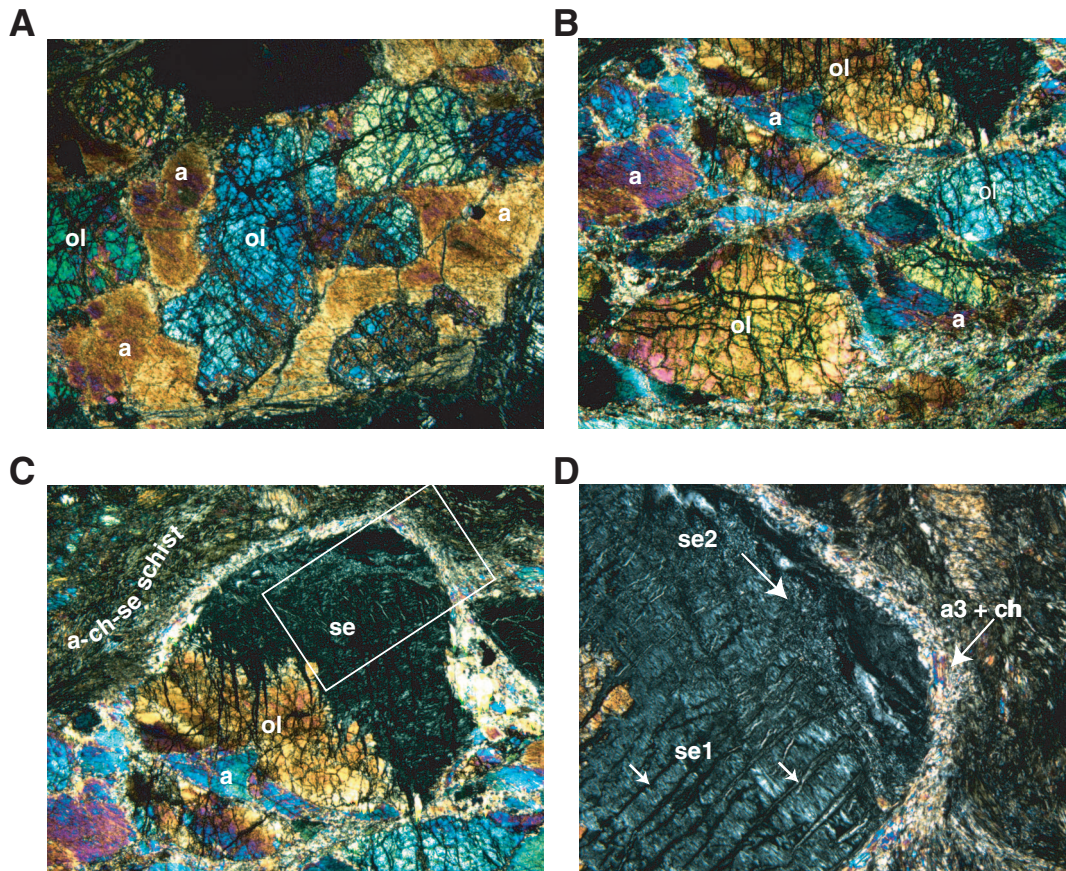
Figure F32 (continued) E. Interlocking serpentine texture (se) after olivine (ol) breakdown is replaced by fine-grained amphibole (a3) growing topotactically in serpentine (FOV = 1.4 mm; image 1271B_091). **F.** Retrograde breakdown of high-temperature amphibole porphyroclast (a) to a later fibrous amphibole (a2) along an amphibole-chlorite-serpentine (a-ch-se) microshear band. Note that fibers of the secondary amphibole are oriented parallel with respect to the schistouos band suggesting a retrograde synkinematic formation under greenschist facies conditions (FOV = 2.75 mm; image 1271B_092).

E
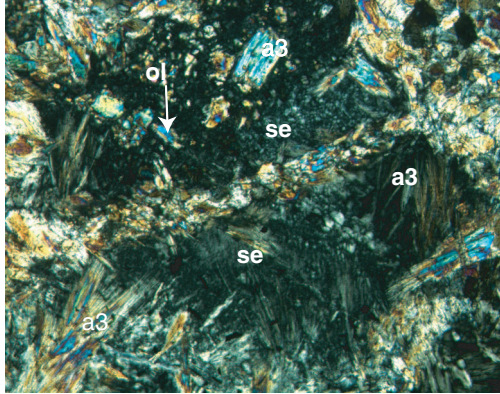
F
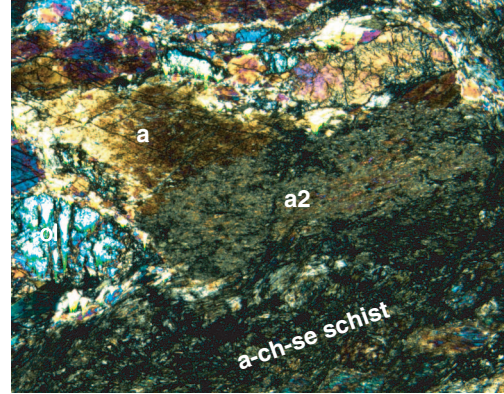
Figure F33. Photomicrograph showing amphibole-bearing dunite with a crosscutting relationship between early serpentinization of olivine and later alteration of the former gabbroic dikelets to an assemblage of chlorite-sericite-amphibole (Sample **209-1271B-10R-1, 40–43 cm**) (cross-polarized light: blue filter; field of view = 5.5 mm; image 1271B_026).
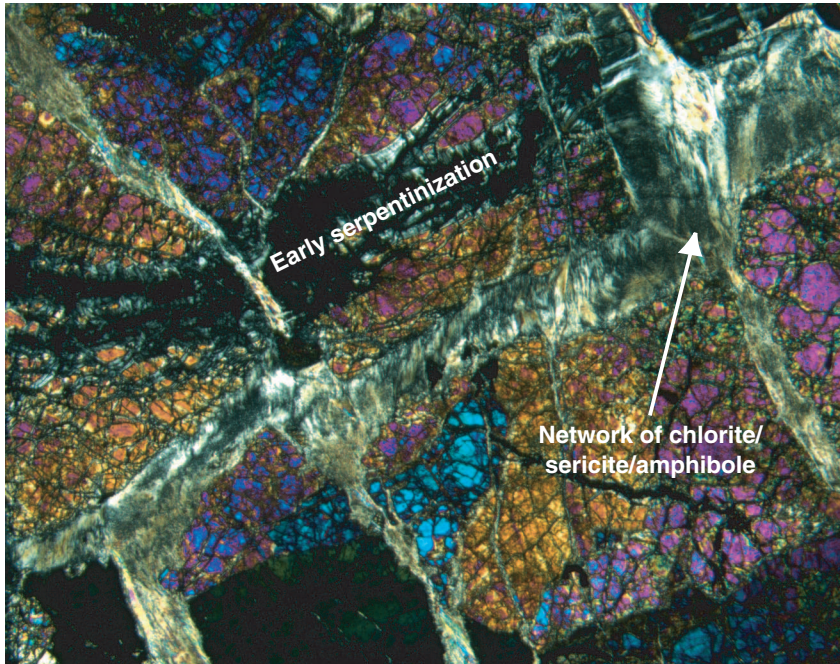
Figure F34. A. Mineral-fluid phase diagram for the system Mg-Ca-Si-O-H at 200°C and 500 bar, constructed using thermodynamic data from Johnson et al. (1992) and assuming $\log(\alpha Ca^{2+}/\alpha^2 H^+) = 6$. Black trend = hypothetical evolution path of fluids dissolving olivine at a higher rate than hydrous minerals are precipitated. The drop in silica activity is solely the result the decrease in the orthosilicate activity coefficient as a function of decreasing pH (calculated with SUPCRT92; Johnson et al., 1992). Black square = hydrothermal fluids from the Lost City vent site (Kelley et al., 2001) respeciated for 200°C and 500 bar and assuming olivine solubility controls $a_{Mg^{2+}}$. The shaded field encompasses fluid compositions from a lherzolite-seawater reaction experiment at 200°C and 500 bar conducted by Janecky and Seyfried (1986). Red arrows = schematic fluid evolution paths for pyroxene-poor lithologies proposed by Seyfried and Dipple (1980). **B.** Same as A but for T = 400°C. The shaded field labeled "R&L" represents fluid compositions from the Rainbow and Logatchev hydrothermal sites, respeciated for 400°C and 500 bar (Charlou et al., 2002). In situ pH values of these fluids range 4.5–5. Silica activities = 6–7 mmol/kg, and Mg^{2+} activity was assumed to be 0.1 mmol/kg.
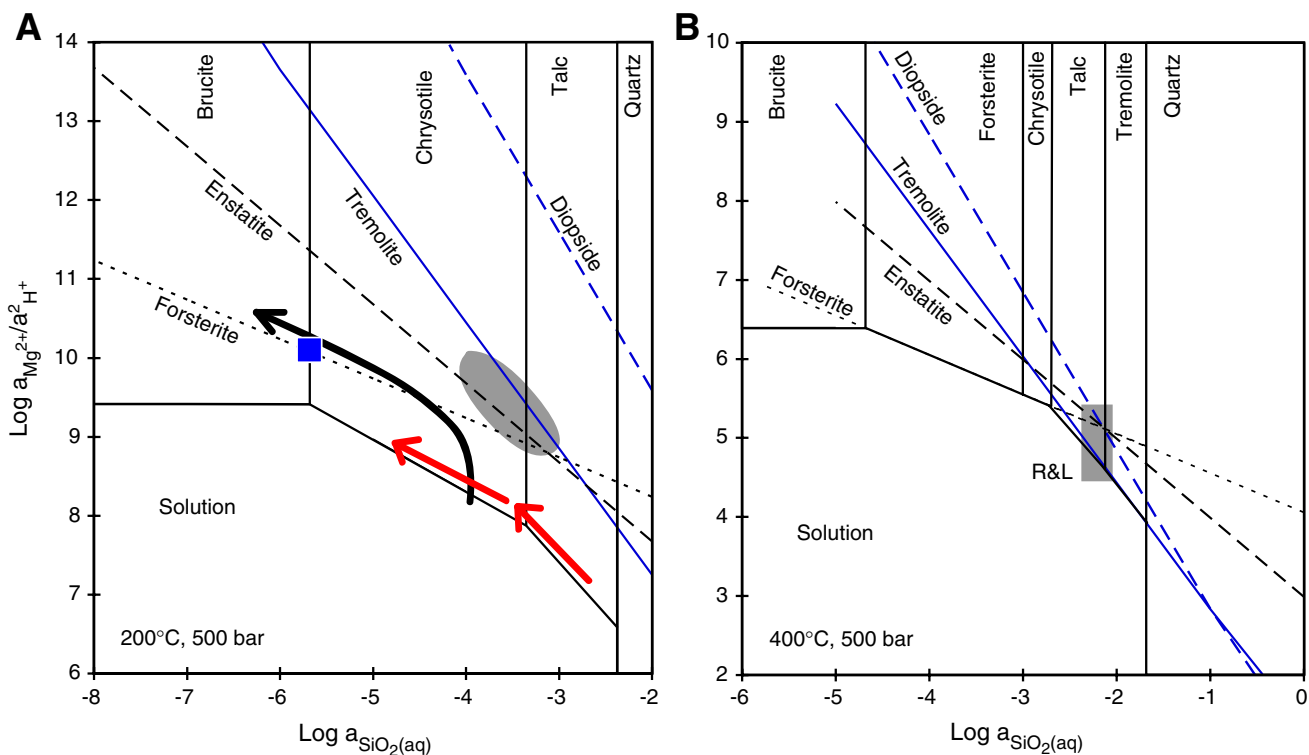
Figure F35. Plot showing recovery, unit boundaries, and the locations of brittle and ductile shear zones and impregnated horizons for Holes 1271A and 1271B. Green and red markers denote the locations of brittle and ductile shear zones. Purple shaded intervals on recovery plots denote the locations and thickness of impregnated horizons. TD = total depth.
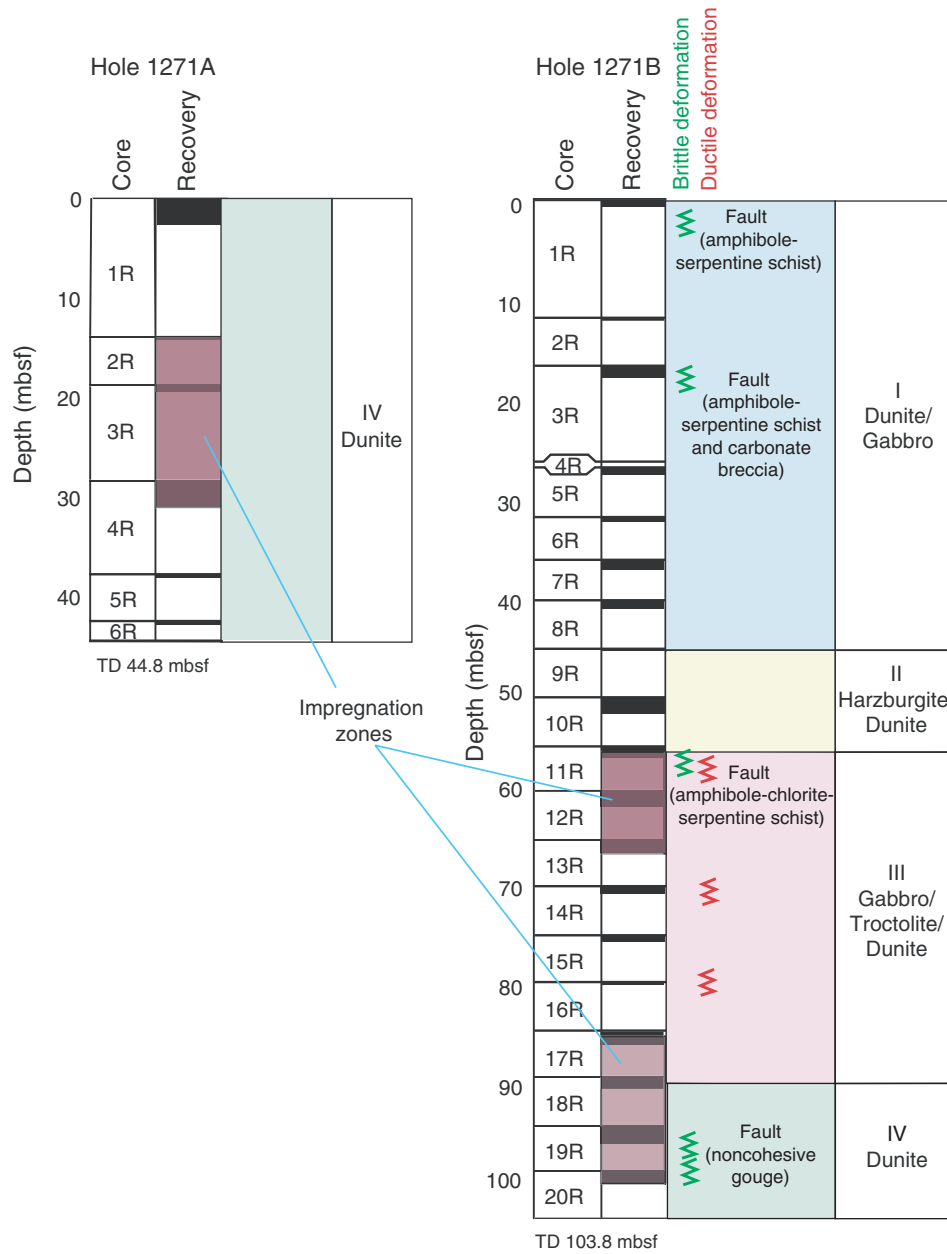
Figure F36. Downhole plot of crystal-plastic deformation intensity for Holes 1271A and 1271B. Plot for Hole 1271A represents a five-piece running average, weighted by piece length, for deformation intensities measured on 102 pieces of core. Plot for Hole 1271B represents a seven-piece running average, weighted by piece length, for deformation intensities measured on 341 pieces of core.
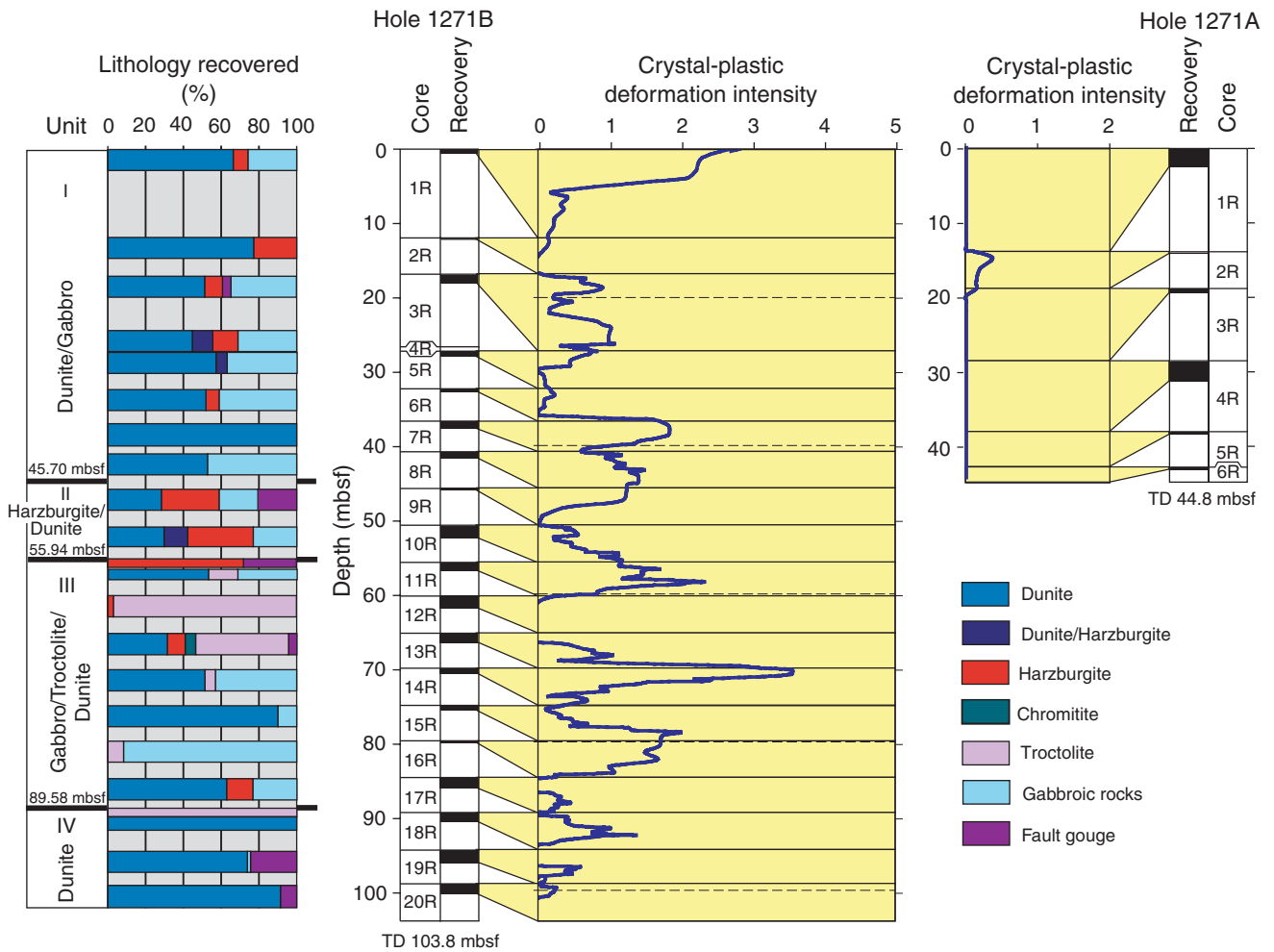
Figure F37. A. Distribution of deformation fabrics by lithology as logged in 341 pieces of core from Hole 1271B. **B.** Distribution of crystal-plastic deformation by intensity grade. For simplicity, different lithologies have been combined from the histograms in A.
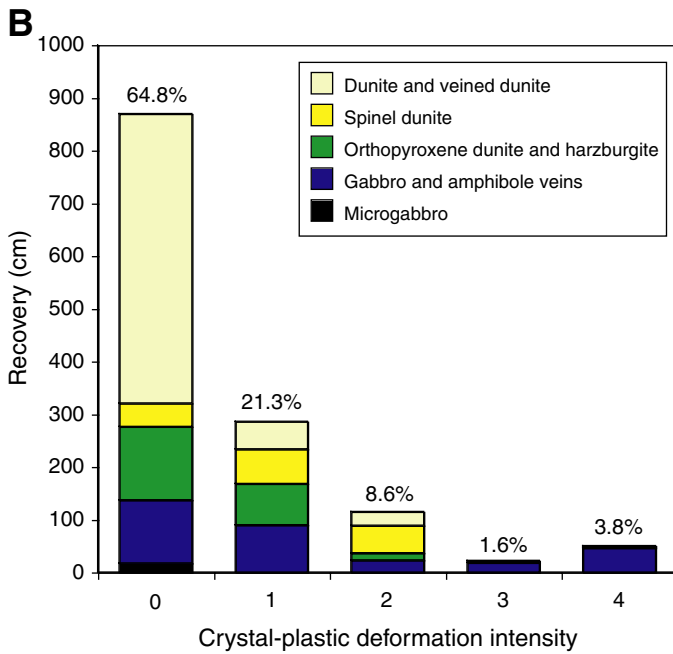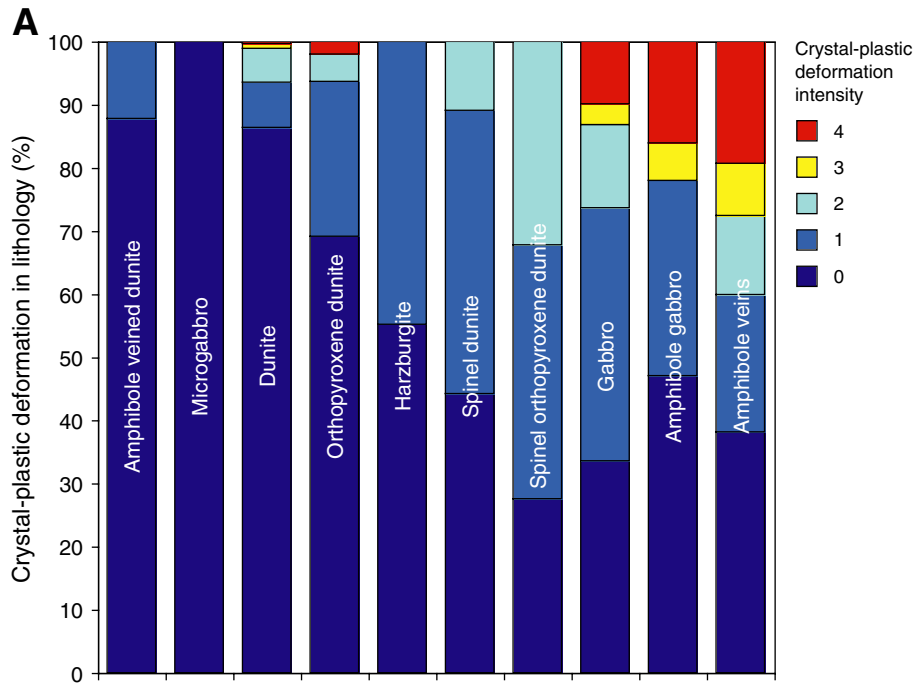
Figure F38. Photomicrographs of harzburgite, orthopyroxene, dunite, and a chromitite layer from Hole 1271B. Ol = olivine, Opx = orthopyroxene, Sp = spinel, Tr = tremolite. **A.** Protointergranular orthopyroxene bastite in protointergranular harzburgite (Sample **209-1271B-6R-1 [Piece 2, 8–11 cm]**) (cross-polarized light [XPL]: blue filter; field of view [FOV] = 5.5 mm; image 1271B_108). **B.** Talc-chlorite-tremolite-magnetite pseudomorph of a stretched orthopyroxene rimmed by vermicular spinel within a sample of orthopyroxene dunite. Red arrows show sense of rotation due to shear prior to spinel precipitation and indicate normal sense shear (Sample **209-1271B-17R-1 [Piece 10, 60–62 cm]**) (plane-polarized light [PPL]; FOV = 5.5 mm; image 12741B_130). **C.** Talc-chlorite-tremolite-magnetite pseudomorph of a stretched orthopyroxene rimmed by vermicular spinel in orthopyroxene dunite. Red arrows show sense of rotation due to shear prior to spinel precipitation and indicate normal sense shear (Sample **209-1271B-17R-1 [Piece 10, 60–62 cm]**) (PPL; FOV = 5.5 mm; image 1271B_129). **D.** Primary chrome spinel layer in massive tremolite replacing a contact between dunite and porphyroclastic gneissic gabbro (Sample **209-1271B-14R-1 [Piece 7, 32–35 cm]**) (XPL: blue filter; FOV = 5.5 mm; image 1271B_117).
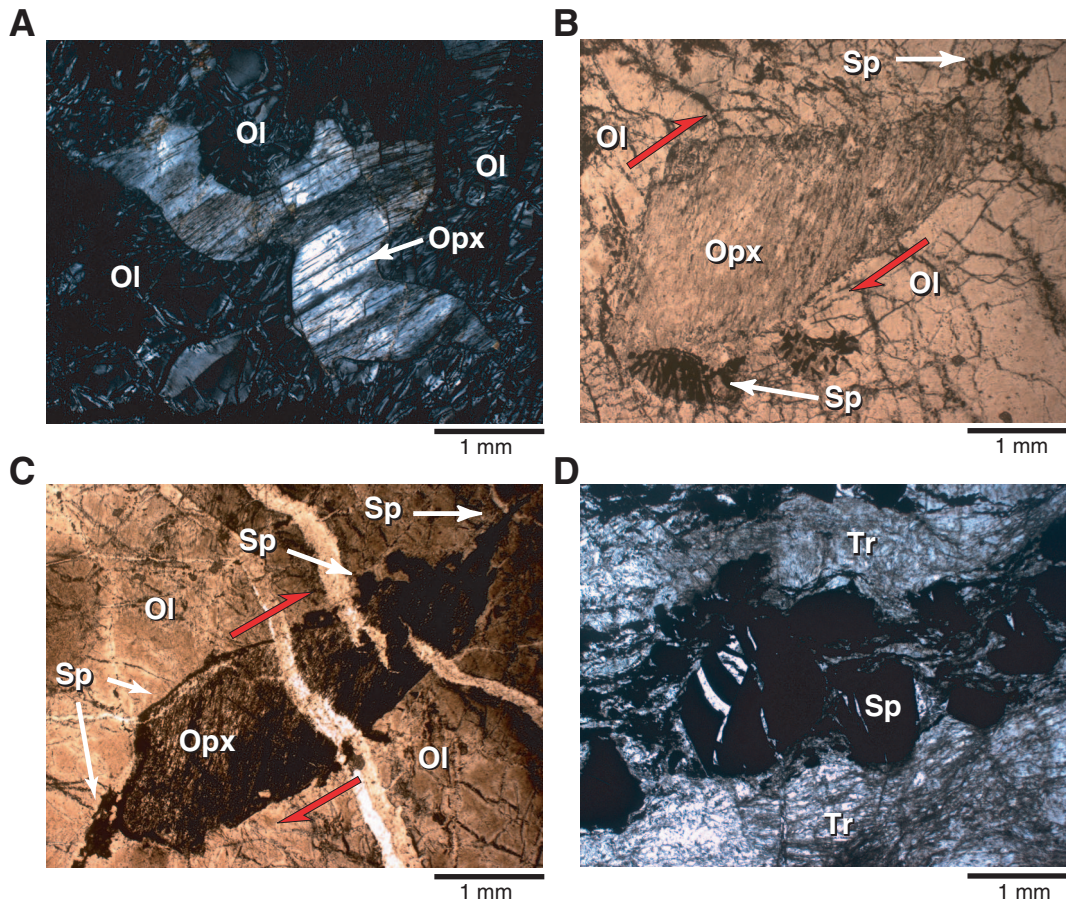
Figure F39. Close-up photographs of examples of crystal-plastic deformation. Sp = spinel, Ol = olivine, Am = amphibole. **A.** Chromitiferous dunite exhibiting a spinel foliation (interval 209-1271B-7R-1 [Piece 7, 48.5–57 cm]). **B.** Contact between coarse- and medium-grained troctolite including xenoliths and xenocrysts derived from dunite (interval 209-1271B-16R-1, 24–29.5 cm). **C.** Brown amphibole gabbro porphyroclastic mylonite (interval 209-1271B-14R-1, 25–29 cm). **D.** Net veined dunite or troctolitic gabbromylonite (interval 290-1271B-11R-1, 87–93 cm).
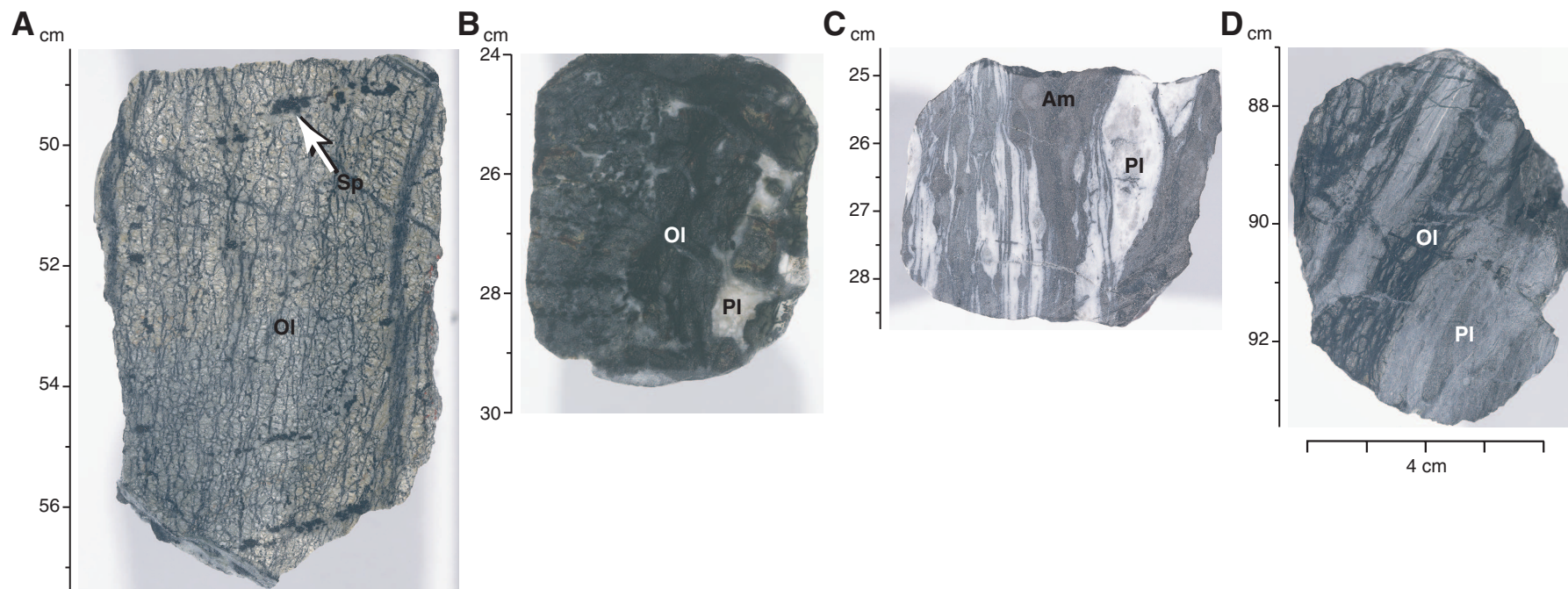
Figure F40. Lower hemisphere stereoplot showing the orientation of magmatic veins and spinel foliations in dunite in Holes 1271 and 1271B. Measurements were rotated into a common orientation using the measured paleomagnetic azimuth as described in **"Structures in Peridotite and Gabbroic Intrusions,"** p. 8, in "Mantle Upwelling, Melt Transport, and Igneous Crustal Accretion" in the "Leg 209 Summary" chapter.

Paleomagnetic North

Lower hemisphere,
equal area

■ 1271A Spinel foliations

◆ 1271B Spinel foliations

• 1271A and 1271B magmatic veins
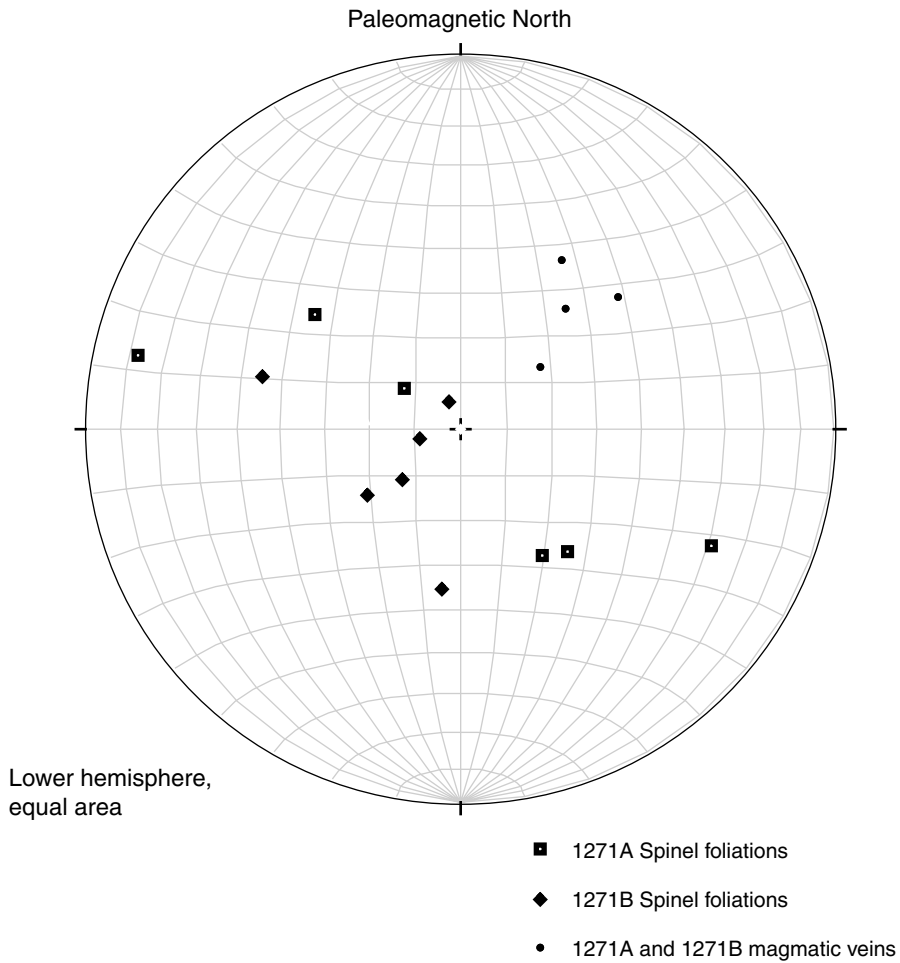
Figure F41. Photomicrographs of deformed and undeformed gabbroic veins. Pl = plagioclase, Ol = olivine, Cpx = clinopyroxene, Am = amphibole, Pr = prehnite, bAm = brown amphibole, Ab = albite. **A.** Undeformed, troctolitic gabbro showing a clinopyroxene oikocryst occluding rounded olivine and subhedral plagioclase laths (Sample 209-1271B-18R-1 [Piece 5, 20–23 cm]) (cross-polarized light [XPL]; field of view [FOV] = 5.5 mm; image 1271B_127). **B.** Weakly recrystallized plagioclase at margin of an unstrained primary plagioclase grain in troctolite. Zone of secondary amphibole has formed between the plagioclase and olivine at upper right (Sample 209-1271B-16R-1 [Piece 4, 24–27 cm]) (XPL: blue filter; FOV = 1.4 mm; image 1271B_118). **C.** Olivine porphyroclast in recrystallized olivine in impregnated dunite mylonite (Sample 209-1271B-11R-1 [Piece 17, 88–91 cm]) (plane-polarized light [PPL]: blue filter; FOV = 5.5 mm; image 1271B_111). (Continued on next page).
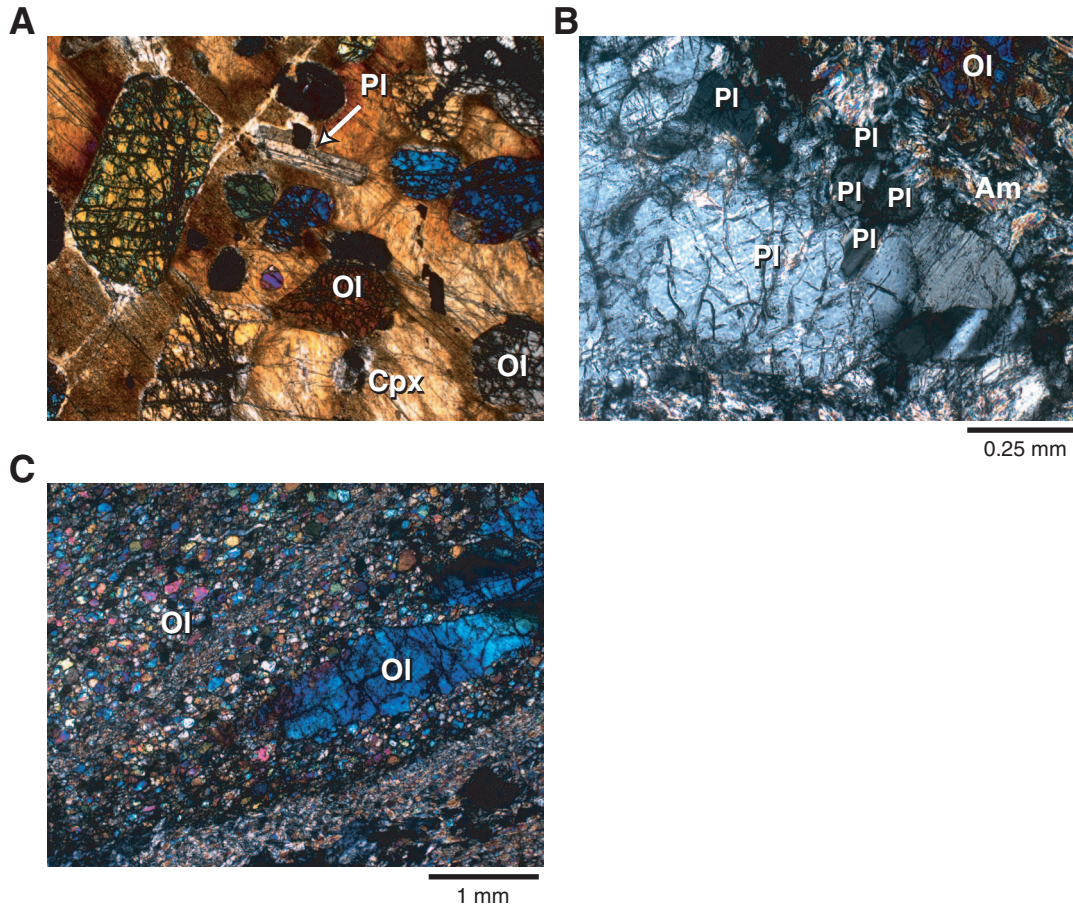
Figure F41 (continued). D–F. Sample **209-1271B-14R-1 (Piece 6, 25–29 cm).** (D) Brown amphibole gabbro mylonite with an amphibole augen in a banded matrix of secondary brown amphibole, after recrystallized pyroxene and olivine, and prehnite, and hydrogrossular after plagioclase (XPL: blue filter; FOV = 5.5 mm; image 1271B_112). (E) Secondary brown amphibole cutting across pseudomorphed mylonite bands, locally extending into and replacing the mafic bands in the same mylonite as in D. A secondary albite vein splits the brown amphibole vein (PPL: blue filter; FOV = 5.5 mm; image 1271B_137). (F) Same frame as E (XPL: blue filter; FOV = 5.5 mm; image 1271B_136).
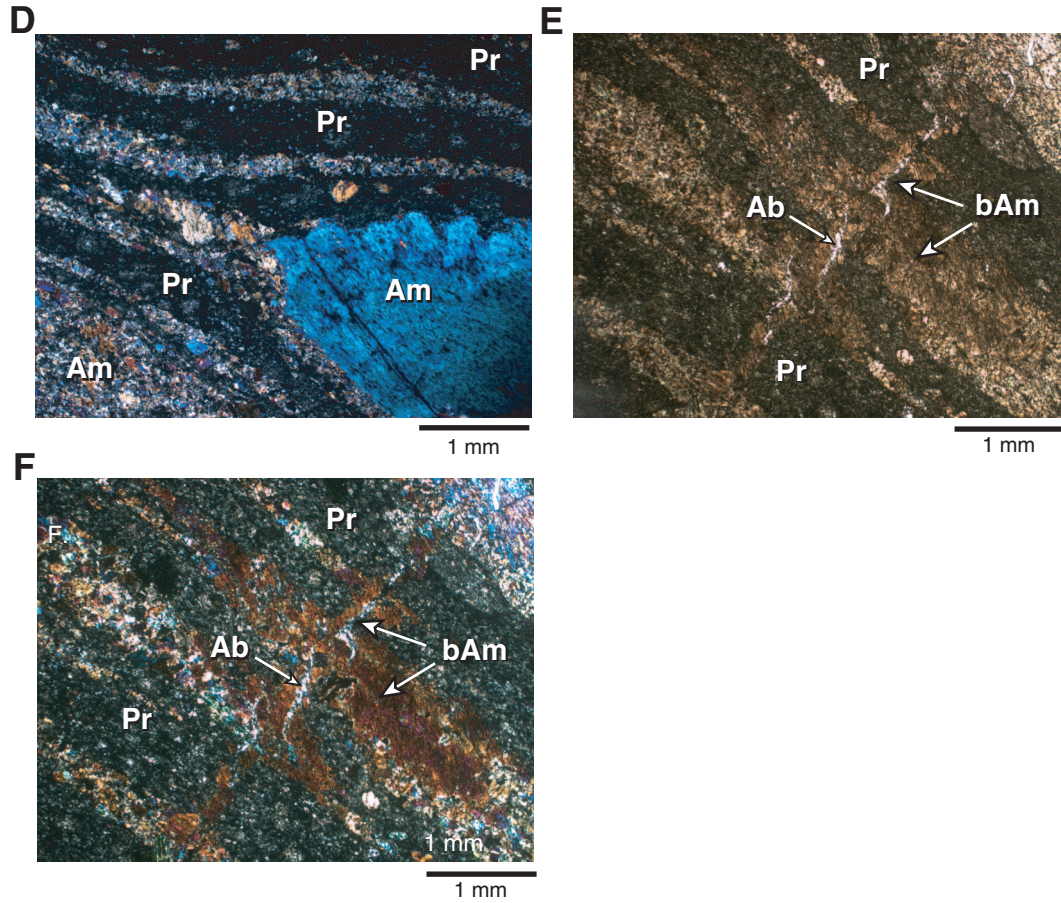
Figure F42. Photomicrographs of porphyroclastic gabbro mylonite entirely pseudomorphed by near-static secondary amphibole (Am). Cross-fiber secondary amphibole replacing clinopyroxene augen, demonstrating near-static replacement of the pyroxene. Slight inclination of the amphibole fibers to the foliation plane suggests continued postalteration deformation (Sample **209-1271B-14R-1 [Piece 7, 32–35 cm]**). **A.** Plane-polarized light: blue filter; field of view = 5.5 mm; image 1271B_115. **B.** Cross-polarized light: blue filter; field of view = 5.5 mm; image 1271B_116.
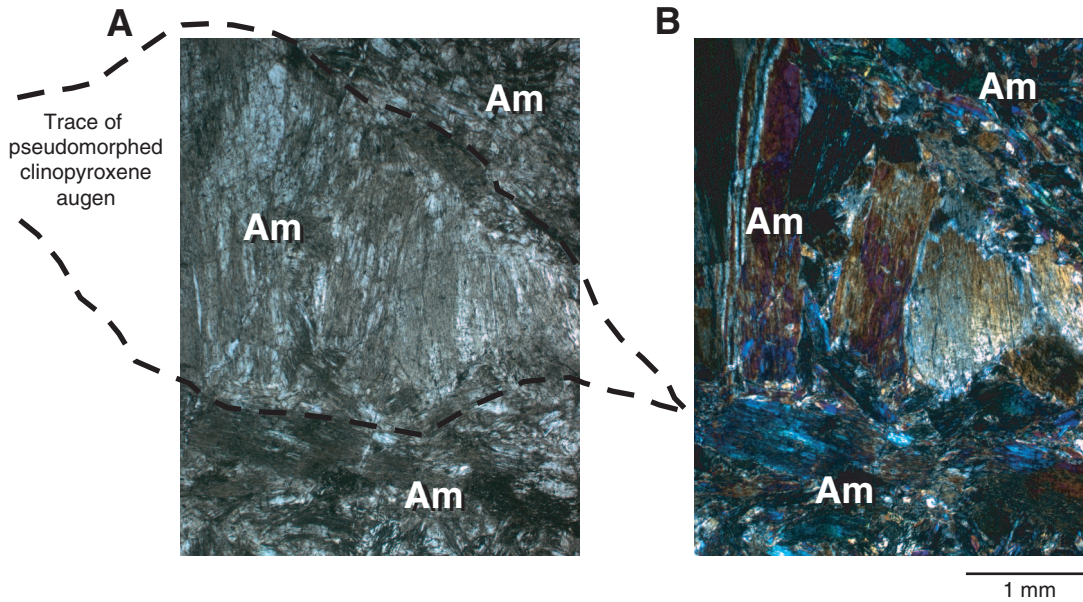
Figure F43. Photomicrographs illustrating late brittle-ductile deformation and faulting in troctolitic gabbros and dunites. **A.** Amphibolite replacing troctolite(?) showing a large amphibole crystal that has been sheared to form numerous parallel subgrains (Am_1), separated from a patch of secondary amphibole (Am_2) by a late, chloritized microfault (Sample **209-1271B-17R-1 [Piece 3, 17–19 cm]**) (cross-polarized light [XPL]: blue filter; field of view [FOV] = 5.5 mm; image 1271B_121). **B.** Microfault along which a coarse-grained amphibole has been sheared (upper left), with the development of a secondary fibrous amphibole-talc-chlorite (Tc – Am_2 – Chl) assemblage in the shear zone (lower right) (Sample **209-1271B-17R-1, 17–19 cm**) (XPL: blue filter; FOV = 5.5 mm; image 1271B_120). **C.** Fully developed secondary fibrous amphibole (Am_2)-talc (Tc)-chlorite (chl) assemblage on a late shear zone (Sample **209-1271B-17R-1, 17–19 cm**) (XPL: blue filter; FOV = 2.75 mm; image 1271_119). **D.** Amphibole (Am) veined dunite showing a sheared secondary amphibole vein that crosscuts earlier secondary amphibole (Sample **209-1271B-18R-1 [Piece 20, 114–117 cm]**) (XPL; FOV = 5.5 mm; image 1271B_128).
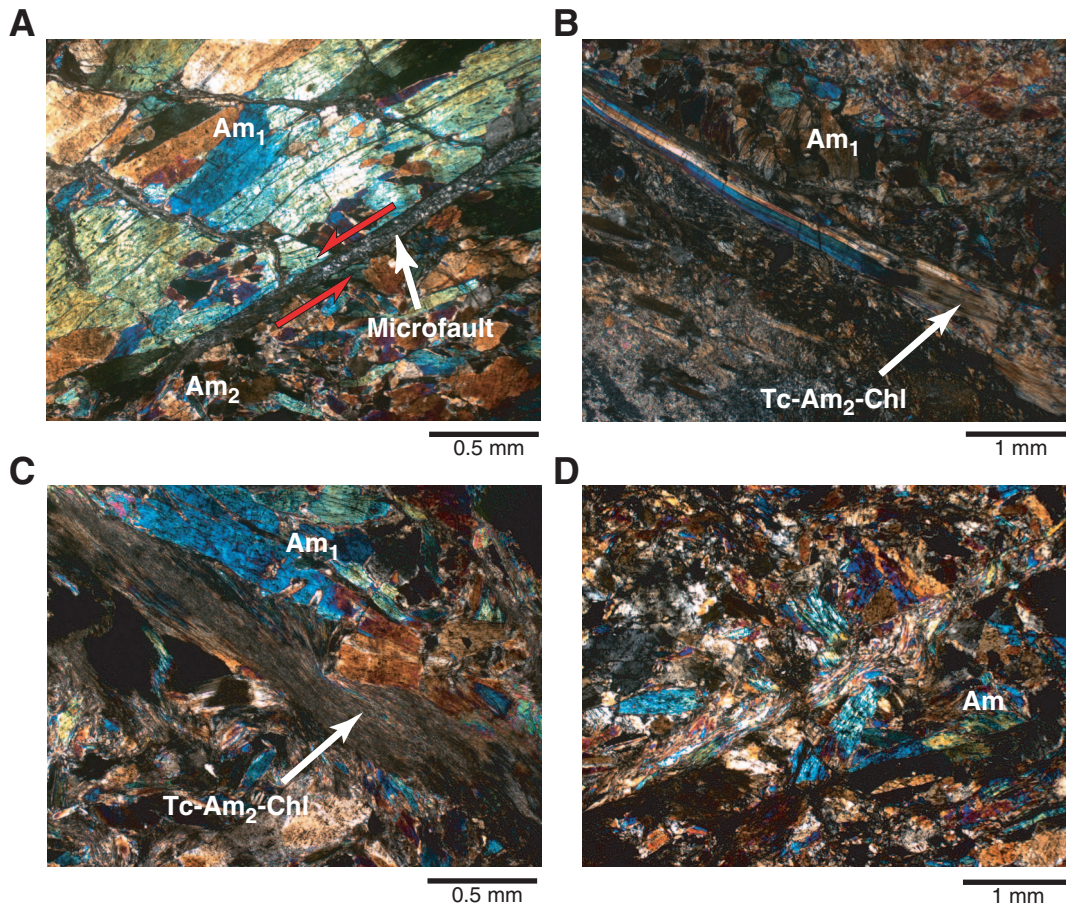
Figure F44. Close-ups of digital images showing impregnation textures from Hole 1271A resembling experimentally produced, partially molten mixtures of olivine and basalt. **A.** Sample 209-1271A-3R-1 (Piece 7). **B.** Sample 209-1271A-4R-1 (Piece 8). **C.** Sample 209-1271A-4R-1 (Piece 14). **D.** This image shows earlier impregnation textures being cut by later, more veinlike intrusions (indicated by the arrow) (Sample 209-1271A-4R-1 [Piece 12]).
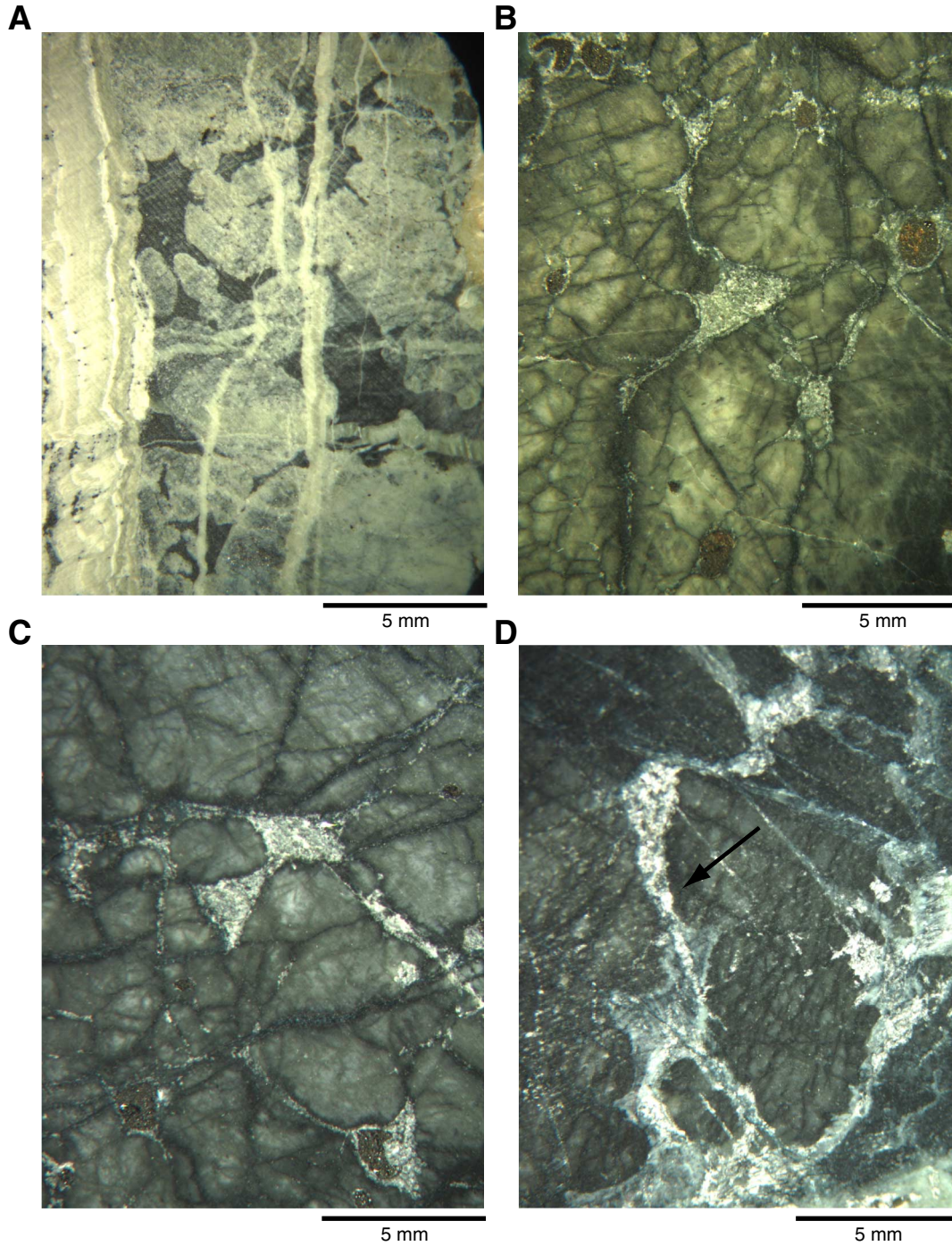
Figure F45. Close-up image of a pyroxenite vein in dunite that is cut by a late gabbroic vein. The arrows indicate impregnating gabbroic material (interval 209-1271B-11R-1, 110–114 cm).
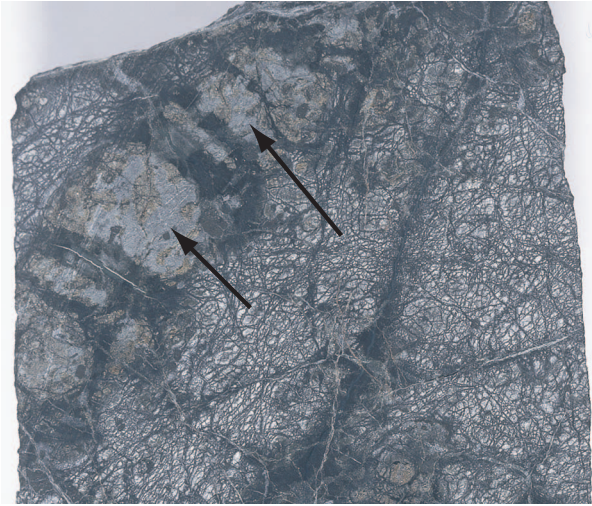
2 cm

Figure F46. Close-up of digital image showing texture from a horizon with a high volume fraction interstitial gabbroic material in Hole 1271B. In this horizon most grains are separated by interstitial gabbroic material. Some olivine grains are rounded, while other olivine crystals resemble angular fragments (lower arrow). The upper arrows point to an arch of aligned olivine possibly rotated in to a common orientation by horizontal flow of melt (Section 209-1271B-12R-1 [Piece 10]).
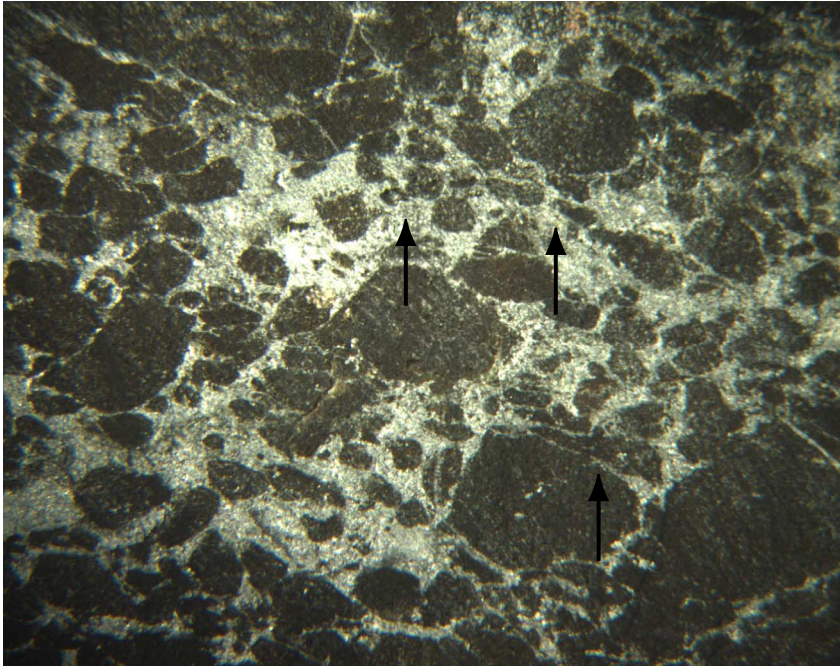
5 mm

Figure F47. Close-up photograph of dunite with a high volume fraction of impregnated material crosscut by a later gabbroic vein (interval 209-1271B-12R-1, 42–55 cm).
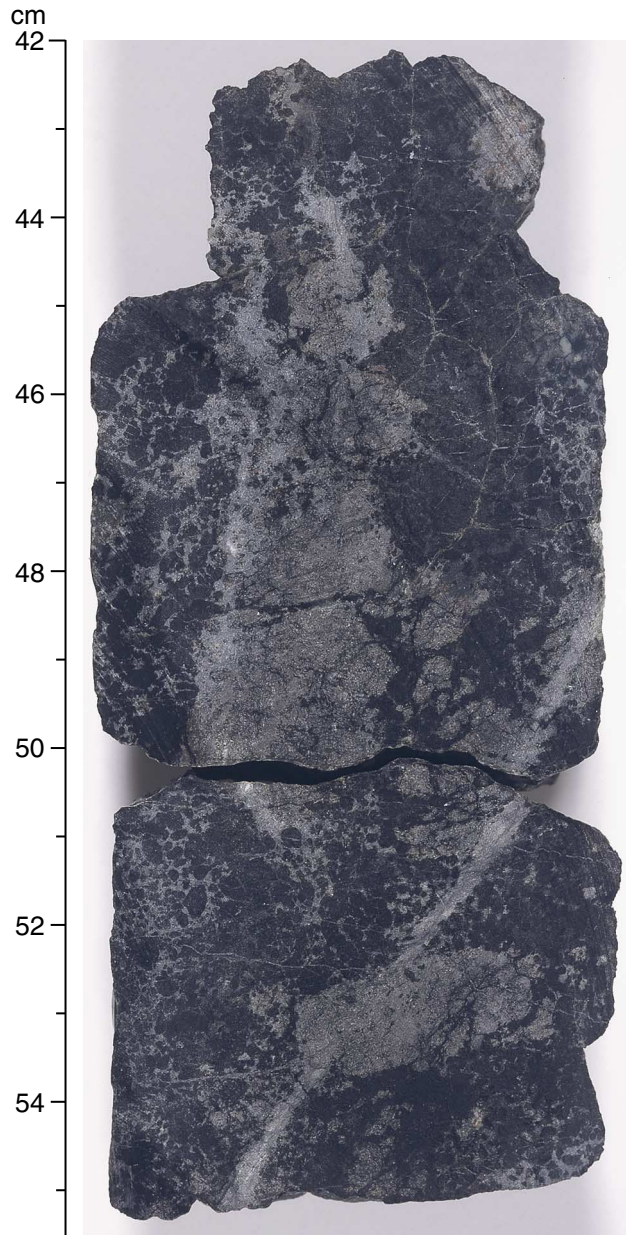
Figure F48. Photographs showing textures from the lower impregnation horizon in Hole 1271B. These textures resemble textures in experiments on partially molten mixtures of olivine plus basalt. **A.** Close-up photograph of a large olivine crystal surrounded by impregnating material that contains rounded spinel grains (interval 209-1271B-19R1, 125–130 cm). **B.** Close-up photograph of interstitial impregnation textures and patchy, veinlike impregnation textures, indicating that multiple liquids of differing composition impregnated this dunite (interval 209-1271B-19R-1, 10–16.5 cm).

A
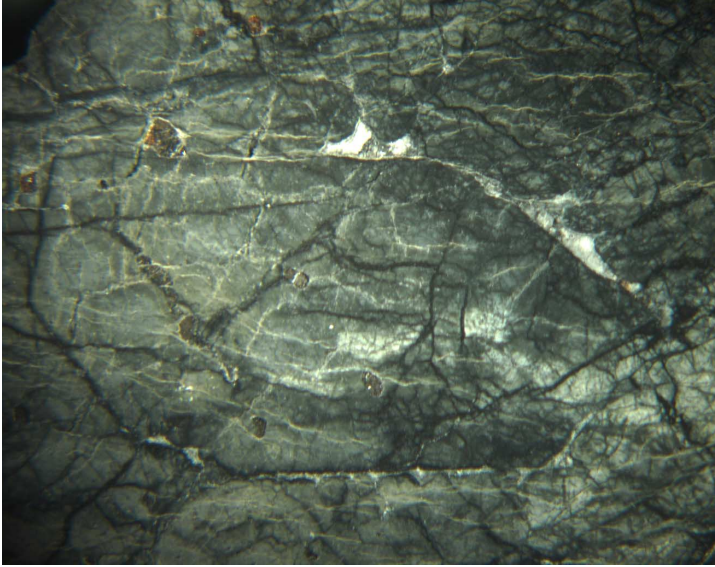
B

Figure F49. Examples of alteration veins cutting dunites in core sections from Holes 1271A and 1271B. **A.** Green picrolite serpentine veins cut by white picrolite serpentine veins and later oxide veins (interval 209-1271A-1R-1, 36–50 cm). **B.** Anastomosing network of black serpentine-magnetite veins cut by a later composite green and black serpentine vein and by late talc-tremolite and carbonate veins (interval 209-1271A-1R-1, 51–66 cm). **C.** Anastomosing network of black serpentine magnetite veins cut by green picrolite serpentine veins and later white chrysotile veins (interval 209-1271A-1R-2, 94–109 cm). **D.** Anastomosing network of black serpentine magnetite veins cut by a composite green and back serpentine vein that is offset by a fault filled with carbonate/tremolite (interval 209-1271B-7R-1, 24–31 cm). **E.** Anastomosing network of black serpentine/magnetite veins that has been faulted. Later green picrolite serpentine veins and even later carbonate veins exploit the fault as a conduit (interval 209-1271B-2R-1, 4–10 cm).
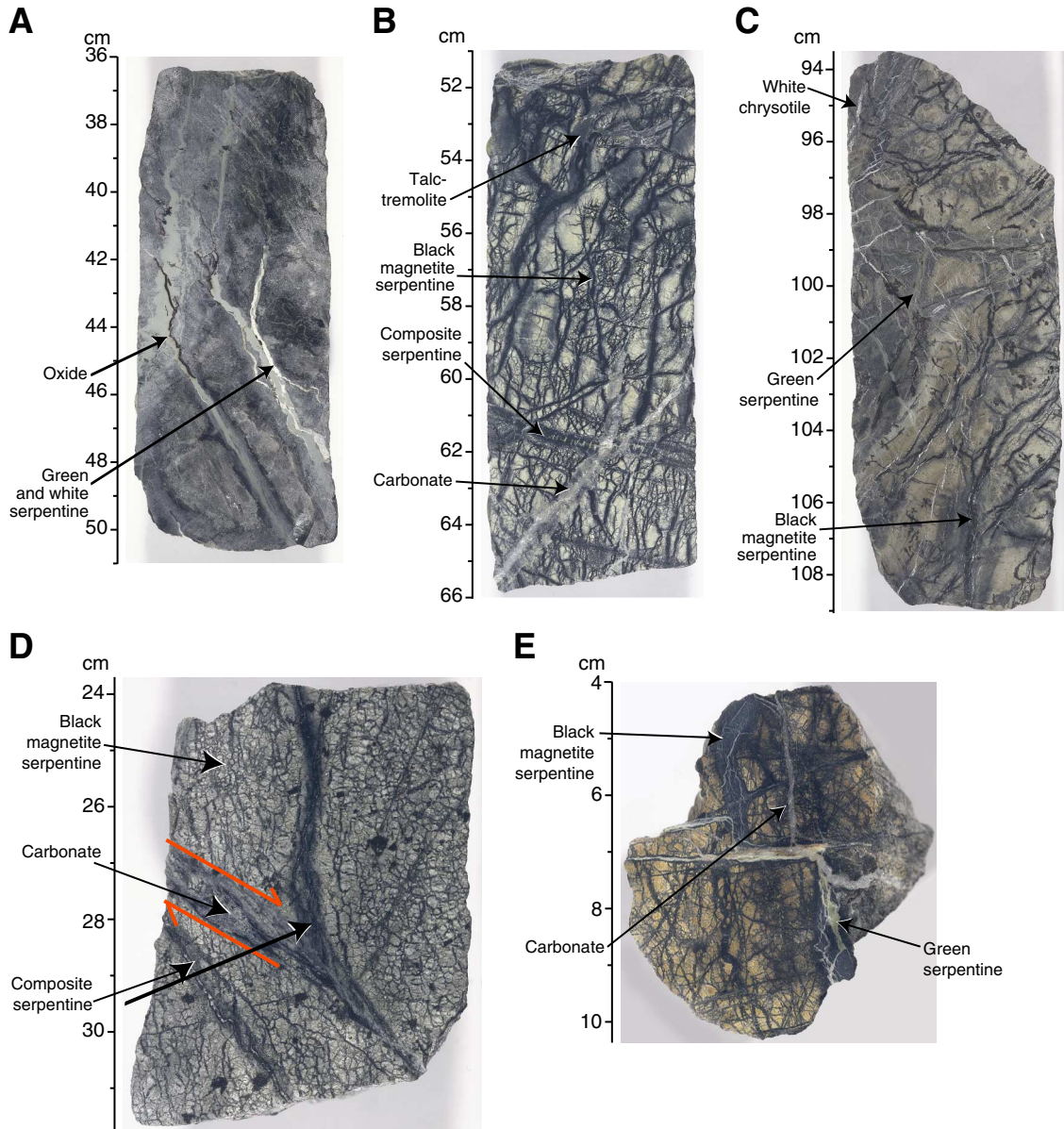
Figure F50. Photomicrograph of fine-grained amphibole and serpentine schist. Intermediate-grained, pale brown amphibole in the lower right corner of the photo is aligned parallel to the crystal-plastic foliation in the olivine mylonite. Fine-grained, schistose, colorless amphibole in the upper left corner appears to have formed concurrently with schistose serpentine in the center of the photo during late greenschist facies deformation and alteration of a gabbroic vein (Sample **209-1271B-11R-1, 88–91 cm**) (cross-polarized light: blue filter; field of view = 2.75 mm; image 1271B_103).
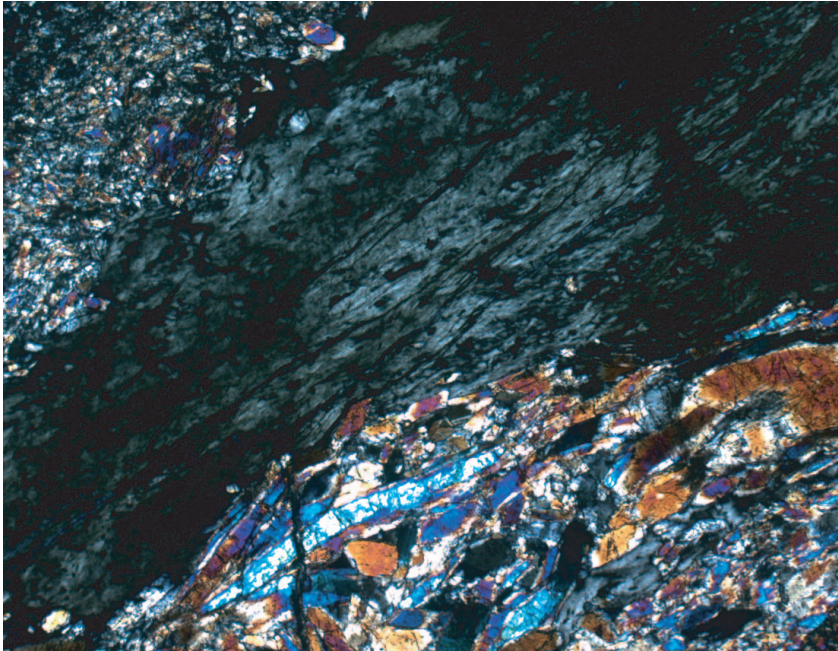
Figure F51. Close-up photograph of a low-temperature schist from the upper deformed section of Hole 1271B. The foliation is defined by schistose chlorite and serpentine due to intense greenschist and subgreenschist grade alteration (interval 209-1271B-3R-1, 17–22 cm).

Figure F52. Photomicrograph of serpentine-chlorite schist from a semibrittle shear zone. Fibrous chlorite defines the strong planar to slightly anastomosing foliation. An early generation of fibrous chlorite (top of image) is folded as a consequence of later deformation (Sample **209-1271B-11R-1, 55–57 cm**) (plane-polarized light: blue filter; field of view = 5.5 mm; image 1271B_101).

Figure F53. Photomicrograph of cohesive carbonate-matrix fault breccia. Variable-sized clasts of serpentinite are contained in a fine carbonate matrix. Sheared, fibrous carbonate bands in the matrix indicate a tectonic origin for the breccia (Sample 209-1271B-3R-1, 51–54 cm) (plane-polarized light: blue filter; field of view = 2.75 mm; image 1271B_105).

Figure F54. Downhole plot of brittle deformation and alteration vein intensities in Hole 1271A. Expanded depth of cored interval is plotted on the vertical axis. Yellow cones reflect the depth range of expansion for each core. Intensity estimate is based on visual core description of individual core pieces. Intensities are plotted as a running downhole average of seven pieces, weighted by piece length, at each depth (96 pieces total). TD = total depth.
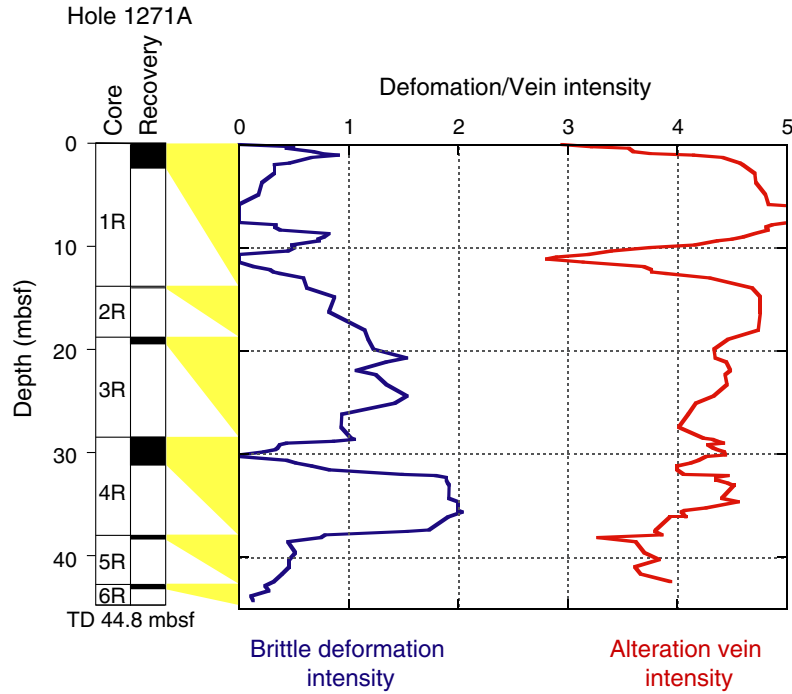
Figure F55. Downhole plot of brittle deformation and alteration vein intensities in Hole 1271B. Expanded depth of cored interval is plotted on the vertical axis. Yellow cones reflect the depth range of expansion for each core. Intensity estimate is based on visual core description of individual core pieces. Intensities are plotted as a running downhole average of seven pieces, weighted by piece length, at each depth (314 pieces total). TD = total depth.
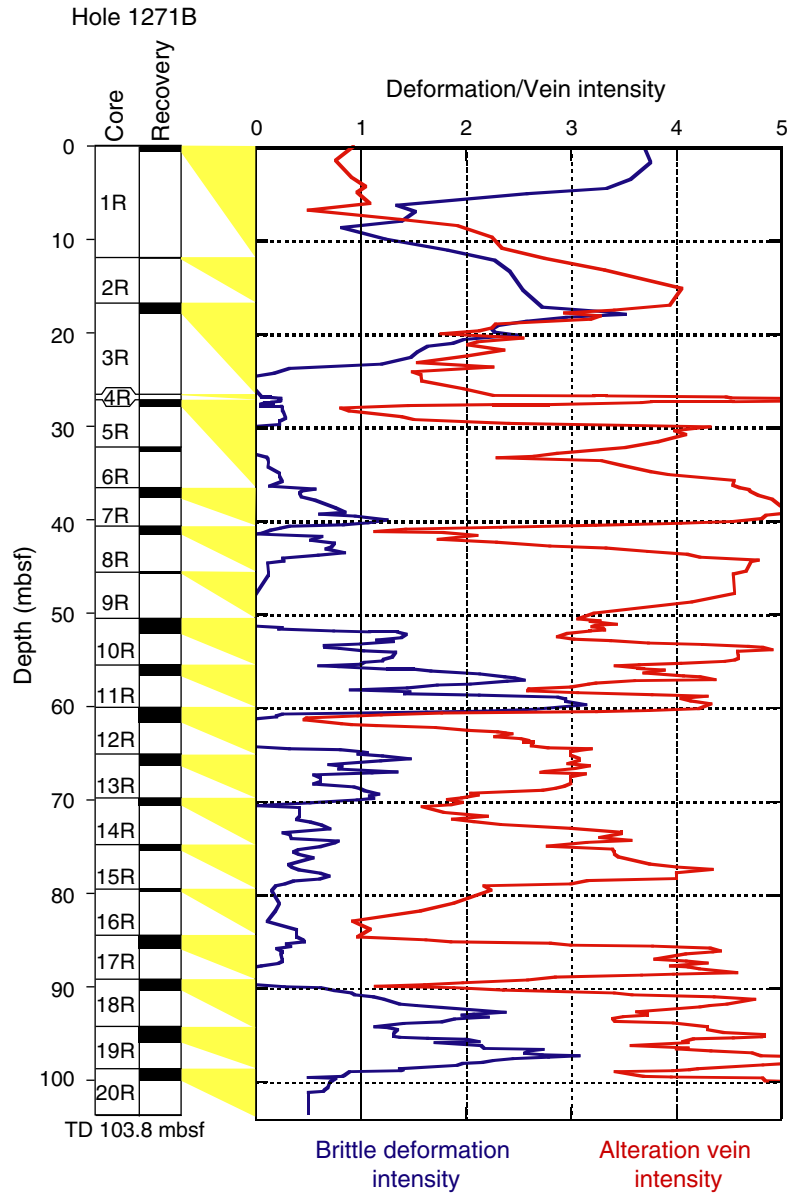
Figure F56. Dips of black serpentine-magnetite, composite green and black serpentine, and carbonate veins with expanded depth in the core reference frame for Holes 1271A and 1271B. TD = total depth.
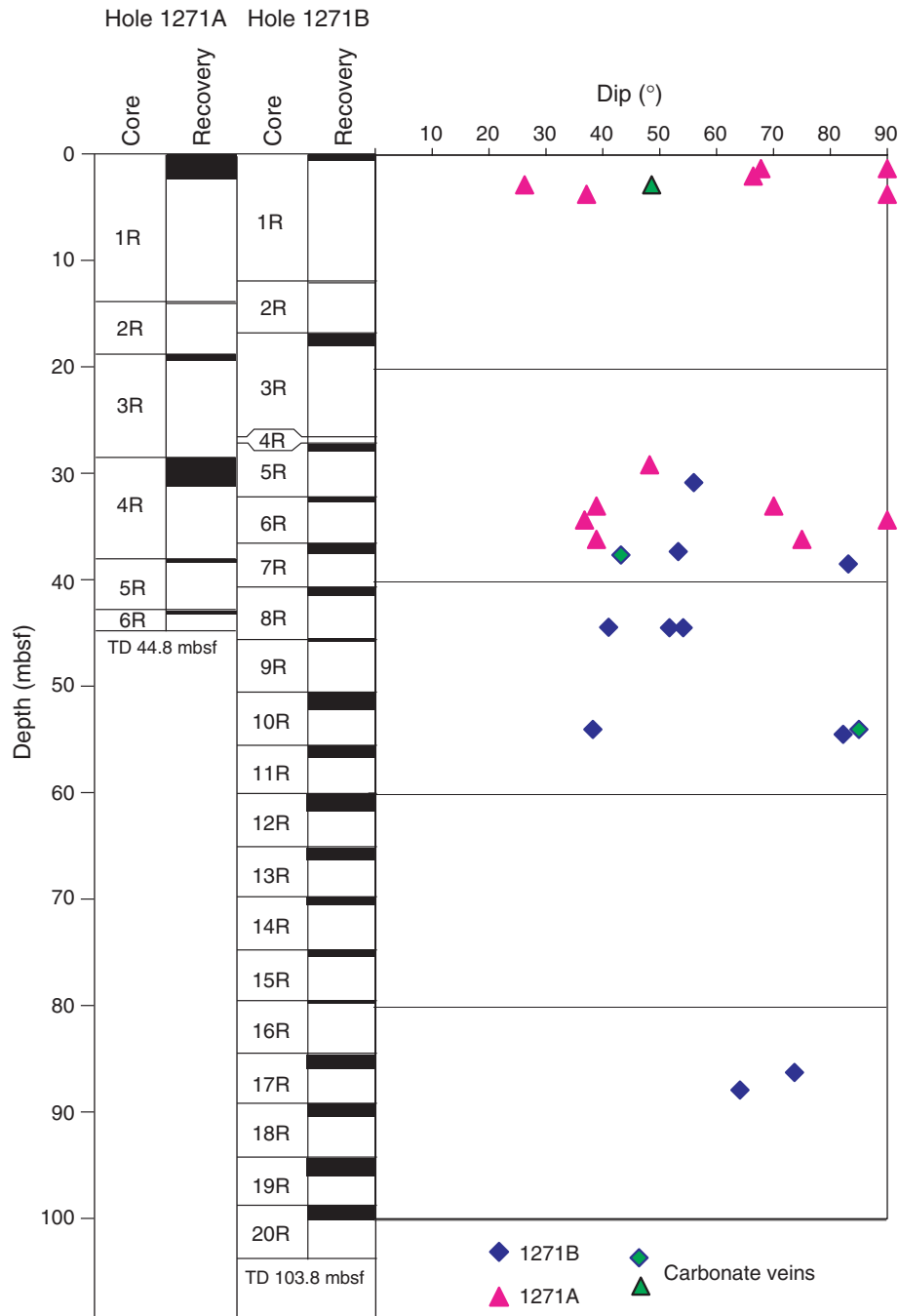
Figure F57. Lower hemisphere equal-area stereographic projection of poles to black serpentine-magnetite and composite green/black serpentine veins and brittle shear zones in Holes 1271A and 1271B. Measurements were rotated into a common orientation using the measured paleomagnetic azimuth as described in **"Structures in Peridotite and Gabbroic Intrusions,"** p. 8, in "Mantle Upwelling, Melt Transport, and Igneous Crustal Accretion" in the "Leg 209 Summary" chapter.

Paleomagnetic North

Lower hemisphere, equal area

• 1271A alteration veins (N = 12)

□ 1271B alteration veins (N = 12)

◇ 1271A and 1271B brittle features (N = 9)
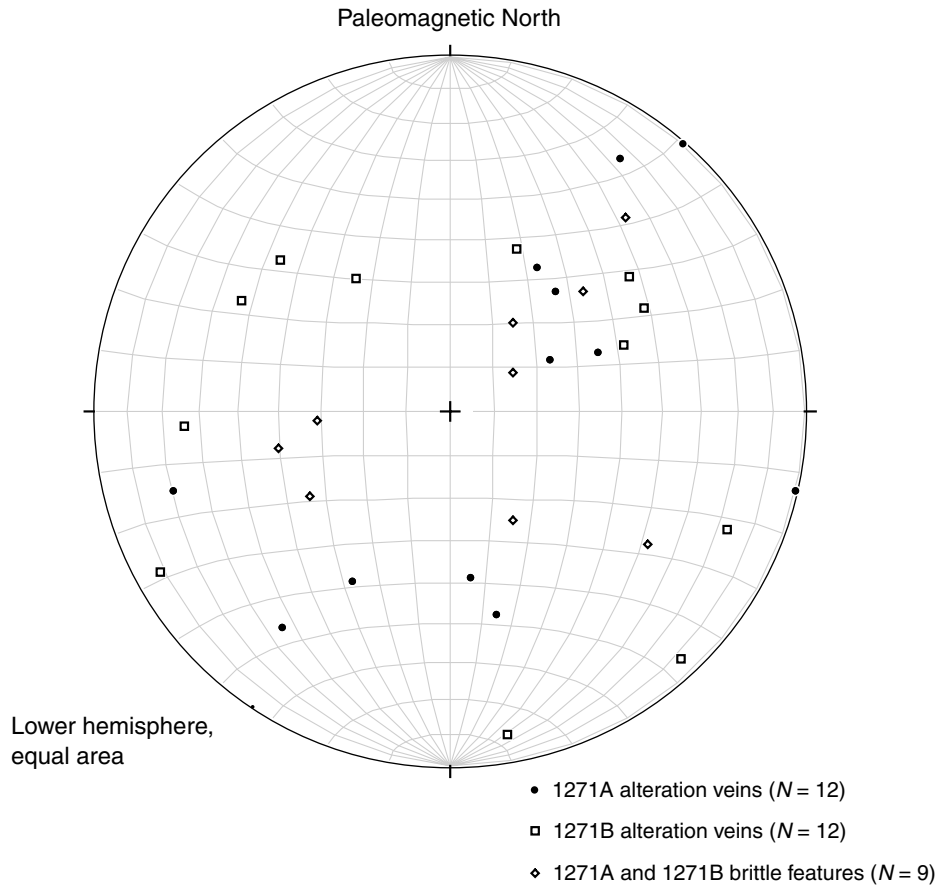
Figure F58. LOI, SiO_2, and Al_2O_3 vs. MgO for peridotites from Site 1271. Shown for comparison are end-member compositions of lizardite and talc (Deer et al., 1992), Site 920 serpentinites (Dilek et al., 1997), and peridotites from Sites 1268 and 1270.
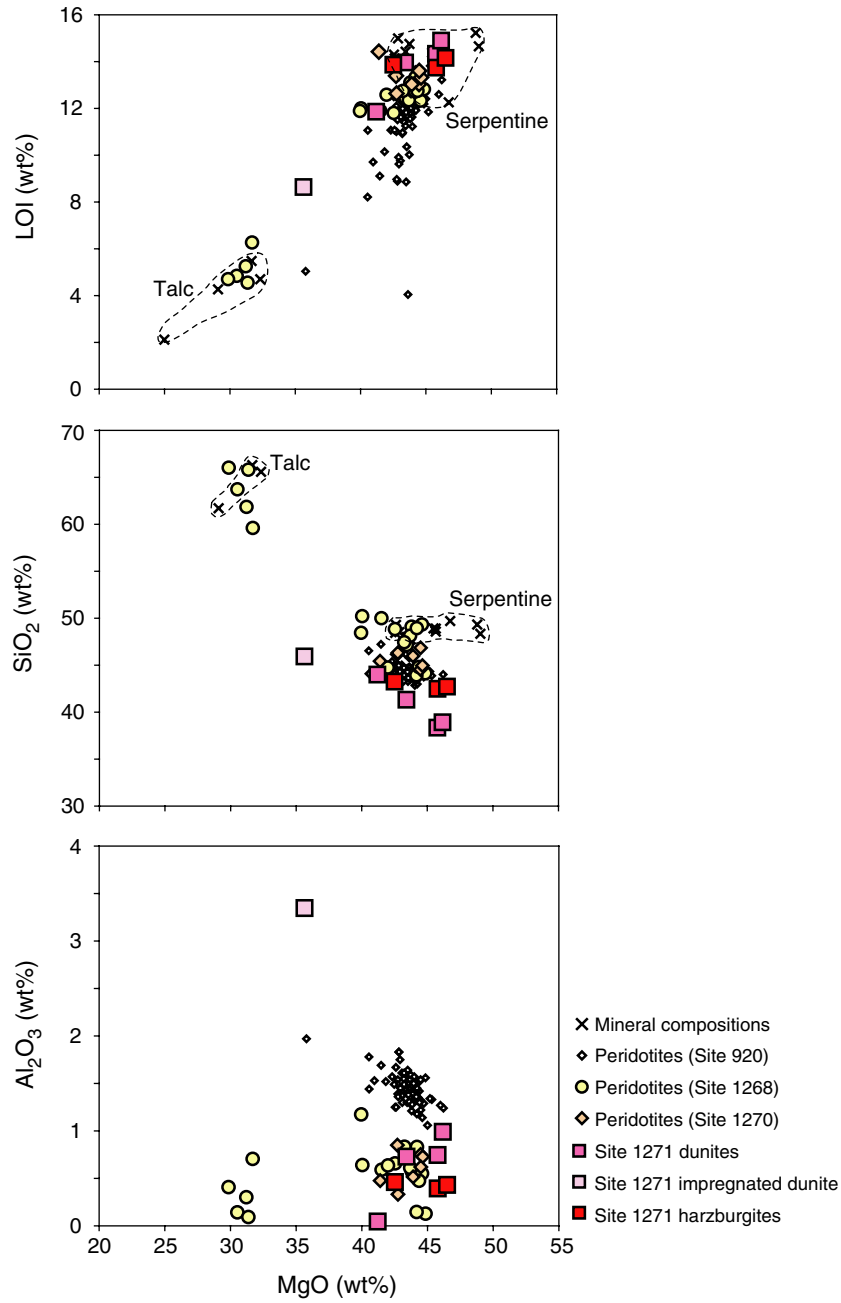
Figure F59. FeO vs. MgO whole-rock concentrations in Site 1271 peridotites. Published data are also shown for comparison: open diamonds = Mid-Atlantic Ridge peridotites from Leg 109, Site 670 (Hebert at al., 1990) and Leg 153 Site 920 (Casey, 1997). Other symbols are: * = Southwest Indian Ridge (Snow and Dick, 1995), + = Izu-Bonin-Mariana forearc (Parkinson and Pearce, 1998), gray diamond = East Pacific Rise peridotites (Niu and Hekinian, 1997), × = Western Alps orogenic lherzolites and ophiolites (Bodinier, 1988; Rampone et al., 1996), gray circle = Oman ophiolite harzburgites (Godard et al., 2000), gray triangle = Oman ophiolite mantle transition zone dunites (Godard et al., 2000). Whole-rock compositions are presented on a volatile-free basis assuming all Fe is FeO. The solid black lines show olivine and orthopyroxene composition as a function of Fe/Mg. Fine gray lines show constant Mg# values (Mg# = $100 \times Mg/[Mg + Fe_{total}]$). Fe_{total} = total Fe as FeO.
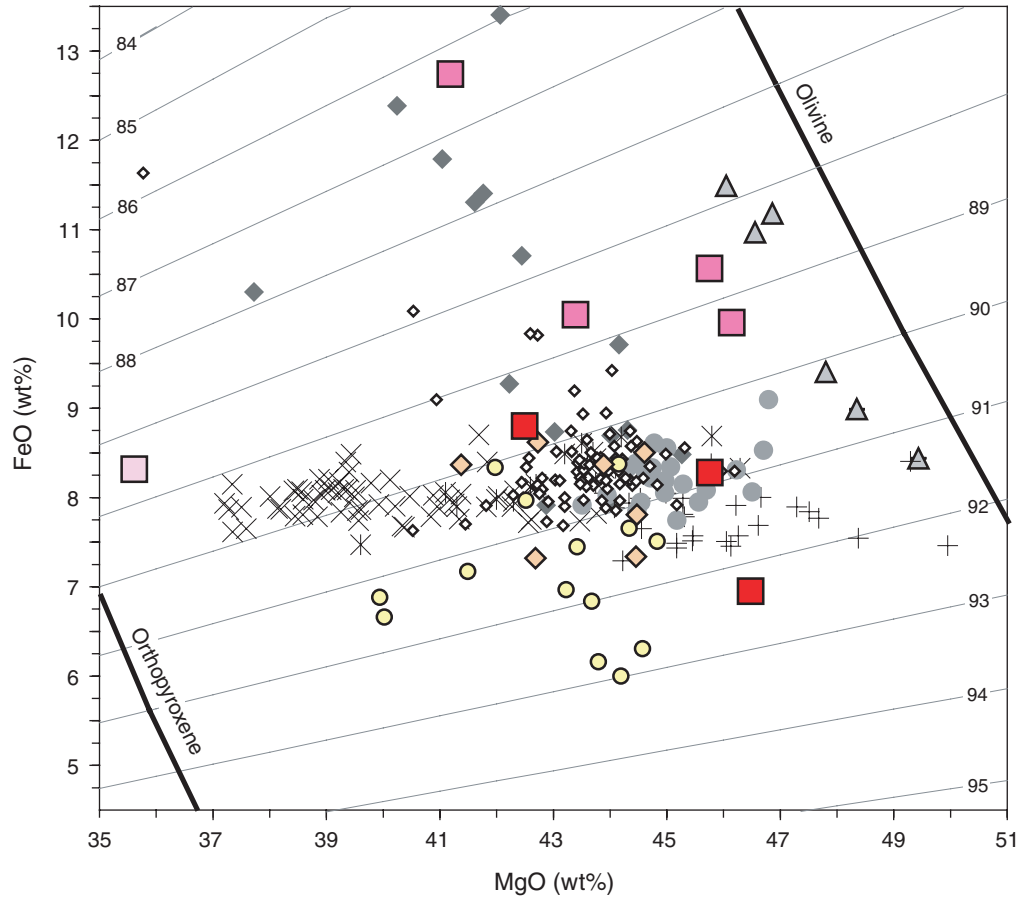
Figure F60. V and Cr vs. Al$_2$O$_3$ in peridotites from Site 1271. Shown for comparison are Site 920 peridotites from Casey (1997) and Site 1268 and 1270 peridotites.
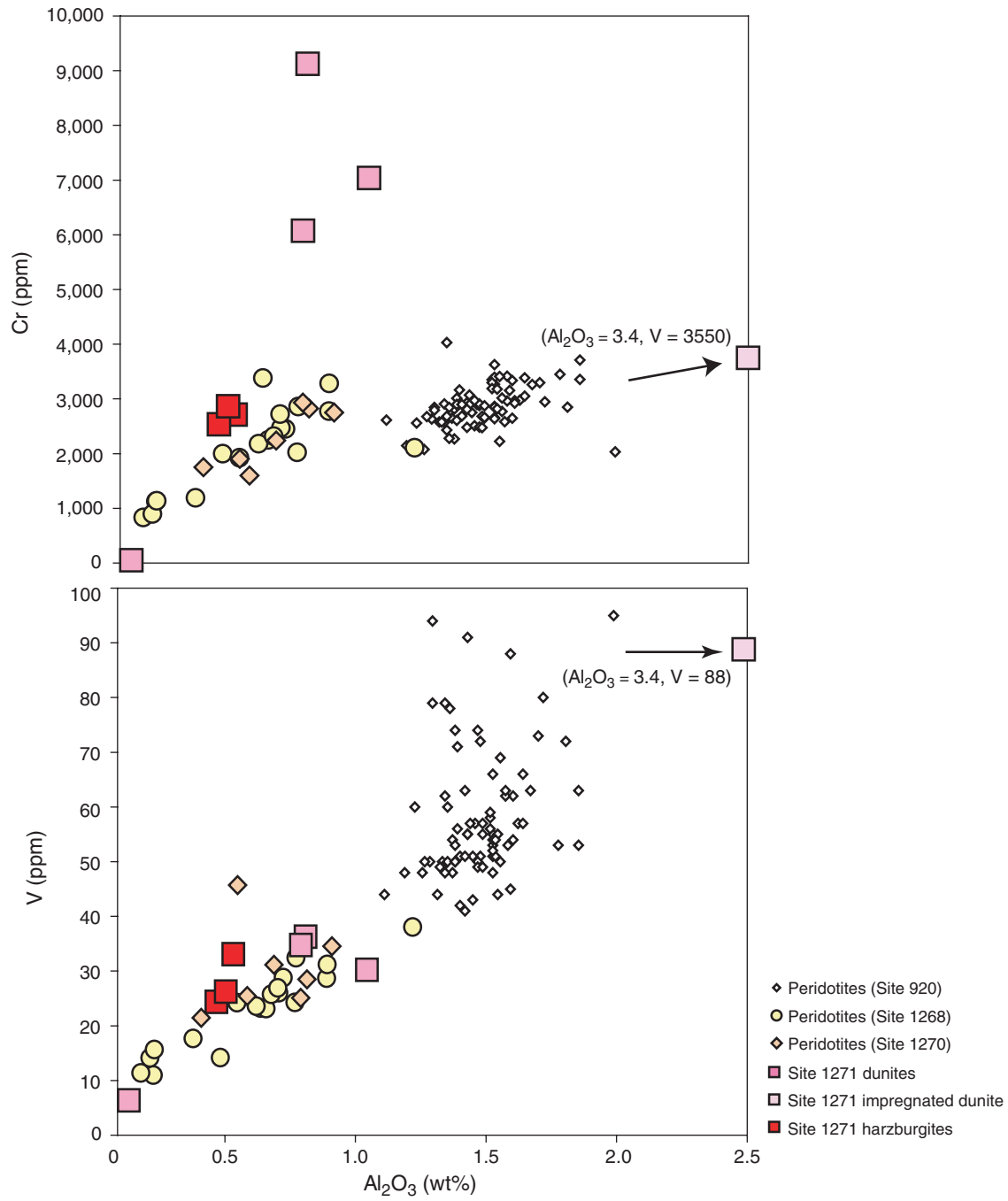
Figure F61. TiO$_2$, Sc, and Zr vs. Al$_2$O$_3$ in peridotites from Site 1271. Shown for comparison are Site 920 peridotites from Casey (1997) and Site 1268 and 1270 peridotites. Dashed lines = detection limit (DL) for TiO$_2$, Sc, and Zr.
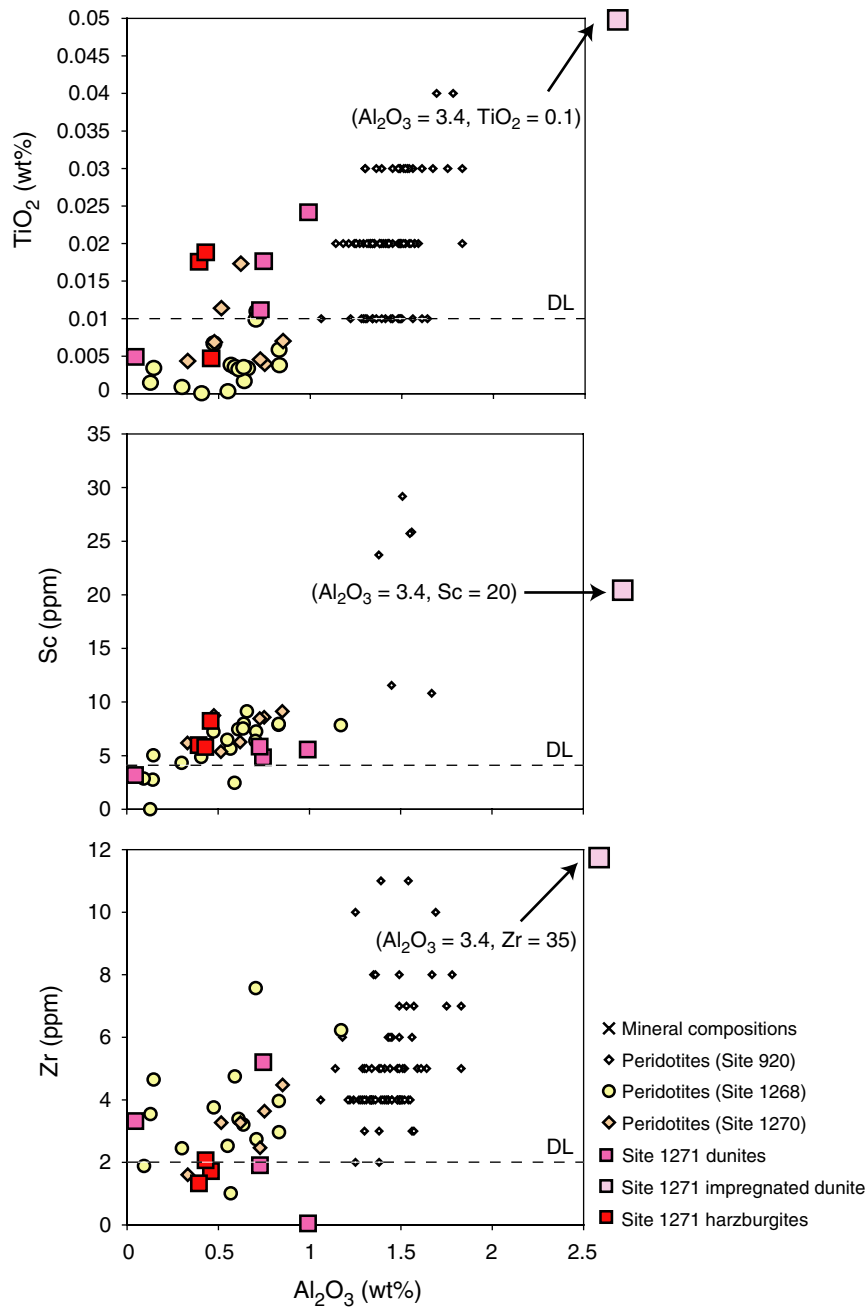
Figure F62. H_2O vs. SiO_2 in gabbros from Site 1271. Site 1268 and 1270 gabbros are shown for comparison.
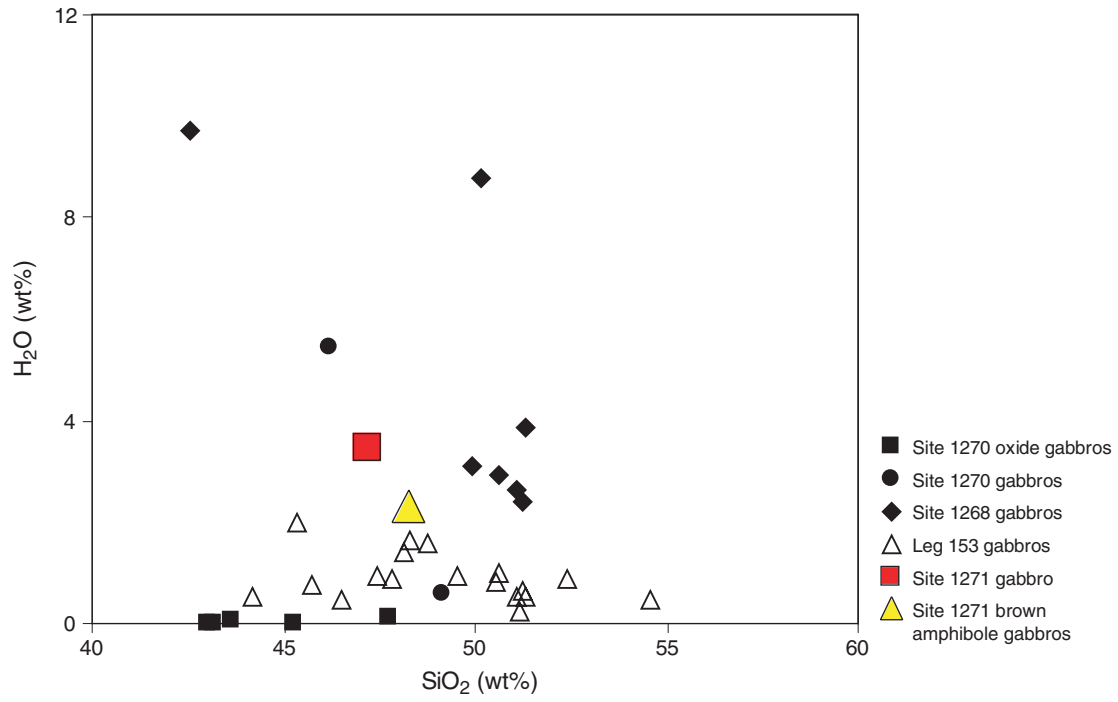
Figure F63. V, Sc, and Cr vs. Al_2O_3 in gabbros from Site 1271. Gabbroic rocks from Leg 153 (from Agar et al., 1997) and Sites 1268 and 1270 are shown for comparison. BAG = brown amphibole gabbro. Dashed line = detection limit (DL) for Cr.
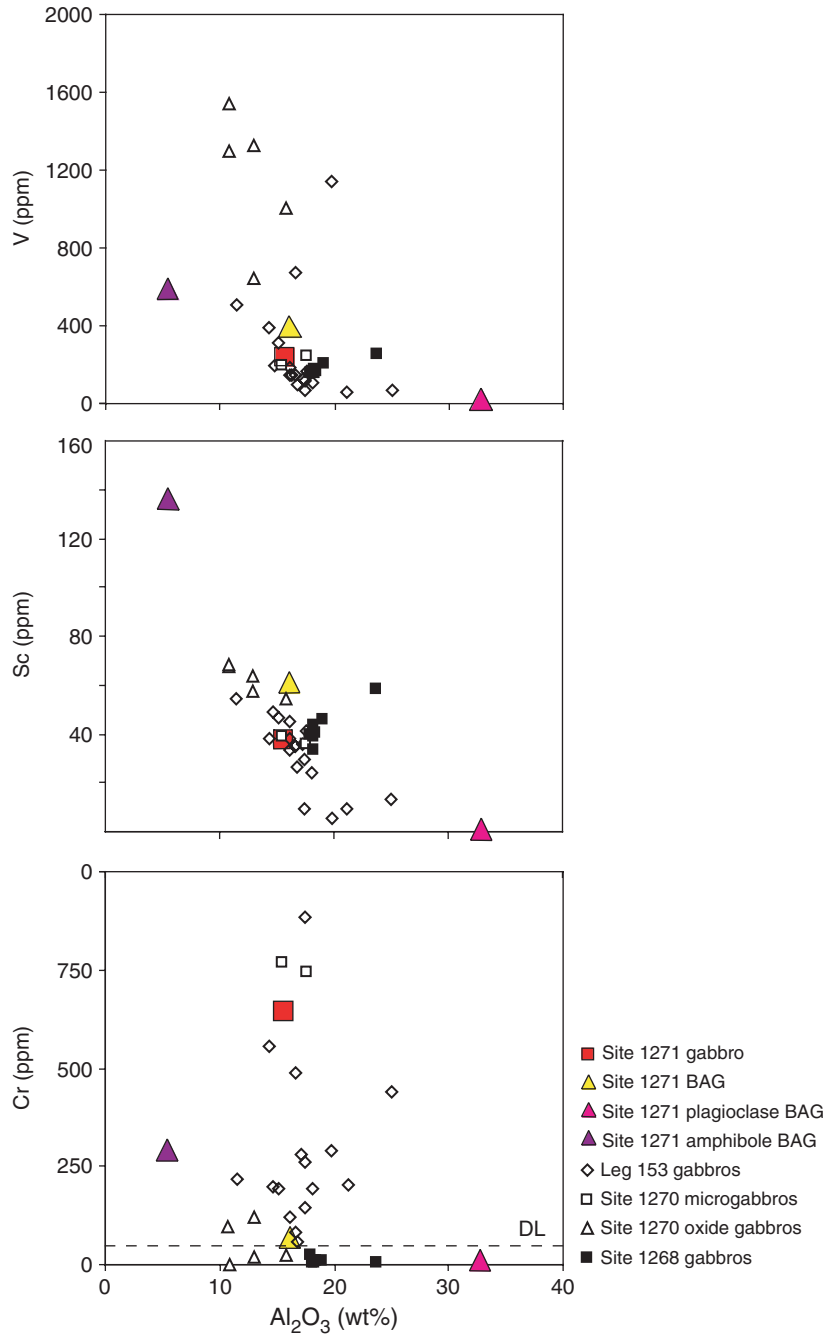
Figure F64. Al_2O_3, TiO_2, and Fe_2O_3 vs. MgO in gabbros from Site 1271. Gabbroic rocks from Leg 153 (from Agar et al., 1997) and Sites 1268 and 1270 are shown for comparison. BAG = brown amphibole gabbro, plag = plagioclase, amph = amphibole.
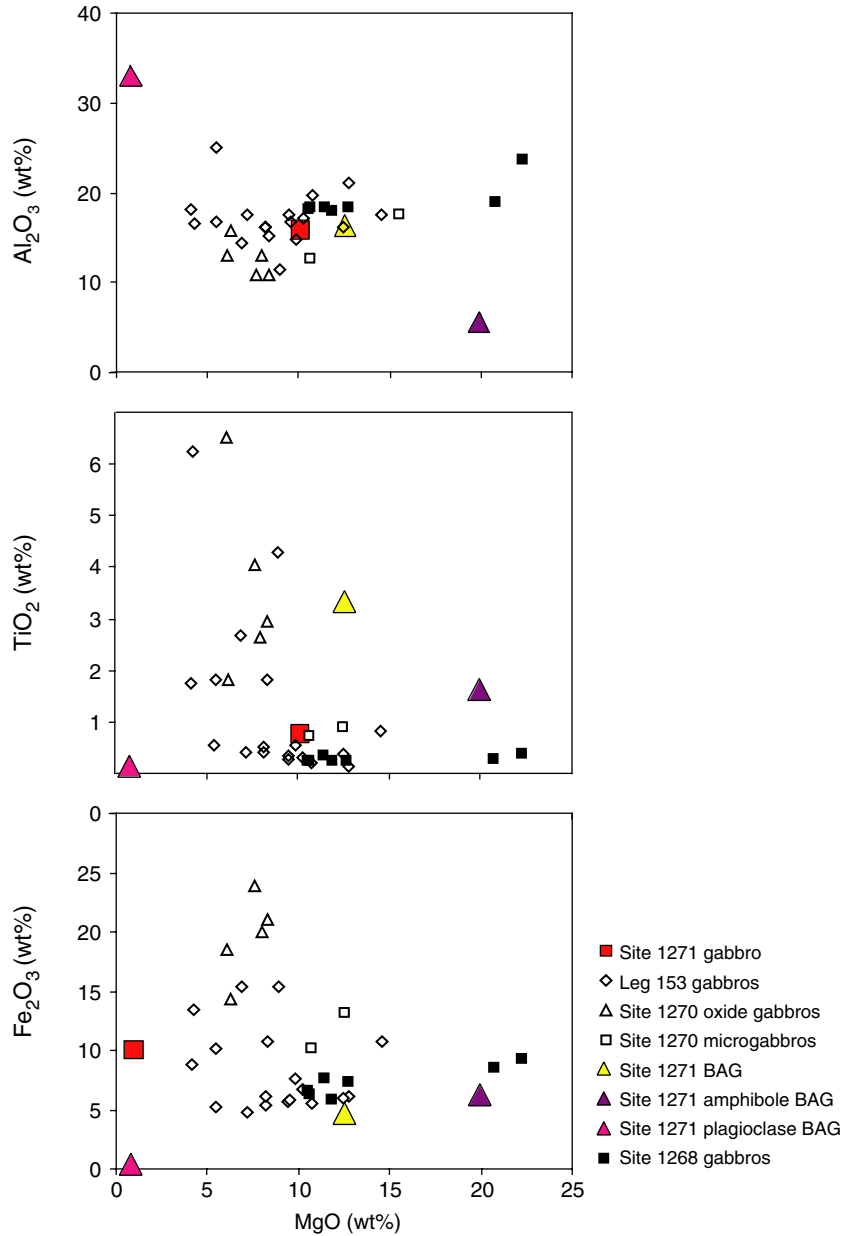
Figure F65. Magnetic susceptibility of cores from Holes 1271A and 1271B, measured on the MST. TD = total depth.
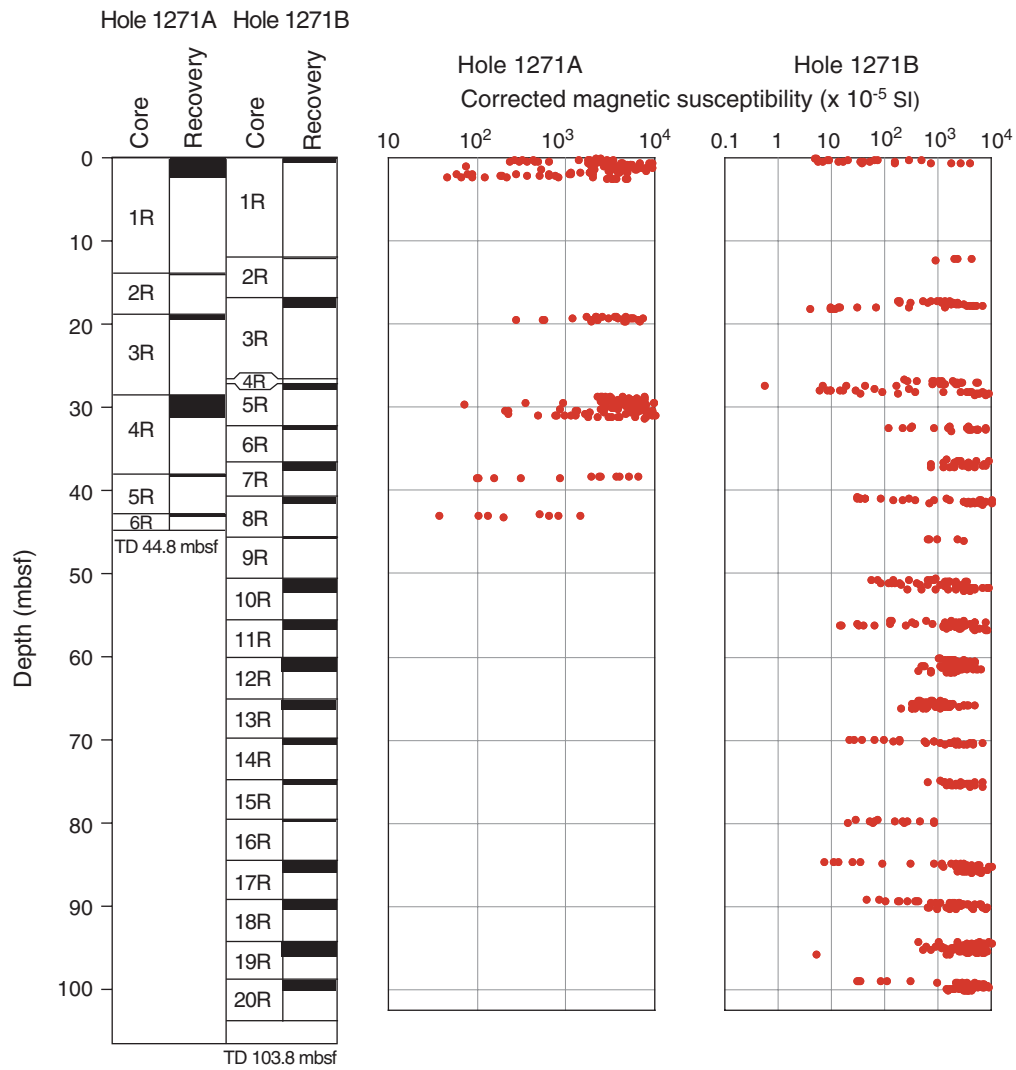
Figure F66. Thermal conductivity of peridotite and troctolite samples from Site 1271, compared with values from Sites 1268 and 1270 and Legs 147 (Gillis, Mével, Allan, et al., 1993) and 153 (Cannat, Karson, Miller, et al., 1995).
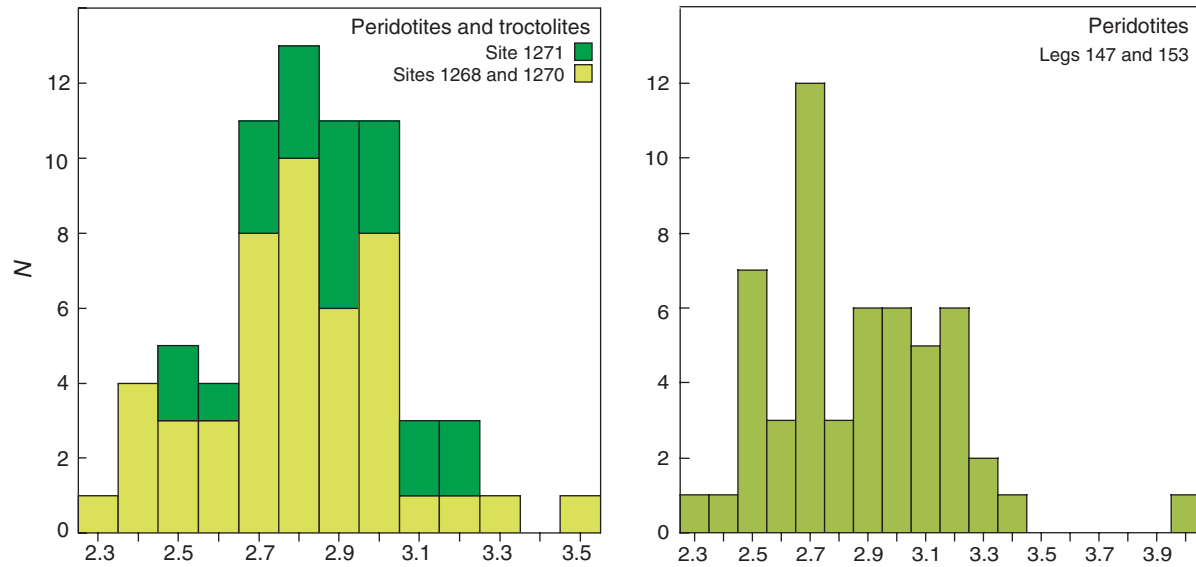
Figure F67. Apparent thermal conductivity anisotropy in peridotite and troctolite samples from Sites 1268, 1270, and 1271.
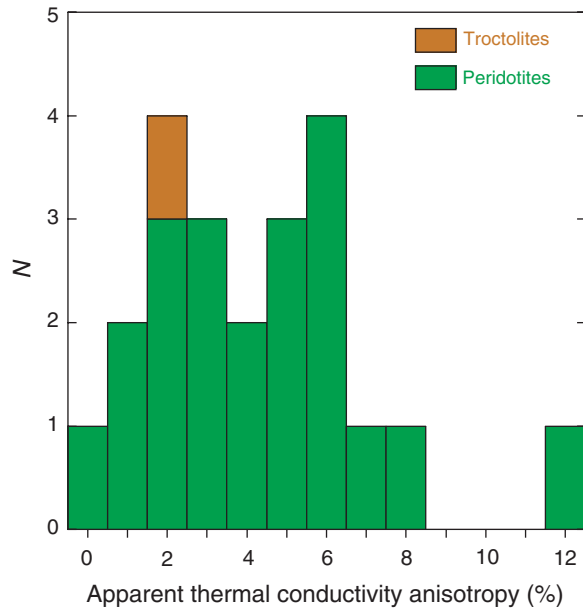
Figure F68. *P*-wave velocity vs. wet bulk density in samples from Site 1271, compared with data from Legs 147 (Gillis, Mével, Allan, et al., 1993; Iturrino et al., 1996) and 153 (Cannat, Karson, Miller, et al., 1995; Miller and Christensen, 1997), as well as Sites 1268 and 1270.
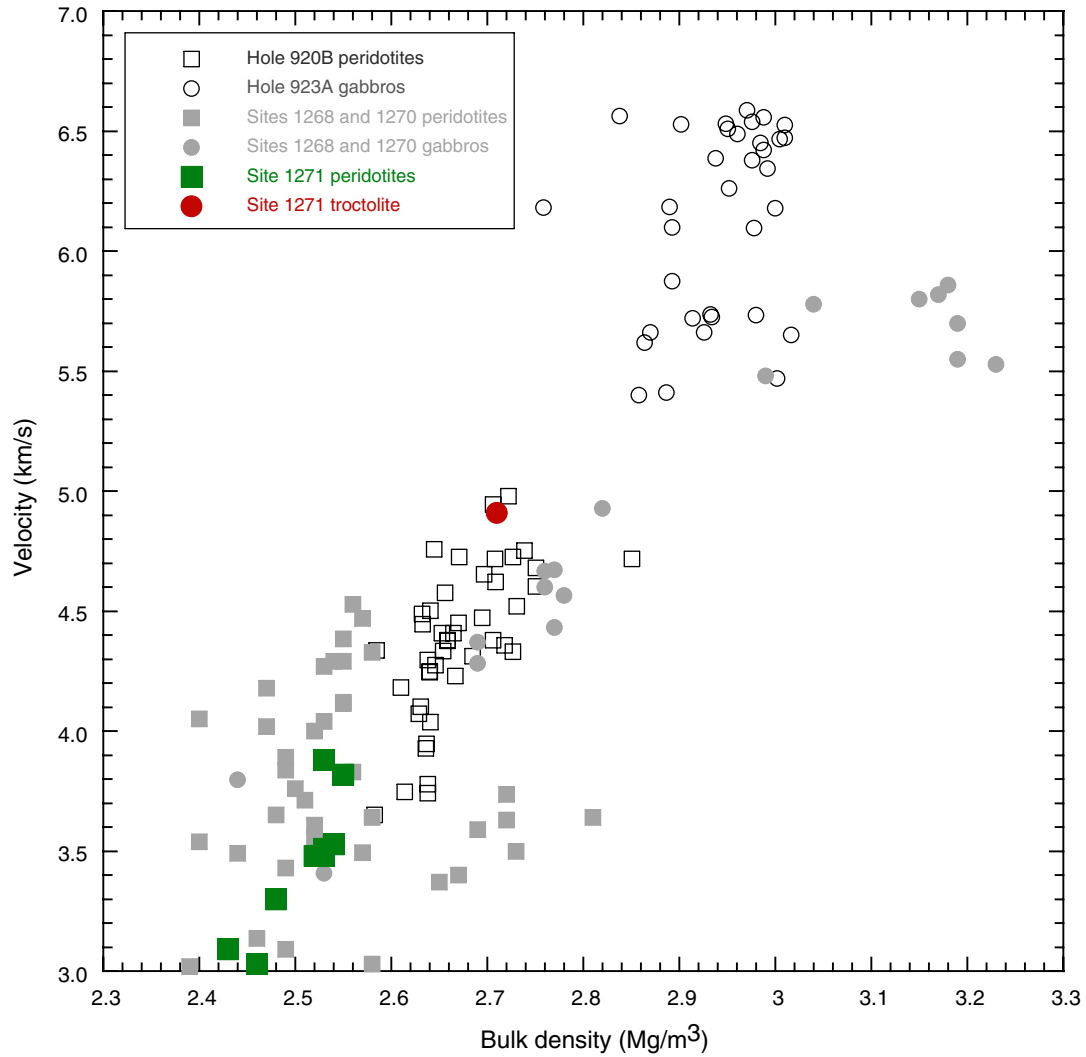
Figure F69. Representative vector endpoint demagnetization diagrams for discrete samples and long-core measurements from Hole 1271A. (**A**) Discrete (Sample 209-1271A-4R-2, 103–105 cm) and (**B**) long-core (Section 209-1271A-4R-2, 104 cm) measurements in the same core interval commonly yield similar final directions but with a significantly different degree of steep, drilling-related overprint. Demagnetization diagrams for (**C**) 9.2-cm^3 cube (Sample 209-1271A-4R-2, 26–28 cm), (**D**) 25-cm^3 quarter-round (Sample 209-1271A-4R-2, 22–25 cm), and (**E**) archive-half (Section 209-1271A-4R-2, 24 cm) data from Section 209-1271A-4R-2 (Piece 1). The quarter-round and archive-half results show steeper initial results and a final direction that is different from the measurement for the discrete sample. NRM = natural remanent magnetization. Solid circles = projections onto the horizontal plane and open circles = projections onto the vertical plane.
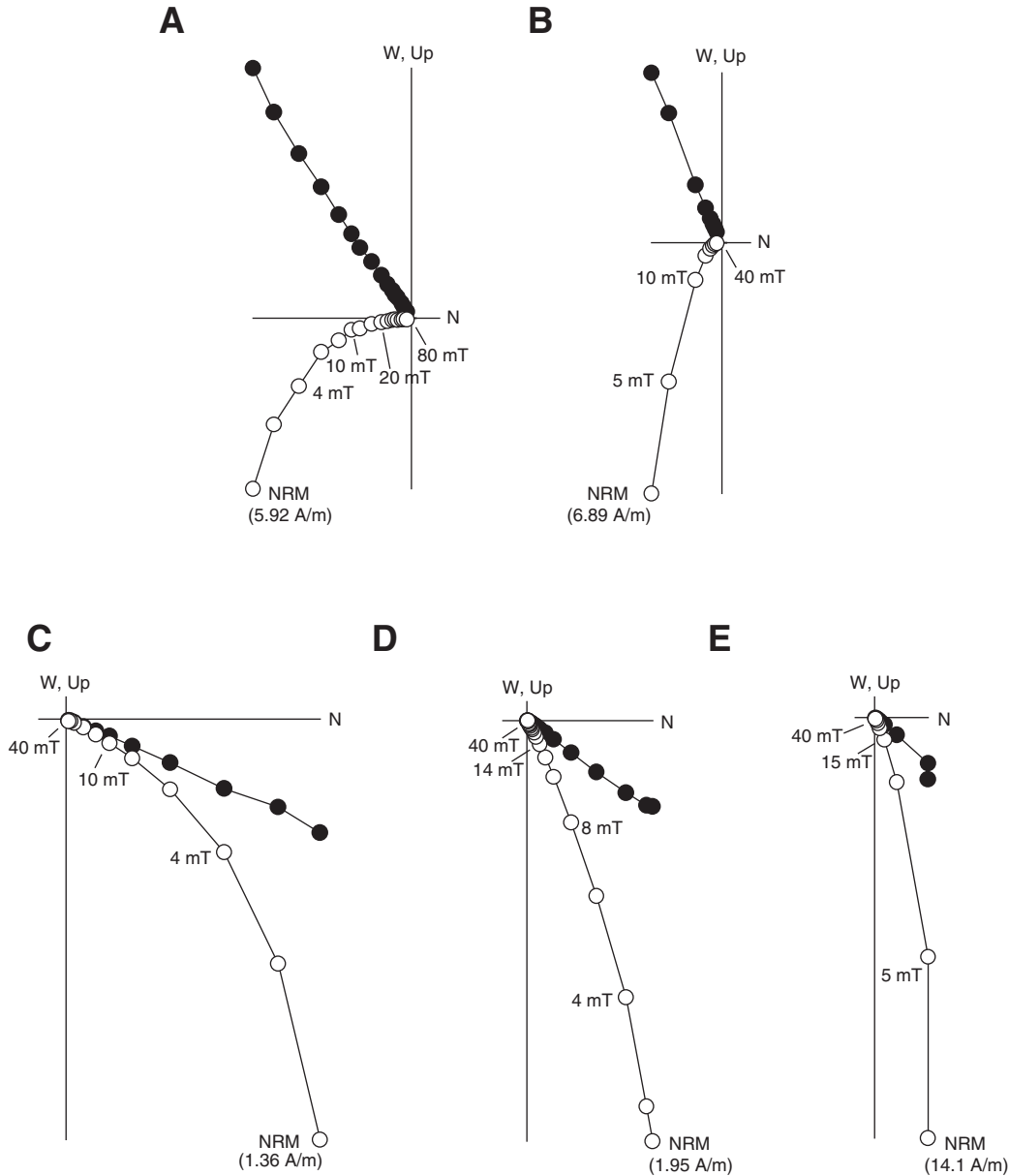
Figure F70. Representative vector endpoint demagnetization diagrams of (A–C) discrete samples at different intervals and (D–F) long-core measurements from the same core pieces from Hole 1271B. Different intensities of drilling overprint affect the samples, but the direction of the characteristic remanence is similar in both discrete and long-core data. **A.** Sample 209-1271B-10R-1, 112–114 cm. **B.** Sample 209-1271B-12R-1, 131–133 cm. **C.** Sample 209-1271B-5R-1, 55–57 cm. **D.** Section 209-1271B-10R-1, 110 cm. **E.** Section 209-1271B-12R-1, 134 cm. **F.** Section 209-1271B-5R-1, 52 cm. NRM = natural remanent magnetization. Solid circles = projections onto the horizontal plane and open circles = projections onto the vertical plane.
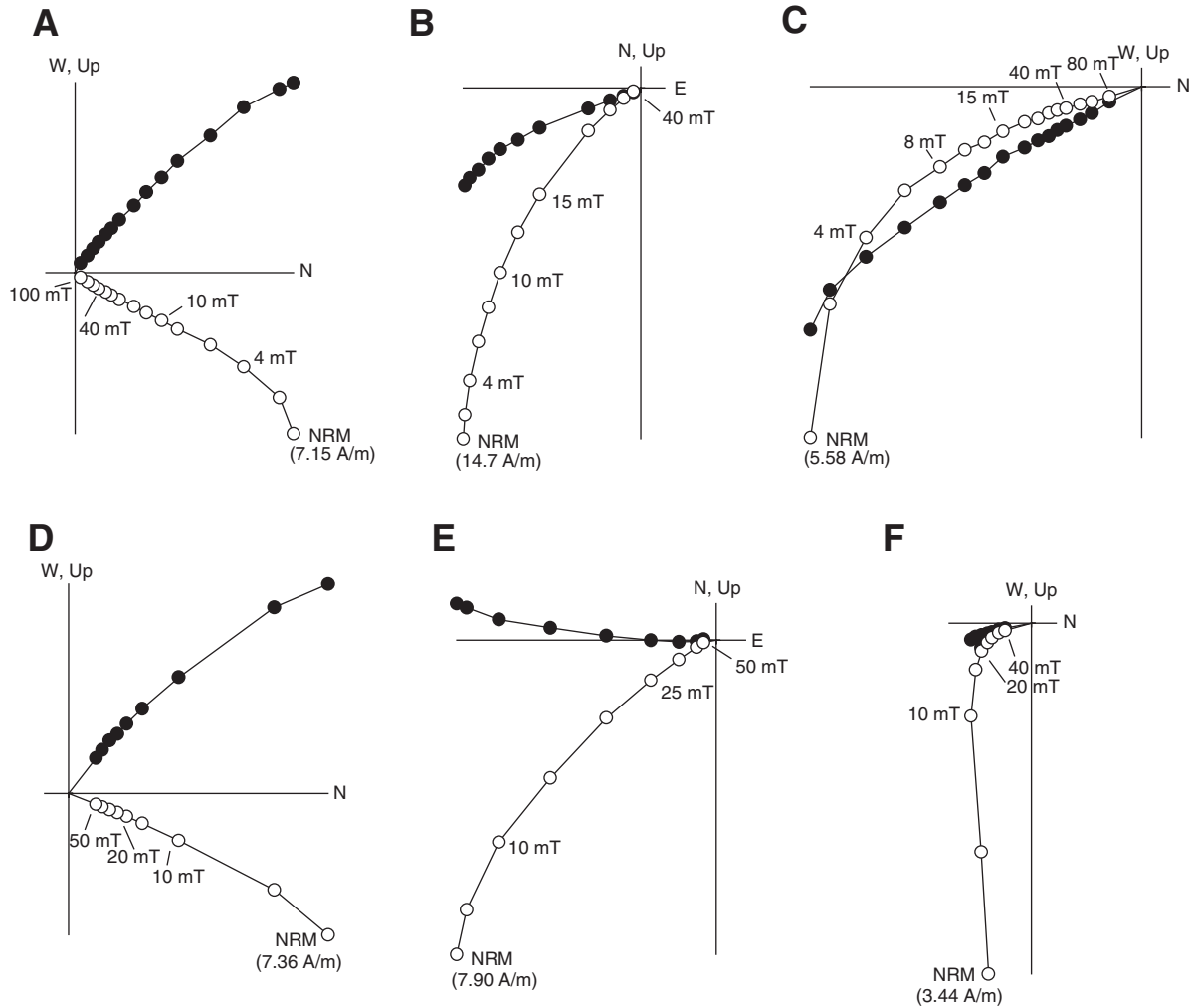
Figure F71. Normalized magnetization decay curves of discrete samples from Site 1271. Decay is plotted as a function of the vector difference sum. Serpentinized samples with no relict igneous structure are shown in blue. Altered dunite, harzburgite, and troctolite are indicated by red dashed curves. Low median destructive fields (3–12 mT) reflect a variable intensity drilling overprint presumably carried by coarse-grained magnetite. B = peak induction.
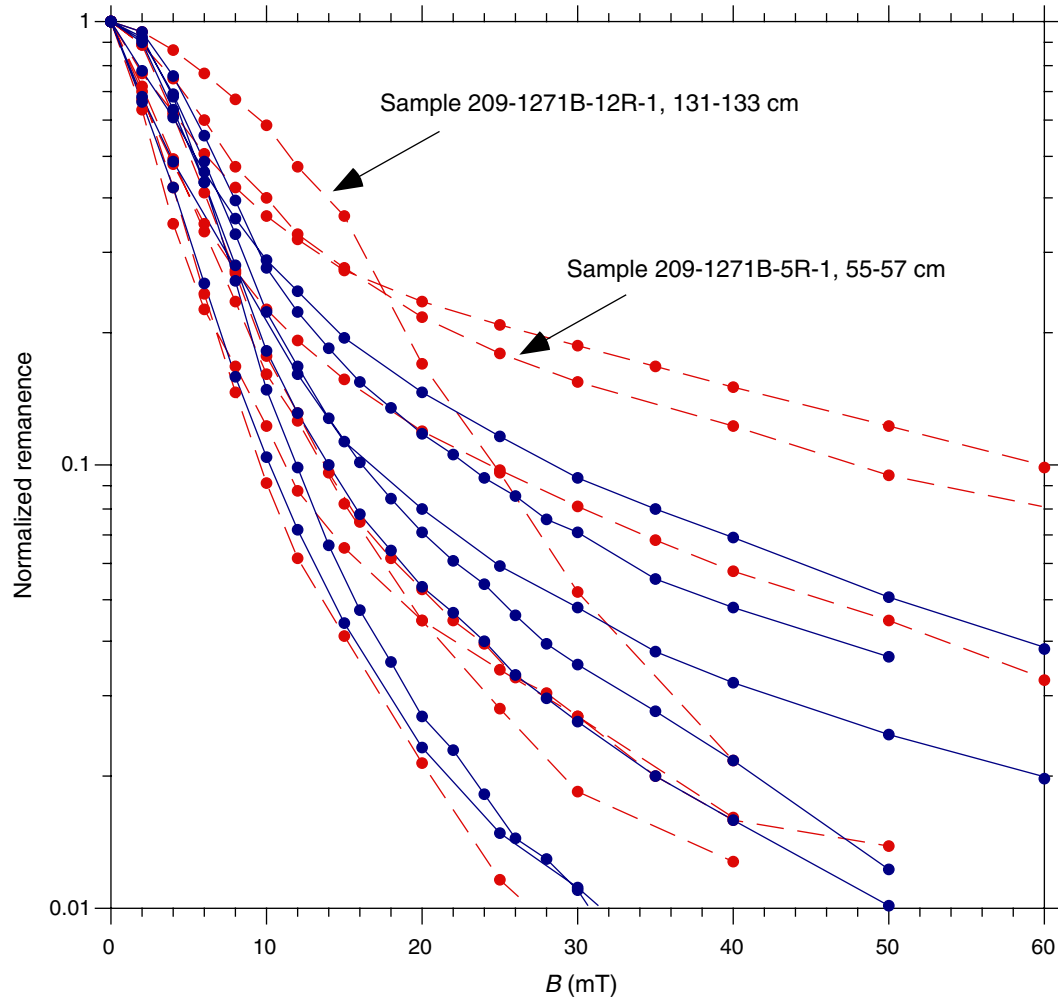
Figure F72. Histograms of paleomagnetic (**A**) inclinations and (**B**) declinations from Site 1271. Discrete (black) and archive-half continuous (gray) measurements show positive inclinations that average 25° and 29°, respectively. Rose diagram shows declinations for the combined data set. A weak bimodal distribution of declinations (northeast and southwest) can be explained by the predominance of near-vertical veining or foliation planes.
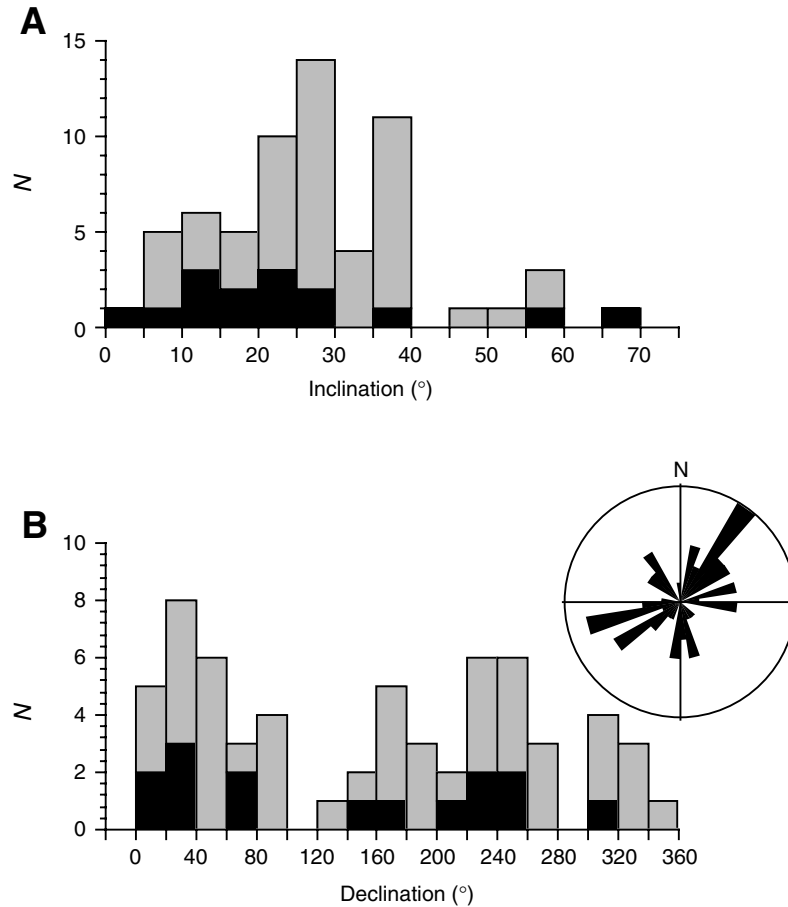
Figure F73. Lower hemisphere equal-area projections of (**A**) minimum and (**B**) maximum eigenvectors of the susceptibility tensors for Site 1271. More foliated samples (foliation > lineation; black circles) may indicate a preferred subvertical foliation oriented northwest–southeast. Samples with lineation > foliation are indicated by gray circles.
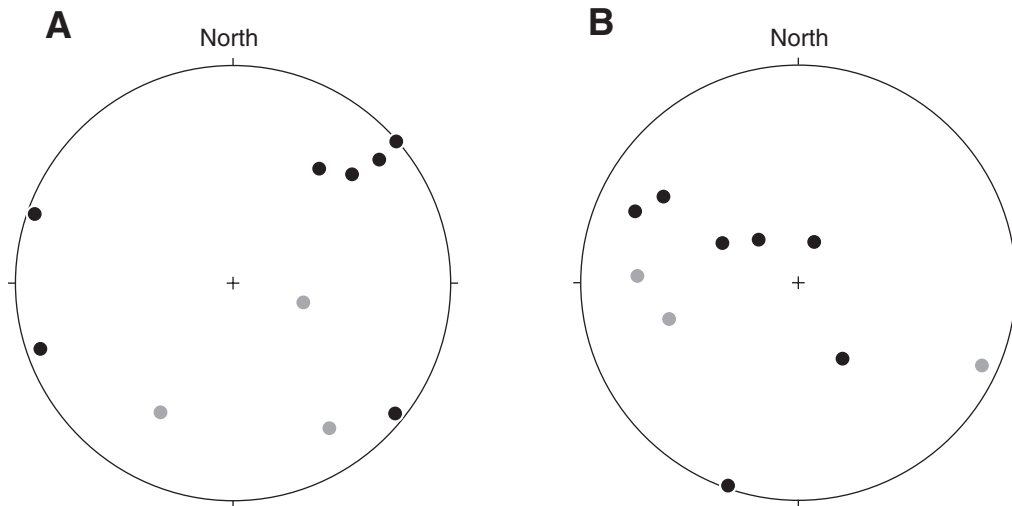
Figure F74. Graph of the gas chromatograph area counts vs. concentration of the perfluorcarbon tracer in standards and sample pieces.
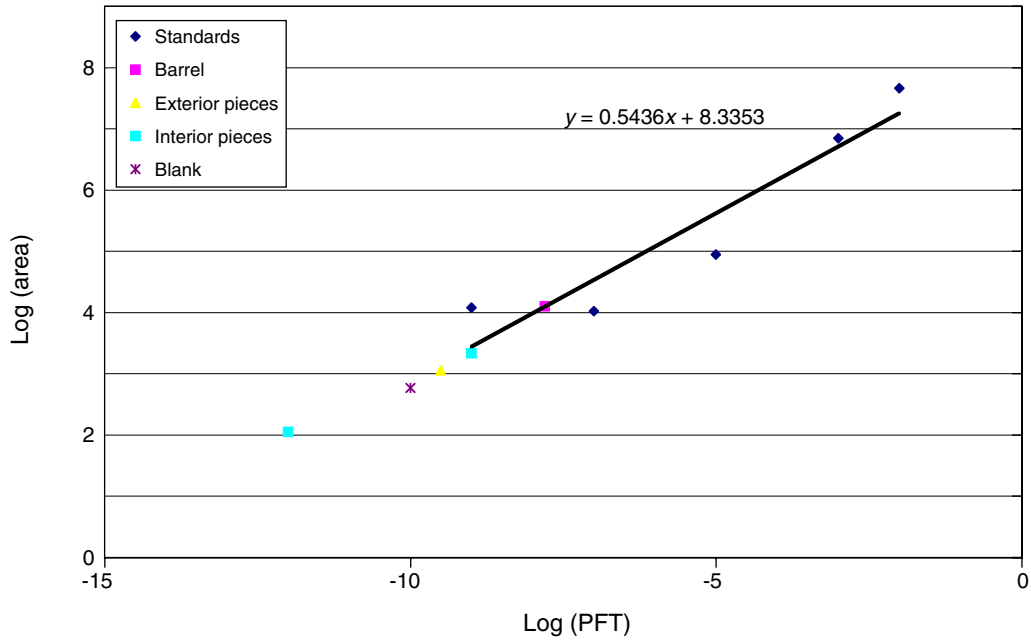
Table T1. Coring summary, Site 1271.

Hole 1271A
  Latitude:15°2.2224′N
  Longitude: 44°56.8865′W
  Time on site: 111.00 (1645 hr, 2 June–0745 hr, 7 June 2003)
  Time on hole: 34.00 (1645 hr, 2 June–0245 hr, 4 June 2003)
  Seafloor (drill pipe measurement from rig floor, mbrf): 3623.0
  Distance between rig floor and sea level (m): 11.1
  Water depth (drill pipe measurement from sea level, m): 3611.9
  Total depth (drill pipe measurement from rig floor, mbrf): 3667.8
  Total penetration (meters below seafloor, mbsf): 44.8
  Total length of cored section (m): 44.8
  Total core recovered (m): 5.76
  Core recovery (%): 12.9
  Total number of cores: 6

Hole 1271B
  Latitude:15°2.1888′N
  Longitude: 44°56.9119′W
  Time on hole: 77.0 (0245 hr, 4 June–0745 hr, 7 June 2003)
  Seafloor (drill pipe measurement from rig floor, mbrf): 3596.0
  Distance between rig floor and sea level (m): 11.1
  Water depth (drill pipe measurement from sea level, m): 3584.9
  Total depth (drill pipe measurement from rig floor, mbrf): 3699.8
  Total penetration (meters below seafloor, mbsf): 103.8
  Total length of cored section (m): 103.8
  Total core recovered (m): 15.9
  Core recovery (%): 15.3
  Total number of cores: 20

Core	Date (Jun 2003)	Local time (hr)	Top	Bottom	Cored	Recovered	Recovery (%)	Remarks
			Depth (mbsf)		Length (m)			
209-1271A-								
1R	3	1015	0.0	13.9	13.9	2.32	16.7	
2R	3	1245	13.9	18.9	5.0	0.12	2.4	
3R	3	1435	18.9	28.5	9.6	0.54	5.6	
4R	3	1725	28.5	38.1	9.6	2.32	24.2	
5R	3	2100	38.1	42.8	4.7	0.23	4.9	AHC
6R	4	0210	42.8	44.8	2.0	0.23	11.5	Core catcher jam
			Cored totals:		44.8	5.76	12.9	
209-1271B-								
1R	4	0925	0.0	12.0	12.0	0.47	3.9	AHC
2R	4	1100	12.0	17.0	5.0	0.14	2.8	AHC; PFT
3R	4	1330	17.0	26.6	9.6	0.93	9.7	AHC; PFT, Whirl-Pak
4R	4	1620	26.6	27.7	1.1	0.48	43.6	AHC; PFT, Whirl-Pak
5R	4	2100	27.7	32.2	4.5	0.57	12.7	PFT, Whirl-Pak
6R	4	2310	32.2	36.2	4.0	0.50	12.5	PFT, Whirl-Pak
7R	5	0230	36.2	40.7	4.5	0.83	18.4	PFT, Whirl-Pak
8R	5	0500	40.7	45.7	5.0	0.66	13.2	PFT, Whirl-Pak
9R	5	0635	45.7	50.5	4.8	0.16	3.3	
10R	5	0845	50.5	55.5	5.0	1.30	26.0	
11R	5	1045	55.5	60.1	4.6	1.05	22.8	
12R	5	1315	60.1	65.1	5.0	1.64	32.8	
13R	5	1515	65.1	69.8	4.7	0.82	17.5	
14R	5	1715	69.8	74.8	5.0	0.62	12.4	
15R	5	2000	74.8	79.5	4.7	0.62	13.2	
16R	5	2225	79.5	84.5	5.0	0.27	5.4	
17R	6	0250	84.5	89.1	4.6	1.18	25.7	
18R	6	0530	89.1	94.1	5.0	1.08	21.6	
19R	6	0905	94.1	98.8	4.7	1.34	28.5	
20R	6	1340	98.8	103.8	5.0	1.24	24.8	
			Cored totals:		103.8	15.90	15.3	

Notes: AHC = active heave compensation. PFT = perfluorocarbon tracer.

Table T2. XRD results, Holes 1271A and 1271B.

Core, section, interval (cm)	Depth (mbsf)	Piece	Rock type	Mineralogy			ICP-AES analyses	Thin section
				Major	Minor	Trace		
209-1271A-								
1R-1, 73–77	0.7	11	Dunite	Lizardite	Magnetite		Yes	Yes
4R-2, 32–37	30.1	1	Dunite	Lizardite, brucite	Magnetite		Yes	Yes
4R-2, 106–111	30.8	7B	Dunite	Lizardite, brucite	Magnetite		Yes	Yes
209-1271B-								
5R-1, 19–23	27.9	4	Gabbro?	Amphibole	Plagioclase	Quartz?	Yes	Yes
8R-1, 39–43	41.1	9	Gabbro?	Plagioclase	Amphibole, lizardite	Cpx	Yes	Yes
8R-1, 65–68	41.4	14	Dunite	Lizardite	Magnetite		Yes	Yes
10R-1, 109–112	51.6	19	Harzburgite	Lizardite	Magnetite		Yes	Yes
12R-1, 134–139	61.4	21	Dunite	Hornblende	Lizardite	Magnetite	Yes	Yes
17R-1, 105–110	85.6	16	Harzburgite	Lizardite	Magnetite	Brucite	Yes	Yes
17R-1, 107–109	85.6	16	Harzburgite*	Lizardite	Magnetite, brucite		Yes	Yes

Notes: Cpx = clinopyroxene. * = light gray material on the margin of dark gray serpentinized harzburgite. Due to peak overlap, samples with identified lizardite may also contain chrysotile. Qualifiers "major, minor, and trace" indicate relative abundances based on peak heights and do not necessarily reflect true relative proportions. ICP-AES = inductively coupled plasma–atomic emission spectrometry. ICP-AES data are available in Table T4, p. 122. This table is also available in ASCII.

Table T3. Vein mineralogy, Holes 1271A and 1271B.

Hole	1271A	1271B
Penetration depth (mbsf)	44.8	103.8
Recovery (%)	12.9	15.3
Length recovered (m)	5.8	15.9
Volume recovered (cm^3)	14,445	39,818
Veins in hole (cm^3/m)	169.9	78.8
Veins in hole (%)	6.8	3.1
Vein minerals in hole (cm^3/m):		
Serpentine	134.5	48.9
Magnetite	4.3	11.8
Amphibole	9.0	3.0
Talc	14.6	7.6
Carbonate	3.6	4.7
Quartz	—	1.3
Others	3.9	1.5
Vein minerals in hole (%):		
Serpentine	5.4	1.9
Magnetite	0.2	0.5
Amphibole	0.4	0.1
Talc	0.6	0.3
Carbonate	0.1	0.2
Quartz	—	0.1
Others	0.2	0.1
Vein minerals in veins (%):		
Serpentine	79.2	62.0
Magnetite	2.5	15.0
Amphibole	5.3	3.8
Talc	8.6	9.6
Carbonate	2.1	6.0
Quartz	—	1.7
Others	2.3	1.9

Notes: The volume of veins is based on macroscopic observations of vein mineralogy and estimates of vein percentages by pieces. We computed volume percentage of veins by using the volume weighted average of the macroscopic estimates using the relative curated length and assuming a constant core radius throughout the site. This table is also available in **ASCII.**

Table T4. Major and trace element compositions of rocks, Holes 1271A and 1271B.

Core, section, interval (cm)	Depth (mbsf)	Piece	Unit	Lithology	Major element oxides (wt%)											Volatiles (wt%)		
					SiO_2	TiO_2	Al_2O_3	Fe_2O_3	MgO	MnO	CaO	Na_2O	K_2O	Total	LOI	CO_2	H_2O
209-1271A-																	
1R-1, 73–77	0.73	11		Dunite	44.00	<0.01	0.05	14.15	41.20	0.08	<0.06	0.13	0.02	99.67	11.86	0.11	14.43
4R-2, 32–37	30.09	1		Dunite	38.34	0.02	0.75	11.73	45.77	0.13	<0.06	0.03	0.02	96.80	14.33	0.24	17.57
4R-2, 106–111	30.83	7B		Dunite	38.91	0.02	0.99	11.06	46.16	0.16	<0.06	0.06	0.03	97.40	14.90	0.27*	14.94*
209-1271B-																	
5R-1, 19–23	27.89	4	I	Brown amphibole gabbro	48.26	3.33	16.15	4.66	12.58	0.22	11.68	2.34	0.87	100.09	1.74	0.13	2.30
8R-1, 39–43	41.09	9	I	Gabbro	47.19	0.77	15.70	10.06	10.16	0.30	12.43	1.85	0.09	98.54	2.59	0.13	3.45
8R-1, 65–68	41.35	14	I	Dunite	41.33	0.01	0.73	11.16	43.41	0.14	<0.06	0.04	0.01	96.83	13.96	0.25	15.92
10R-1, 109–112	51.59	19	II	Harzburgite	43.25	<0.01	0.46	9.77	42.52	0.07	2.11	0.06	<0.01	98.24	13.87	1.54	14.69
12R-1, 134–139	61.44	21	III	Impregnated dunite	45.92	0.09	3.35	9.23	35.63	0.14	3.51	0.53	0.02	98.42	8.64	0.21	10.47
17R-1, 105–110	85.55	16	III	Harzburgite	42.48	0.02	0.39	9.19	45.78	0.08	0.15	0.03	<0.01	98.13	13.74	0.30	16.26
17R-1, 107–109	85.57	16	III	Harzburgite	42.71	0.02	0.43	7.71	46.50	0.10	0.07	0.05	<0.01	97.60	14.16	0.27	17.49

Notes: * = analyzed using smaller sample sizes for improved H_2O calibration. NA = not analyzed. This table is also available in **ASCII.**

Table T4 (continued).

Core, section, interval (cm)	Depth (mbsf)	Piece	Unit	Lithology	Trace elements (ppm)									
					S	Cr	Ni	Ba	Sr	V	Y	Zr	Sc	Co
209-1271A-														
1R-1, 73–77	0.73	11		Dunite	762	50	2849	<39	5	6.3	<2	3	3.2	191
4R-2, 32–37	30.09	1		Dunite	NA	9123	2245	<39	<5	36.3	<2	5	4.8	160
4R-2, 106–111	30.83	7B		Dunite	NA	7037	2090	<39	<5	30.2	<2	<2	5.6	124
209-1271B-														
5R-1, 19–23	27.89	4	I	Brown amphibole gabbro	NA	69	598	498	279	390.4	48	122	60.2	115
8R-1, 39–43	41.09	9	I	Gabbro	758	640	223	65	84	238.7	19	40	37.2	48
8R-1, 65–68	41.35	14	I	Dunite	981	6075	2737	139	<5	34.7	<2	2	5.8	143
10R-1, 109–112	51.59	19	II	Harzburgite	875	2711	2952	<39	290	33.1	<2	2	8.2	126
12R-1, 134–139	61.44	21	III	Impregnated dunite	1075	3559	1792	<39	6	88.3	16	35	19.7	101
17R-1, 105–110	85.55	16	III	Harzburgite	1330	2536	2599	<39	<5	24.3	<2	<2	6.0	<32
17R-1, 107–109	85.57	16	III	Harzburgite	1269	2865	2690	<39	<5	26.2	<2	<2	5.8	<32

Table T5. Major and trace element compositions of mineral separates, Site 1271.

Core, section, interval (cm)	Depth (mbsf)	Piece	Unit	Mineral	Major element oxides (wt%)											Volatiles (wt%)		
					SiO_2	TiO_2	Al_2O3	Fe_2O_3	MgO	MnO	CaO	Na_2O	K_2O	Total	LOI	CO_2	H_2O
209-1271B-																	
11R-1, 66–67	56.16	13	III	Plagioclase	46.79	0.12	32.83	0.25	0.82	0.03	15.45	2.05	0.49	98.83	NA	0.05	0.90
11R-1, 66–67	56.16	13	III	Brown amphibole	51.47	1.61	5.45	6.17	19.91	0.20	12.56	2.25	0.09	99.72	NA		
13R-1, 32–33	65.42	6	III	Chromite	15.71	0.18	17.22	18.63	20.67	0.19	0.08	0.12	0.06	72.88	NA	0.07	6.05

Notes: Only 19 mg of the 100-mg chromitite sample was dissolved. The high SiO_2 content suggests that this sample also contained some silicate minerals in addition to chromite and other oxides. Mg# = $100 \times$ (Mg/[Mg+Fe]) with all Fe as Fe^{2+}. An = anorthite. NA = not analyzed, BDL = below detection limit. This table is also available in **ASCII.**

Table T5 (continued).

Core, section, interval (cm)	Depth (mbsf)	Piece	Unit	Mineral	Trace elements (ppm)										(%)
					S	Cr	Ni	Ba	Sr	V	Y	Zr	Sc	Co	
209-1271B-															
11R-1, 66–67	56.16	13	III	Plagioclase	743	<41	<165	337	686.5	21.1	4	5	1	<32	An = 81
11R-1, 66–67	56.16	13	III	Brown amphibole		291	887	<39	15.3	588.4	37	39	136	57	Mg# = 86
13R-1, 32–33	65.42	6	III	Chromite	723	146,666	1,128	<39	6.3	593.3	<2	4	3	303	

Table T6. Thermal conductivity measurements, Holes 1271A and 1271B.

Core, section, interval (cm)	Depth (mbsf)	Piece	Thermal conductivity* (W/[m·K])	Standard deviation	Standard error	Needle orientation	Apparent anisotropy (%)	Primary lithology
209-1271A-								
1R-1, 52–66	0.52	10	3.05	0.042	0.021	0	4.4	Serpentinite
1R-1, 52–66	0.52	10	2.92	0.049	0.024	1		Serpentinite
1R-1, 52–66	0.52	10	2.95	0.030	0.015	2		Serpentinite
4R-2, 77–89	30.54	6	3.15	0.029	0.015	0	0.6	Serpentinite
4R-2, 77–89	30.54	6	3.17	0.027	0.013	1		Dunite/Serpentinite
4R-2, 77–89	30.54	6	3.16	0.010	0.005	2		Dunite/Serpentinite
209-1271B-								
5R-1, 49–60	28.19	10	2.69	0.015	0.008	0	5.5	Dunite
5R-1, 49–60	28.19	10	2.84	0.007	0.003	1		Dunite
5R-1, 49–60	28.19	10	2.69	0.009	0.004	2		Dunite
10R-1, 106–118	51.56	19	3.04	0.028	0.014	0	2.0	Harzburgite
10R-1, 106–118	51.56	19	3.00	0.031	0.015	1		Harzburgite
10R-1, 106–118	51.56	19	3.07	0.030	0.015	2		Harzburgite
12R-1, 126–140	61.36	21	2.88	0.012	0.006	0	1.8	Troctolite
12R-1, 126–140	61.36	21	2.93	0.025	0.013	1		Troctolite
12R-1, 126–140	61.36	21	2.88	0.017	0.008	2		Troctolite
18R-1, 49–59	89.59	10	2.54	0.015	0.007	0	3.1	Dunite
18R-1, 49–59	89.59	10	2.56	0.021	0.010	1		Dunite
18R-1, 49–59	89.59	10	2.48	0.018	0.009	2		Dunite
19R-2, 1–12	95.61	1	2.80	0.004	0.002	0	3.1	Dunite
19R-2, 1–12	95.61	1	2.73	0.002	0.001	1		Dunite
19R-2, 1–12	95.61	1	2.82	0.015	0.007	2		Dunite

Notes: * = average of four measurements. 0 = parallel to core axis, 1 = oblique to core axis (~35°), 2 = oblique to core axis (~35°) in opposite direction. This table is also available in **ASCII.**

Table T7. Porosity, density, and velocity on discrete samples, Holes 1271A and 1271B.

Core, section, interval (cm)	Depth (mbsf)	Volume measured in pycnometer			Volume measured with caliper			V_P (km/s)				V_P apparent anisotropy (%)	Primary lithology
		Density (Mg/m³)		Porosity (%)	Density (Mg/m³)		Porosity (%)						
		Bulk	Grain		Bulk	Grain		x	y	z	Mean		
209-1271A-													
1R-1, 70–72	0.70	—	—	—	2.43	2.48	6.7	3.00	3.25	3.02	3.09	8.13	Serpentinite
4R-1, 92–94	29.42	2.54	2.65	6.6	2.55	—	—	4.00	3.72	3.74	3.82	7.49	Dunite/Serpentinite
4R-2, 26–29	30.03	—	—	—	2.54	2.55	3.1	3.49	3.58	3.51	3.53	2.41	Dunite/Serpentinite
4R-2, 103–105	30.80	—	—	—	2.53	2.54	3.6	3.52	3.41	3.49	3.48	3.19	Dunite/Serpentinite
209-1271B-													
5R-1, 55–57	28.25	2.47	2.61	9.1	2.53	—	—	3.57	3.45	3.51	3.51	3.42	Dunite
8R-1, 69–71	41.39	2.42	2.59	10.9	2.46	—	—	2.99	3.00	3.11	3.03	3.92	Dunite
10R-1, 112–114	51.62	2.48	2.66	10.8	2.52	—	—	3.36	3.63	3.45	3.48	7.93	Harzburgite
12R-1, 131–134	61.41	2.66	2.69	1.9	2.71	—	—	4.89	4.94	4.90	4.91	0.92	Troctolite
17R-1, 58–60	85.08	2.53	2.64	6.5	2.53	—	—	3.94	3.98	3.73	3.88	6.59	Dunite
19R-1, 20–22	94.30	2.48	2.65	10.5	2.48	—	—	3.35	3.24	3.32	3.30	3.39	Dunite

Note: This table is also available in **ASCII.**

Table T8. Summary of discrete sample data, Holes 1271A and 1271B.

Core, section, interval (cm)	Depth (mbsf)	Piece	Lithology	N	Decay type	MAD (°)	Remanence direction (°)		Demagnetization (mT)		J (A/m)	PCA (%)
							Declination	Inclination	Low	High		
209-1271A-												
1R-1, 70	0.70	11	1	8	F	1.6	38.7	23.3	20	80	1.2028	11.26
3R-1, 60	19.50	11	1	7	F	3.2	12.1	69.6	24	50	0.3268	2.52*
4R-1, 17	28.67	5	17	7	F	11.8	77.5	20.1	24	50	0.3468	2.57*
4R-1, 88	29.38	14	17	7	F	8.5	211.9	14.8	24	50	0.3305	3.97*
4R-1, 92	29.42	14	17	7	F	2.3	221.4	5.0	20	60	0.3882	6.41
4R-2, 22	29.99	1	17	9	F	3.8	31.5	55.9	20	50	0.4287	2.20*
4R-2, 26	30.03	1	17	6	F	6.3	20.0	17.7	20	50	0.2464	1.81
4R-2, 103	30.80	7B	17	8	F	1.9	234.4	3.6	20	80	0.7689	12.98
4R-2, 121	30.98	7C	17	9	F	4.5	245.5	15.4	20	50	0.4102	8.27*
209-1271B-												
5R-1, 55	28.25	10	1	8	F	2.1	152.0	14.8	20	80	1.0283	18.44
8R-1, 69	41.39	14	1	5	F	3.1	73.4	12.6	15	40	0.4784	4.94
10R-1, 112	51.62	19	2	8	F	1.3	312.6	20.3	15	100	1.8066	25.35
12R-1, 131	61.41	21	14	4	F	1.6	250.2	39.8	20	40	2.2491	15.03
17R-1, 58	85.08	10	1	5	F	3.3	177.7	26.0	15	40	0.2436	7.11
19R-1, 20	94.30	3	1	5	F	1.5	4.4	27.0	15	40	0.5976	3.70

Notes: Lithology: 1 = dunite, 2 = harzburgite, 14 = troctolite, 17 = serpentinite. N = number of points. Decay type: F = free of origin. MAD = maximum angular deviation. Principal component analysis (PCA) (%) = percentage of natural remanent magnetization intensity. * = quarter-round samples. This table is also available in **ASCII.**

Table T9. Piece orientations from archive-half data, Holes 1271A and 1271B.

Core, section, interval (cm)	Depth (mbsf)	Piece	Lithology	N	Decay type	MAD (°)	Remanence direction (°)		Demagnetization (mT)		J (A/m)	PCA (%)
							Declination	Inclination	Low	High		
209-1271A-												
1R-1, 44	0.44	9	1	5	F	2.8	252.5	14.6	15	40	0.2107	7.8
1R-1, 60	0.60	10	1	4	F	2.7	91.2	34.0	20	40	0.8205	6.4
1R-1, 78	0.78	11	1	3	A	2.2	51.6	35.9	25	40	1.0494	6.2
1R-1, 98	0.98	12	1	3	A	2.3	37.0	34.6	25	40	0.9933	6.7
1R-1, 114	1.14	14	1	3	A	1.0	41.3	24.5	25	40	0.7309	14.2
1R-2, 32	1.74	7	1	3	A	2.0	79.5	23.6	25	40	0.2849	60.1*
1R-2, 70	2.12	14	1	3	A	0.8	179.3	29.6	25	40	0.133	60.1*
1R-2, 90	2.32	18	1	3	A	1.3	267.5	24.1	25	40	0.149	57.8*
1R-2, 106	2.48	19	1	2	A	2.2	252.6	31.5	30	40	0.2649	41.4*
3R-1, 64	19.54	11	1	2	A	2.9	33.0	56.8	30	40	0.0905	2.4
4R-1, 22	28.72	5	17	5	F	1.7	78.6	8.4	15	40	0.4551	9.2
4R-1, 82	29.32	13	17	4	F	2.8	34.7	27.2	20	40	0.2888	3.3
4R-1, 94	29.44	14	17	3	F	3.9	222.0	29.0	25	40	0.1687	2.0
4R-1, 110	29.60	17	17	2	A	3.1	91.3	24.8	30	40	0.1329	1.9
4R-2, 6	29.83	1	17	4	F	1.2	32.4	36.7	20	40	0.1932	2.2
4R-2, 42	30.19	2	17	4	F	1.8	12.2	7.3	20	40	0.4682	6.4
4R-2, 52	30.29	3	17	4	F	2.3	165.9	39.0	20	40	0.2213	3.1
4R-2, 56	30.33	3	17	4	F	2.4	183.9	22.5	20	40	0.3374	3.9
4R-2, 68	30.45	4	17	4	F	0.8	206.7	13.7	20	40	0.2786	4.7
4R-2, 84	30.61	6	17	4	F	1.7	301.4	22.1	20	40	0.4467	6.4
4R-2, 110	30.87	7	17	3	A	3.1	237.5	9.5	25	40	0.3796	5.2
209-1271B-												
5R-1, 52	28.22	10	1	2	A	0.4	169.0	16.0	40	50	0.335	9.7
7R-1, 20	36.40	4	1	5	A	2.0	130.4	36.8	20	50	0.1589	3.6
7R-1, 28	36.48	5	1	4	F	3.1	45.3	33.1	25	50	0.1273	2.6
7R-1, 54	36.74	7	1	4	F	1.0	41.4	22.9	25	50	0.257	11.5
8R-1, 74	41.44	14	1	4	F	4.3	53.3	34.8	25	50	0.2861	2.5
10R-1, 110	51.60	19	2	4	F	3.2	311.2	14.3	25	50	0.6778	9.2
10R-1, 124	51.74	20	2	4	F	3.6	50.3	27.7	25	50	0.192	8.2
11R-1, 104	56.54	19	1	4	F	2.8	268.6	28.8	25	50	0.7036	15.9
11R-1, 114	56.64	20	1	4	F	2.6	239.2	24.9	25	50	1.4958	25.3
12R-1, 38	60.48	7	14	4	F	2.2	23.8	24.7	25	50	0.666	18.0
12R-1, 52	60.62	8	14	4	F	2.4	128.9	–28.7	25	50	1.0623	22.4†
12R-1, 74	60.84	12	14	4	F	3.4	252.0	45.9	25	50	0.6995	15.0
12R-1, 98	61.08	16	14	4	F	0.9	322.5	18.5	25	50	0.4563	17.4
12R-1, 134	61.44	21	14	4	F	2.3	269.7	35.7	25	50	1.252	15.9
13R-1, 56	65.66	10	1	4	F	2.3	185.1	36.8	25	50	0.0705	5.2
14R-1, 18	69.98	4	10	3	A	2.4	254.5	21.7	25	40	0.0001	31.1
15R-1, 26	75.06	5	1	4	A	1.2	146.9	28.4	25	50	0.4069	15.6
17R-1, 12	84.62	2	10	4	F	6.4	98.4	23.5	25	50	0.0002	37.1
17R-1, 62	85.12	10	1	3	F	2.4	182.6	57.2	30	50	0.0727	1.6
17R-1, 104	85.54	16	2	5	F	1.5	356.8	27.5	20	50	0.8441	9.4
18R-1, 54	89.64	10	1	5	F	1.8	161.3	8.5	20	50	0.5953	17.1
18R-1, 112	90.22	20	1	5	F	0.9	325.5	25.7	20	50	0.5114	29.2
19R-1, 16	94.26	3	1	5	F	1.3	10.8	37.2	20	50	0.3452	3.7
19R-2, 8	95.68	1	1	5	F	2.3	324.6	52.2	20	50	0.4363	3.9
20R-1, 84	99.64	16	1	4	F	2.5	359.7	37.6	20	40	0.13	3.7

Notes: Lithology: 1 = dunite, 2 = harzburgite, 10 = gabbro, 14 = troctolite, 17 = serpentinite. *N* = number of samples. Decay type: A = anchored to origin, F = free of origin. MAD = maximum angular deviation. PCA (%) = percentage of natural remanent magnetization intensity. * = PCA (%) normalized to 15-mT demagnetization step. † = sample marked upside down. Corrected direction = 231/28.7. This table is also available in **ASCII.**

Table T10. Anisotropy of magnetic susceptibility, Holes 1271A and 1271B.

Core, section, interval (cm)	Depth (mbsf)	Piece	Susceptibility (SI)	1 σ	Maximum*			Intermediate*			Minimum*		
					Value	Dec (°)	Inc (°)	Value	Dec (°)	Inc (°)	Value	Dec (°)	Inc (°)
209-1271A-													
1R-1, 70	0.70	11	1.456E–01	0.00029	0.3514	293.0	38.2	0.3275	72.8	44.1	0.3210	185.1	21.3
4R-1, 92	29.42	14	1.120E–01	0.00036	0.3565	154.9	19.1	0.3391	41.2	49.2	0.3045	258.6	34.5
4R-2, 26	30.03	1	1.163E–01	0.00047	0.3586	169.8	56.7	0.3429	5.9	32.3	0.2985	271.2	7.4
4R-2, 103	30.80	7B	9.984E–02	0.00022	0.3487	172.2	57.7	0.3354	21.7	28.8	0.3159	284.2	13.3
209-1271B-													
5R-1, 55	28.25	10	1.060E–01	0.00088	0.3723	109.4	67.8	0.3391	291.5	22.2	0.2886	201.2	0.8
8R-1, 69	41.39	14	1.290E–01	0.00037	0.3804	95.1	73.4	0.3326	293.6	15.8	0.2870	202.2	5.0
10R-1, 112	51.62	19	8.649E–02	0.00014	0.3437	66.7	8.1	0.3315	324.3	56.2	0.3248	161.9	32.5
12R-1, 131	61.41	21	7.917E–02	0.00013	0.3447	89.4	1.6	0.3343	337.1	85.7	0.3211	179.5	4.0
17R-1, 58	85.08	10	1.181E–01	0.00021	0.3493	90.1	27.0	0.3290	182.8	5.3	0.3217	283.0	62.4
19R-1, 20	94.30	3	1.150E–01	0.00028	0.3545	306.9	27.6	0.3467	178.7	49.8	0.2987	52.1	26.7

Notes: σ = 1 standard deviation for normalized eigenvalues. Total anisotropy critical value = 3.4817. * = unrotated core coordinates (double line on working half = 360°, inclination positive down). Dec = declination, inc = inclination. F12 = max, min eigenvalues, F23 = int, min eigenvalues (critical value = 4.2565 for F12 and F23). P (degree of anisotropy) = max/min eigenvalues, F (magnetic foliation) = int/min eigenvalues, L (magnetic lineation) = max/int eigenvalues. AMS = anisotropy of magnetic susceptibility. † = anisotropy of magnetic susceptibility core coordinates rotated to 360°. This table is also available in **ASCII**.

Table T10 (continued).

Core, section, interval (cm)	Depth (mbsf)	Piece	Total anisotropy	F12	F23	P	F	L	Minimum†		Maximum†	
									Dec (°)	Inc (°)	Dec (°)	Inc (°)
209-1271A-												
1R-1, 70	0.70	11	2434.8	3397.4	248.7	1.095	1.020	1.073	146.4	21.3	254.3	38.2
4R-1, 92	29.42	14	4382.4	1183.5	4679.9	1.171	1.114	1.051	37.2	34.5	293.5	19.1
4R-2, 26	30.03	1	3500.4	553.5	4441.9	1.201	1.149	1.046	251.2	7.4	149.8	56.7
4R-2, 103	30.80	7B	4417.6	1804.2	3844.9	1.104	1.062	1.040	49.8	13.3	297.8	57.7
209-1271B-												
5R-1, 55	28.25	10	1830.3	711.9	1639.6	1.290	1.175	1.098	49.2	0.8	317.4	67.8
8R-1, 69	41.39	14	9999.9	8336.1	7589.7	1.325	1.159	1.144	128.8	5.0	21.7	73.4
10R-1, 112	51.62	19	3768.0	3821.6	1148.4	1.058	1.021	1.037	209.3	32.5	114.1	8.1
12R-1, 131	61.41	21	6200.0	2979.7	4845.6	1.073	1.041	1.031	289.3	4.0	199.2	1.6
17R-1, 58	85.08	10	3594.5	4533.2	582.0	1.086	1.023	1.062	105.3	62.4	272.4	27.0
19R-1, 20	94.30	3	9609.8	400.5	9999.9	1.187	1.161	1.023	47.7	26.7	302.5	27.6

Table T11. GC analysis of PFT contamination, Hole 1271B.

Standard PFT curve					Samples			
Concentration (µg/mL)	PFT (g)	Peak area (counts)	Log (PFT)	Log (area counts)	Location	Peak area (counts)	Log (PFT)	Log (area counts)
1.00E–02	8.80E–07	4.59E+07	–2	7.66	Core 1	12,500	–7.8	4.10
1.00E–03	8.80E–08	6.92E+06	–3	6.84	Exterior	1,130	–9.5	3.05
1.00E–05	8.80E–10	8.80E+04	–5	4.94	Interior 1	112	–12	2.05
1.00E–07	8.80E–12	1.05E+04	–7	4.02	Interior 2	2,142	–9	3.33
1.00E–09	8.80E–14	1.19E+04	–9	4.08	Blank	584	–10	2.77

Notes: GC = gas chromatography. PFT = perfluorocarbon tracer. Sample from Section 209-1271B-7R-1 (Piece 6) run on 6 June 2003.